UNIVERSITÉ DE STRASBOURG

N° ordre UDS 687

N° ordre IPHC 2010-018

Thèse

Thèse .

Présentée par

Christophe RAPPOLD

Pour obtenir le grade de

Docteur de l'Université de Strasbourg

Spécialité

Physique Nucléaire

Study of hypernuclei in the reaction ^{6}Li+^{12}C at 2 *A* GeV

Institut Pluridisciplinaire
Hubert Curien
Département de Recherches Subatomiques

UMR 7178

IPHC
Institut Pluridisciplinaire Hubert CURIEN
STRASBOURG

UNIVERSITÉ DE STRASBOURG

Thèse présentée pour l'obtention du grade de
Docteur de l'Université de Strasbourg

Discipline : Physique Nucléaire

par : Christophe Rappold

Study of hypernuclei in the reaction ^{6}Li+^{12}C at 2 A GeV

Soutenue publiquement le 24 Septembre 2010

Membres du jury

Président du jury :	**Ulrich Goerlach (IPHC, Strasbourg)**
Rapporteurs :	**Ian Bearden (Niels Bohr Institute, Copenhagen)**
	Horst Lenske (Justus-Liebig-Universität, Giessen)
Examinateurs :	**Christelle Roy (IPHC, Strasbourg)**
	Hirokazu Tamura (Tohoku University, Sendai)
Co-directeurs :	**Take R. Saito (GSI, Darmstadt)**
	Fouad Rami (IPHC, Strasbourg)

Acknowledgements

I would like to express my gratitude to all those, who supported me and made this thesis possible, in particular my deepest gratitude to my Ph.D. advisors, Takehiko Saito and Fouad Rami for giving me the opportunity to work on this fascinating research domain and for their continuous personal and scientific support.

My gratitude also goes to my colleagues and friends from the HypHI group, with whom it was a pleasure to work with. A special thought for Shizu Minami and Myroslav Kavatsyuk who have been there since the beginning to help and guide me during this work. I would like also to address my gratitude to Sebastien Bianchin, Olga Borodina, Daisuke Nakajima and Banu Özel-Tashnov for their support, help and friendly discussions. As well to Vakkas Bozkurt, Eunhee Kim and Yue Ma who have joined the group and have helped a lot for the experiments.

I would like also to thank personally all the members of the jury. To Horst Lenske and Ian Bearden who have accepted to be my external referees, for the time that they have dedicated to me, and for their great comments on the thesis. As well as Christelle Roy and Ulrich Goerlach who had considered and accepted to be part of the jury. I would like to deeply thank Hirokazu Tamura, who have accepted and traveled from Japan in order to join the jury, for introducing me to the domain of the hypernuclear physics when I was undergraduate student in his group during my stay in Japan.

Special thanks for all the friends that I have made in GSI and Germany during all this time: the French team of GSI, Sebastien Bianchin, Tudi Le Bleis, Nicolas Wickler, Antoine Baquias, Stephane Petris, Audrey Chatillon, Vincent Pangon, Helene Ricaud, for their support, hot and trollish discussions, and friendship. But also all other friends, Juan Castillo Hernandez, Diego Gonzalez Diaz, Angela Saa Hernandez, with whom I have enjoyed a lot the after-work. It also includes non spanish speakers, like Klass Brantjes, Felix Wamers, Namita Goel, and all other persons ... Thanks for all and your valuable friendship.

Je tiens à remercier également ma famille, mes parents, mes sœurs, mes grands-parents pour tout, leurs soutiens, aides et compréhension, et qui ont toujours été là pour moi. Particularly I would like to express an important thank to Carmen Serna Moreno for her love, encouragement and patience.

In short : all of you have been part of me in this achievement, thank you.

“À ma famille”

Contents

List of Figures

List of Tables

Résumé

Contexte général

La grande majorité de la matière est constituée d'un ensemble stable de trois quarks *up* et *down* qui forment les nucléons. Cependant, la chromodynamique quantique prédit l'existence d'autres triplets stables en plus des triplets du neutron et du proton. En particulier, un *hypéron*, un triplet contenant un quark étrange, pourrait être stable dans un environnement neutronique dense, telle qu'une étoile à neutrons [6]. Il en serait l'un de constituants majeurs. La compréhension de son interaction avec les autres baryons dans ce système dense est donc cruciale pour les modèles d'étoiles à neutrons [15]. Malheureusement, l'étude directe de l'interaction hypéron-nucléon (YN) et hypéron-hypéron (YY) est difficile à mettre en œuvre, car l'obtention d'un faisceau d'hypérons ne peut se faire avec précision. De plus la faible durée de vie des hypérons empêche leur utilisation en tant que cibles. Toutefois, il a été montré que par l'étude d'un noyau comportant un hypéron, appelé *hypernoyau*, l'interaction YN et YY peut en être déduite [16].

Le terme *hypernoyau* réfère à un système contenant des nucléons et des hypérons. Généralement, cet hypéron est une particule Λ mais, il peut être une autre particule plus lourde comme, Σ ou Ξ. Un hypernoyau Λ est donc constitué de trois composants: des neutrons, des protons et des particules Λ.

L'étude des hypernoyaux se veut être le micro laboratoire pour l'étude des interactions baryoniques nucléon-hypéron et hypéron-hypéron. Les hypernoyaux sont étudiés expérimentalement en utilisant des réactions induites par des faisceaux secondaires de mésons π^+

ou K^- ou des faisceaux d'électrons sur cibles fixes. Ce type de réactions permet d'accéder au processus élémentaire de production ou d'échange de l'étrangeté. Seul un nucléon de la cible est ainsi remplacé par un hypéron, pour former des hypernoyaux proches de la vallée de stabilité [17]. L'existence d'états très fortement liés de particules Λ dans un noyau a été démontré [20]. Le principe d'exclusion de Pauli n'empêche pas l'hypéron, ainsi créé, de se placer dans une couche très profonde déjà occupée par les nucléons, permettant ainsi d'utiliser le dit hypéron comme sonde [21].

La découverte des hypernoyaux a été faite par M. Danysz et J. Pniewski en 1952 en étudiant les interactions nucléon-hypéron et hypéron-hypéron des rayons cosmiques dans une chambre à émulsion [27]. Jusqu'aux années 70, les différentes expériences mises en place utilisaient encore les émulsions irradiées par un flux de K^- faiblement énergétique. Grâce à l'étude de la désintégration en π^-, les hypernoyaux ${}^{3}_{\Lambda}$H à ${}^{15}_{\Lambda}$N ont été découverts ainsi que leurs diagrammes énergétiques [30, 31]. Cependant, avec ces méthodes, seuls ces hypernoyaux ont pu être étudiés. Avec l'apparition de faisceaux de mésons plus intenses, de nouvelles expériences ont vu le jour. Parmi celles-ci, des expériences de spectroscopie au CERN à la fin des années 60, au BNL (Brookhaven National Laboratory, USA) dans les années 80 [32, 33] et dans les années 90, au KEK (High Energy Accelerator Research Organization, Japon) [34, 35, 36, 37]. Ces expériences sont essentiellement basées sur des réactions (K^-, π^-) (CERN et BNL) et (π^+, K^+) (BNL et KEK). Les noyaux légers et de masses intermédiaires ont ainsi été étudiés, mais la résolution obtenue par spectroscopie reste de l'ordre du MeV. L'une des avancées fut l'utilisation de détecteurs au germanium pour une spectroscopie par rayonnement γ. Plusieurs expériences se sont ainsi déroulées au BNL et au KEK, où a été utilisé un ensemble de ces détecteurs au germanium, *l'Hyperball*, pour obtenir la structure énergétique des éléments ${}^{7}_{\Lambda}$Li et ${}^{9}_{\Lambda}$Be avec une résolution de quelques keV [38]. L'ensemble de ces expériences a permis de montrer que l'introduction d'un hypéron Λ dans un noyau a un effet de *colle* qui rétrécit la taille du noyau en question, et peut donc modifier toute la structure du noyau classique. Les multiples hypernoyaux créés sont principalement dans, ou proche, de la vallée de stabilité β puisqu'ils ont été formés par un faisceau mésonique sur une cible stable. L'étude des hypernoyaux loin de la vallée de stabilité permettra de compléter les connaissances sur les interactions hypéron-nucléon [17]. Pour produire de tels hypernoyaux, un faisceau d'ions lourds ou d'isotopes rares est nécessaire.

Le but de la physique hypernucléaire est de comprendre comment interagit un système à N-corps d'hadrons, aussi bien au niveau des quarks qu'au niveau des hadrons. Des régions

profondes du noyau peuvent ainsi être explorées grâce aux hypérons qui sont libérés du principe de Pauli [21]. De plus, la présence d'hypérons dans le noyau induit plusieurs modifications de la structure nucléaire, permettant ainsi d'améliorer les connaissances de celle-ci [30, 31]. La structure des hypernoyaux permet aussi d'étudier les interactions nucléon-hypéron, qui permettra d'étendre la connaissance sur les forces nucléaires et d'unifier la compréhension de l'interaction baryon-baryon [42, 43]. Les connaissances sur l'interaction faible peuvent aussi être approfondies grâce à la désintégration faible des hypernoyaux [24].

Le projet HypHI

Un projet de recherche dédié à cette thématique a débuté récemment au GSI, *Helmholtz Centre for Heavy Ion Research* (Darmstadt, Allemagne). Ce projet, appelé HypHI, propose d'introduire une nouvelle approche dans l'étude des hypernoyaux [71]. Il vise à étudier la production des hypernoyaux dans les réactions induites par des faisceaux d'ions lourds stables ou radioactifs sur cibles fixes. Dans ces réactions, les hypernoyaux sont formés par coalescence entre un hypéron produit dans la région des participants et un des fragments du projectile : La collision du projectile et de la cible provoque la formation d'une zone dense et chaude. Lorsque l'énergie initiale du projectile est suffisante, des hypérons tel que Λ sont produits dans cette région dense. Si le projectile spectateur, ne participant pas à la réaction, et l'hypéron Λ se trouvent très proches dans l'espace des phases, alors un hypernoyau peut se former par coalescence.

Les premières études théoriques sur la formation d'hypernoyaux par le biais de ce mécanisme de production ont été réalisées par Kerman et Weiss en 1973 [49]. Ils ont conclu que cette méthode de production est le seul moyen pour produire des hypernoyaux avec plusieurs hypérons ou plus exotiques. Par la suite, Wakai, Bando et Sano ont, dans une série de publications, formalisé le phénomène de coalescence sur lequel est basée la formation d'hypernoyaux [50, 51, 52, 53]. Ils ont ainsi déterminé plusieurs valeurs de section efficace de production, qu'ils ont confrontées aux données venant d'une expérience réalisée à Dubna en 1988 [72, 73]. Cette expérience fut la première étude des hypernoyaux dans les réactions induites par faisceaux de ^{4}He et de ^{7}Li sur une cible de polyéthylène.

Cette nouvelle approche expérimentale a pour but de produire des hypernoyaux proches des limites de stabilité et d'étudier leurs modes de production et de désintégration. Les

hypernoyaux ainsi créés permettent l'étude de l'influence de l'isospin sur la structure de la matière baryonique, sur les interactions baryoniques nucléon-hypéron et hypéron-hypéron, mais aussi une mesure directe du moment magnétique hypernucléaire. Cela contribuera ainsi à une meilleure compréhension des interactions fondamentales.

La présente thèse s'inscrit dans le cadre de la première phase de ce projet, dont l'objectif principal est de démontrer la faisabilité de la nouvelle méthode proposée pour l'étude des hypernoyaux, en effectuant une spectroscopie précise des hypernoyaux ${}^{4}_{\Lambda}$H, ${}^{3}_{\Lambda}$H, ${}^{5}_{\Lambda}$He.

L'expérience phase 0 et son dispositif expérimental

Dans cette première expérience, qui s'est déroulé entre août et octobre 2009, un faisceau de ^{6}Li à 2 GeV par nucléon a été utilisé sur une cible de ^{12}C avec une intensité de 10^{7} particules par seconde. Le but de cette expérience a été de démontrer la faisabilité de la spectroscopie de précision des hypernoyaux ${}^{4}_{\Lambda}$H, ${}^{3}_{\Lambda}$H, ${}^{5}_{\Lambda}$He. Seule leur décroissance mésonique par interaction faible ${}^{3}_{\Lambda}\mathrm{H} \rightarrow \pi^{-} + {}^{3}\mathrm{He}$, ${}^{4}_{\Lambda}\mathrm{H} \rightarrow \pi^{-} + {}^{4}\mathrm{He}$ et ${}^{5}_{\Lambda}\mathrm{He} \rightarrow \pi^{-} + {}^{4}\mathrm{He} + p$ est considérée. Les modèles théoriques simulant la réaction d'ions lourds relativistes montrent que chaque hypernoyau, produit par coalescence entre un hypéron et un fragment spectateur, aura une vitesse proche de celle du faisceau. Le facteur de Lorentz attendu lors de la collision à 2 GeV par nucléon est proche de $\gamma = 3$, permettant ainsi un allongement d'un facteur 3 du temps de demi-vie de l'hypernoyau et de sa longueur de décroissance. Cette propriété est la clé de la nouvelle approche que veut introduire le projet HypHI. Grâce à la production d'hypernoyaux avec un facteur de Lorentz important, leur temps de vie sera suffisamment allongé pour leur permettre de sortir de la cible. Ce point est important en comparaison des précédentes études réalisées dans les quelles les hypernoyaux ont été étudiés par spectroscopie de masse manquante. Les hypernoyaux se désintègrent par interaction faible en dehors de la cible permettant une identification claire des vertex secondaires qui se distingueront très bien des vertex primaires venant de la cible.

La spectroscopie de masse invariante de ces hypernoyaux requiert de suivre l'ensemble des traces des particules venant de la cible et de la désintégration des hypernoyaux. Chaque hypernoyau est identifié très précisément en reconstruisant les possibles vertex secondaires et en calculant leur masse par la méthode de masse invariante. Le défi de cette nouvelle approche expérimentale est intrinsèquement lié à son avantage. En utilisant les collisions d'ions lourds à 2 GeV par nucléon, l'espace des phases de la réaction est large.

La différence de section efficace entre la production des hypernoyaux, approximativement, de 0,1 à 0,5 microbarns, et le reste des produits de la collision, autour de 1 barn, produit un bruit de fond qui doit être traité de façon efficace pour permettre une spectroscopie de précision. Le défi est donc d'avoir un système de déclenchement qui soit très efficace pour sélectionner au maximum les événements de type hypernoyaux.

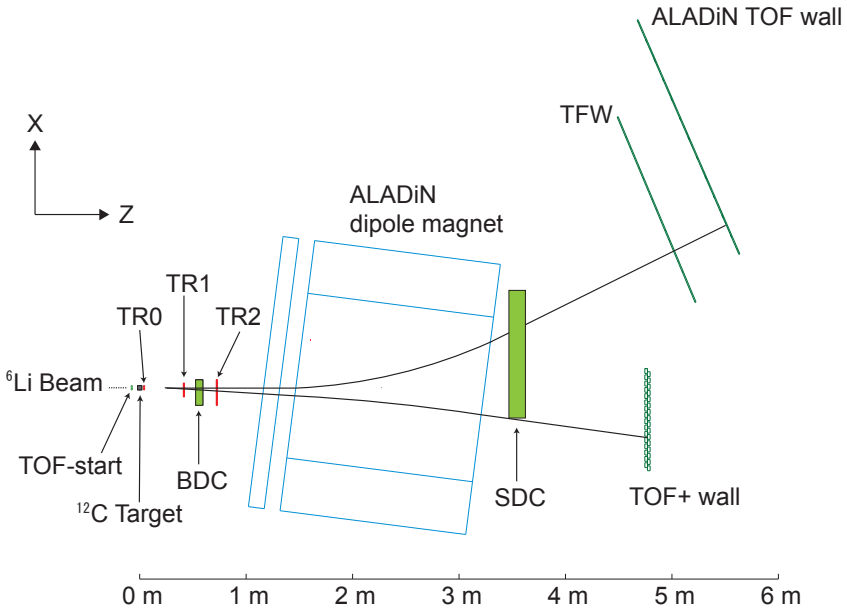

Figure 0.1.: Dispositif expérimental de la première expérience réalisée dans le cadre du projet HypHI.

La figure 0.1 présente le dispositif expérimental de l'expérience. Le faisceau venant de la gauche traverse le détecteur TOF-start placé en amont de la cible de ^{12}C. Les particules produites durant la réaction sont suivies par l'ensemble des détecteurs à fibres scintillantes TR0, TR1, TR2 et de la chambre à dérive BDC placée devant l'aimant ALADiN. Le champ magnétique crée par ce dipôle permet de défléchir les particules en fonction de leur rigidité magnétique $B\rho$, permettant ainsi le calcul de leurs impulsions respectives. L'ouverture angulaire du dipôle permet d'avoir une acceptance proche de 4π grâce au facteur de Lorentz de la réaction à 2 GeV par nucléon. Les traces de chaque particule sont suivies après leur passage à travers le champ magnétique du dipôle grâce à la seconde chambre à dérive SDC et aux différents murs de temps de vol, TOF+, TFW et ALADiN TOF. Chaque hodoscope est placé de telle façon que le mur TOF+ et les deux autres

murs soient dédiés respectivement à la détection des fragments et des π^- produit lors de la décroissance des hypernoyaux.

Conception et simulation de l'expérience

L'ensemble du dispositif expérimental a été simulé avec le logiciel GEANT4 permettant ainsi de concevoir les nouveaux détecteurs à fibres scintillantes et le nouveau mur de temps de vol TOF+. La conception complète du détecteur TOF+ fut la première partie du travail de thèse. Après avoir défini les spécifications de ce nouveau mur de temps de vol, chaque point de sa conception fut détaillé par les simulations Monte Carlo. Les caractéristiques intrinsèques des prototypes ont pu être déterminées après plusieurs expériences test avec faisceaux entérinant ainsi le cahier des charges proposé. La construction finale du détecteur fut validée lors d'une expérience de commissionnement.

Par la suite, la phase d'optimisation du dispositif expérimental fut achevée par une série de simulations Monte Carlo. Après avoir inclus la carte du champ magnétique dans la simulation GEANT4 de l'expérience, la taille des détecteurs a été optimisée pour la détection des produits de désintégration des hypernoyaux. Plus spécifiquement, l'ensemble des caractéristiques géométriques des trois stations de détection de fibres scintillantes fut adapté pour détecter les particules π^- venant spécifiquement de la décroissance des hypernoyaux. L'ensemble des fragments est concentré à proximité de l'axe du faisceau, tandis que ces π^- se trouvent très décalés de cet axe dû à l'importante impulsion transverse qui leur est transmise lors de la désintégration des hypernoyaux. Le positionnement final des détecteurs a dû aussi être revu pour permettre l'agencement de l'ensemble. En particulier, le positionnement des murs de temps de vol ALADiN TOF et TFW a été optimisé pour limiter leur encombrement tout en conservant leurs acceptances. La figure 0.1 montre les positions finales des détecteurs ainsi choisies.

Principe et performance du système de déclenchement

L'ensemble du système d'acquisition de données mis en place pour l'expérience est présenté ainsi que les développements effectués pour concevoir un module électronique logique, appelé VUPROM2. Ce module électronique est constitué de puces FPGA et DSP qui

peuvent être programmées pour différentes utilisations. En effet, ce module sert à la fois pour la lecture des canaux des détecteurs à fibres scintillantes et des chambres à dérive mais aussi à tout le système de déclenchement de l'expérience.

Le système de déclenchement est une partie cruciale pour l'expérience. La production des hypernoyaux s'effectue avec une très faible section efficace (de 0,1 à 0,5 microbarns), comparée à la section efficace totale de réaction, évaluée à 1 barn. Lors de la prise de données, le système de déclenchement permet ainsi de sélectionner les événements se comportant comme ceux des hypernoyaux. Cela aide à réduire la proportion des événements indésirables tout en gardant une certaine efficacité à trouver les événements de type hypernoyaux.

Cette réduction du bruit de fond par rapport au signal des hypernoyaux permet à la fois de rentrer dans les limites de traitement du système d'acquisition, qui se trouvent aux alentours de 3 kHz, et de sélectionner les événements susceptibles de provenir de la désintégration des hypernoyaux recherchés. Cette réduction se fait par le biais du système de déclenchement qui, pour l'expérience, est composé de trois étapes simultanées. Une étape de traitement est dédiée à la vérification de la présence de vertex secondaires, une autre étape requiert la présence de particules de charge Z=2 dans le mur de temps de vol placé du côté correspondant aux charges positives. La dernière étape sélectionne les particules de charge Z=1 détectées par le mur de temps de vol placé du côté correspondant aux charges négatives.

Le concept du sous système déclenchant sur les possibles vertex secondaires fut étudié et simulé avec le logiciel GEANT4. Le principe de ce sous système est de repérer les traces de vertex primaires venant de la cible à partir des stations de fibres scintillantes TR0, 1, 2. Ces détecteurs ont été placés de telle façon que le volume de désintégration des hypernoyaux se trouve entre TR0 et TR1. Ainsi, en combinant les informations venant des trois stations de fibres, il est possible de distinguer les traces provenant de la cible et les traces venant de la désintégration des hypernoyaux. Ce sous système évalue donc la présence de traces venant de vertex secondaires et le signale au système maître de déclenchement. Ce sous système est intégré dans les puces FPGA des modules logiques VUPROM2.

Plusieurs expériences ont permis de tester en conditions réelles ce sous système. Les dernières améliorations ont pu être apportées au système complet de déclenchement lors du commissionnement en août 2009. Les décisions prises par ce sous système ont été

enregistrées durant l'expérience. Elles ont été comparées avec les mêmes décisions prises à posteriori lors de l'analyse des données délivrées par ce sous système. Cette analyse se base sur l'algorithme utilisé pour la conception de ce sous système permettant ainsi de simuler les possibles décisions. La consistance entre l'analyse à posteriori et les décisions prises durant l'expérience est supérieure à 93 % pour l'ensemble des stations TR{1,2}{x,y} utilisé pour sélectionner les possibles vertex secondaires. De plus la distribution de canaux qui auraient déclenchés le système d'acquisition ou qui auraient été rejetés par le système de déclenchement a été comparé avec celle obtenue par les simulations lors de la conception du sous système. Cette comparaison met en évidence un très bon accord montrant ainsi que le sous-système a correctement fonctionné durant l'expérience.

Le second sous système, ayant nécessité une phase de développement, porte sur la prise de décision de la présence ou non de particules de charge Z=2 sur le mur de temps de vol TOF+. Un discriminateur permettant la mesure de la longueur du pulse au delà du seuil de discrimination est utilisé. Il est ainsi possible de discerner la charge des particules incidentes en fonction de la largeur de leur pulse logique après discrimination. L'algorithme permettant cela fut mis en œuvre dans une puce CPLD, équivalente aux puces FPGA. Plusieurs tests de l'électronique ainsi que des expériences tests avec des faisceaux d'ions ont montré que cette sélection est possible. Il a été démontré que l'efficacité de sélection des fragments de charge Z=2 est proche de 99 % avec 0,4 % de contamination de particules de charge Z=1. L'analyse de comportement de ce sous système durant l'expérience a montré que le nombre de particules enregistrées de charge Z=1 diminue tandis que le nombre de particules de charge Z=2 augmente, quand ce sous-systeme est requis, en comparaison avec le déclenchement de biais minimum.

Le dernier sous système, beaucoup plus simple, correspond à la détection des particules arrivant sur le mur de temps de vol TFW. Etant donné que cet hodoscope est positionné de telle façon à couvrir la région où seules les particules π^- peuvent être émises, une simple détection sur ce mur produit le signal de déclenchement de ce sous système.

Le système maître prend en considération les différentes combinaisons de ces trois sous systèmes et spécifie la procédure que devra suivre le système d'acquisition. Chaque événement ainsi sélectionné par le système maître est marqué par son type de déclenchement. Lors de l'expérience réalisée en octobre 2009, l'ensemble du système d'acquisition et du système de déclenchement permit d'atteindre un taux d'événements enregistrés de 2,5 kHz. Ceci a permis la prise de 2 To de données sur l'ensemble des 8 jours de l'expérience.

Développement et performance du code d'analyse

Une importance particulière a également été donnée au développement du code d'analyse permettant de reconstruire les hypernoyaux. Ce code d'analyse se base sur les bibliothèques de ROOT, ainsi que plusieurs algorithmes pour la reconstruction des traces. En utilisant la méthode globale de la transformée de Hough, il est tout d'abord possible de trouver les traces potentielles. La trajectoire de chaque trace reconstruite est calculée et ajustée par un filtre de Kalman avec une résolution en impulsion d'environ 1 %.

L'identification des particules est ensuite effectuée grâce à la reconstruction de leurs traces et de la mesure de leur temps de vol. La corrélation entre la perte d'énergie dE et l'impulsion P/Z permet de séparer chaque particule : p, d, ^{3}He, ^{4}He à ^{6}Li. Pour les particules légères π^-, π^+, K^+, p, la corrélation entre la quantité $1/\beta$ (où $\beta = v/c$, est la vitesse de la particule normalisée à celle de la lumière) et l'impulsion P/Z est utilisée pour mieux distinguer chacune d'elles.

La reconstruction des hypernoyaux s'effectue en sélectionnant les possibles particules filles π^- et le fragment correspondant et en calculant la masse de ceux-ci en utilisant la formule de masse invariante suivante : $M_{hyp} = \sqrt{(\sum E_{decay})^2 - \| \sum \overrightarrow{p}_{decay} \|^2}$.

Pour chaque candidat hypernoyau, son vertex secondaire est aussi calculé permettant une meilleure sélection. À partir des simulations Monte Carlo, il a été possible d'estimer la résolution en masse de chaque hypernoyau ainsi que la résolution sur le vertex secondaire. La résolution en masse invariante des hypernoyaux est estimée à 2,23, 2,07 et 2,09 MeV pour, respectivement, les hypernoyaux ${}^3_\Lambda$H, ${}^4_\Lambda$H et ${}^5_\Lambda$He. Les différents critères de sélection des hypernoyaux ont été étudiés. sur des événements simulés. Suivant la sévérité des coupures imposées lors de la reconstruction, la proportion de bruit de fond par rapport au signal des hypernoyaux varie, permettant ainsi de déterminer un premier jeu de sélection possible sur les données réelles.

Premiers résultats

A partir des données obtenues durant l'expérience, plusieurs analyses plus ou moins complexes ont été réalisées afin de vérifier les performances de chaque détecteur.

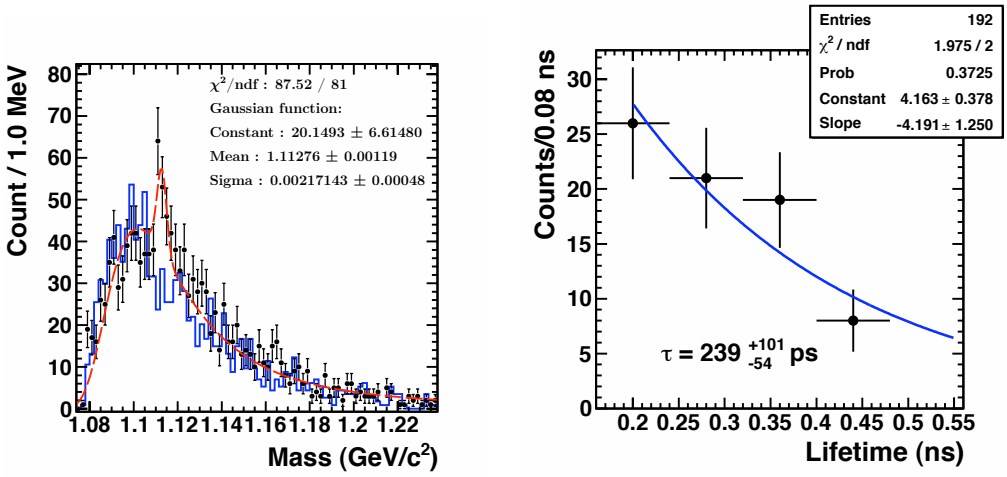

Figure 0.2.: Distribution de masse invariante des candidats de l'hypéron Λ (à gauche). Les points en noir représentent les données analysées et l'histogramme en bleu correspond à la contribution du bruit de fond combinatoire évaluée avec la méthode des événements mélangés. Le pic à 1,113 GeV/c^2 correspond aux hypérons Λ reconstruits. La distribution mesurée est ajustée par une combinaison d'une fonction polynomiale d'ordre 5 et d'une distribution gaussienne. La distribution du temps de vie des hypérons Λ ainsi reconstruits (à droite) est ajustée par une fonction exponentielle.

Une version simplifiée du code d'analyse de reconstruction des traces a permis de mettre en évidence la possibilité de reconstruire l'hypéron Λ. La figure 0.2 montre le spectre de masse invariante de $\Lambda \rightarrow \pi^- + p$ obtenu par cette version simplifiée. Les données reconstruites sont représentées par les points noirs, tandis que l'évaluation du bruit combinatoire par la méthode d'événements mélangés est représentée par l'histogramme en bleu. Le spectre de masse invariante a été ajusté par une combinaison d'une fonction polynomiale d'ordre 5 pour le bruit et d'une distribution gaussienne correspondante au signal de l'hypéron Λ. La masse ainsi estimée est de 1,1128 GeV/c^2 avec une déviation standard de 2,2 MeV/c^2. La significance du signal, $S/\sqrt{S+B}$, est de 4,2 σ. Un ajustement exponentiel de la mesure du temps de vie des candidats Λ, présentée dans la figure 0.2 (à droite), donne une estimation de 239^{+101}_{-54} ps. Les valeurs connues de masse et de temps de vie de l'hypéron Λ sont respectivement 1,115 GeV/c^2 et 263,1 $\pm$ 2 ps [103]. Les déviations par rapport aux valeurs de référence sont suffisamment faibles pour considérer que ces mesures indiquent bien la présence de l'hypéron Λ dans les données enregistrées.

La première tentative de reconstruction d'hypernoyaux a été réalisée en considérant le cas de ${}^{5}_{\Lambda}$He. La décroissance à 3 corps ${}^{5}_{\Lambda}\mathrm{He} \rightarrow \pi^- + \mathrm{p} + \alpha$, permet d'être moins sensible au

bruit de fond combinatoire lors de la reconstruction de la masse invariante. Cela est du à une plus grande sélectivité sur la présence du vertex secondaire.

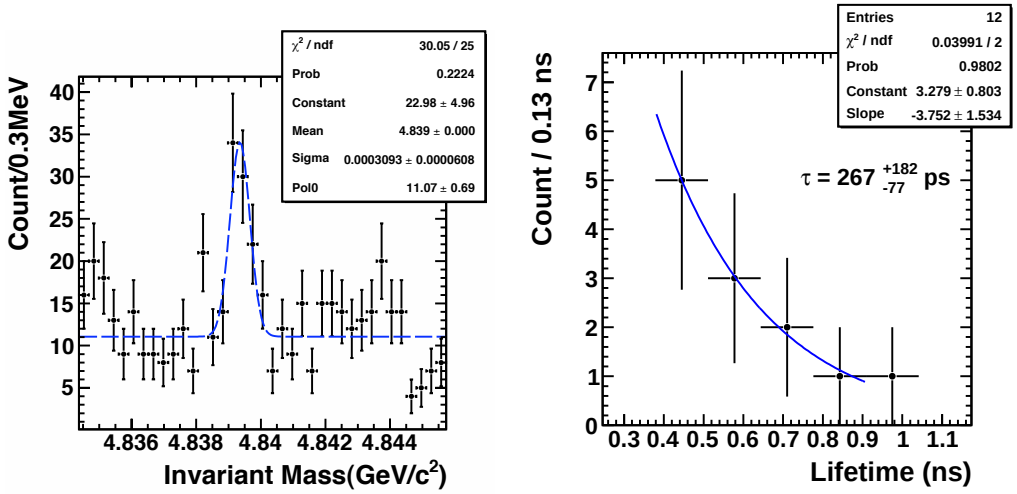

Figure 0.3.: Distribution de masse invariante des candidats de l'hypernoyau ${}^{5}_{\Lambda}$He (à gauche) et la distribution associée du temps de vie (à droite). L'ajustement de la distribution de masse invariante est présenté, et la valeur moyenne de l'ajustement gaussien est de 4,8394 GeV/c^2.

La figure 0.3 rassemble le spectre de masse invariante de ${}^{5}_{\Lambda}$He (à gauche) ainsi que la mesure de son temps de vie (à droite). Un ajustement de la distribution de masse invariante combinant une distribution gaussienne et un polynôme constant donne une valeur moyenne de 4,8394 GeV/c^2 avec une déviation standard de 3,1 MeV/c^2. Cette estimation est consistante avec la valeur de référence 4,8399 GeV/c^2. La significance du signal est de 5,6σ. La mesure du temps de vie a été réalisée sur 12 candidats ${}^{5}_{\Lambda}$He, sélectionnés par de conditions strictes afin d'éviter toute contamination par le bruit. L'ajustement exponentiel de la mesure de temps de vie donne une estimation de 267^{+182}_{-77} ps. Les larges barres d'erreur sont dûes au petit nombre de candidats utilisés. La valeur obtenue est en accord avec les valeurs déjà connues de 256 $\pm$ 20 ps et 278 $^{+11}_{-10}$ ps [105, 106, 107, 108, 109, 110].

Cette première tentative de reconstruction d'un hypernoyau a réussi à montrer la première signature de la présence de l'hypernoyau ${}^{5}_{\Lambda}$He. De meilleurs résultats sont attendus quand l'ensemble des données disponibles sera exploité, sachant que seule une petite fraction (environ 1 %) a été analysée dans ce travail. Cette première signature d'un hypernoyau est une bonne indication de la faisabilité de cette nouvelle approche expérimentale dans l'étude des hypernoyaux. Cela ouvre de nouvelles perspectives pour la recherche d'hypernoyaux lourds et proches des limites de stabilité.

Introduction

The interest in strangeness production in nuclear and hadron collisions has been growing during the last decade. From the standard nuclear matter composed by ordinary nucleons, formed by triplets of the two lightest d- and u-quarks, the strange (s) quark is necessary to be considered in order to understand the properties of the dense matter [1, 2]. Even in nucleons, which do not contain any strangeness as a constituent, the strange-quark from the quark-antiquark sea contributes to the form factor of the nucleon [3].

Strangeness has been mainly studied through light hadrons, which are particles made of a doublet or triplet of the s-, d- and u-quark [4, 5]. Strange hadrons play an important role in understanding the dense matter, from heavy ion reactions to the nature of stellar objects. In heavy ion physics, it has been demonstrated that strangeness production was one of the first observables suggested as a possible signature of the Quark-Gluon Plasma (QGP) [2]. On the other hand, strange baryonic matter is considered to be stable in very neutron-dense environment, such as in the core of neutron stars [6].

The study of hot and dense matter and its relation with the nuclear equation of state (EoS) has been a central question for years, from phenomena as nuclear multifragmentation [7, 8], collective flow [9, 10] to the particle production at the subthreshold energy region [11, 12]. The effects of strangeness have to be included to investigate the equation of state of dense nuclear matter [13]. Typical examples are the properties of neutron stars, such as the relationship between the mass range and the mass-radius which are profoundly connected to the underlying nuclear matter equation of state for a wide range of densities [14]. When the density increases, the degree of freedom offered by the strangeness appears

in addition to the ordinary nuclear matter. The strange baryonic matter can be composed of nucleons, their resonance states and strange baryons called *Hyperons* (Y), which are important components of the EoS of hyperonic matter to understand the special properties of neutron stars [15].

The interactions between baryons under those conditions have to be comprehended in order to model a proper EoS of the baryonic matter. Both the nucleon-nucleon (NN) and the hyperon-nucleon (YN) interactions need to be studied to be fully understood within the strong interaction group, $SU(3)_f$. The nucleon-nucleon (NN) interactions have been studied for several decades via nuclear scattering experiments providing enough data to adjust the nucleon-nucleon force parameters. The baryonic interactions involving strangeness have been very difficult to study because of the short lifetime of hyperons. This difficulty leads to a lack of hyperon-nucleon (YN) scattering experimental data. Furthermore, there are very sparse experimental data for the hyperon-hyperon (YY) interactions available nowadays. Meanwhile, it has been demonstrated that a bound system of nucleons and hyperons can be a key feature to study those YN and YY interactions [16]. The bound system of nucleons and hyperons is called a *Hypernucleus*.

Hypernuclei have been investigated by induced reactions of meson- or electron beams on stable target material, granting access to elementary processes of strangeness production or strangeness exchange. However, only hypernuclei close to the beta-stability region have been produced and studied so far [17].

In addition to this well established method for hypernucleus studies, the HypHI collaboration intents to introduce a new experimental approach. The HypHI project aims to study hypernuclei by means of collisions of stable heavy ion and rare isotope beams on stable target materials. These hypernuclei are formed by coalescence of a Λ-hyperon, which is produced in the participant region of the collision, in a projectile spectator fragment. They are therefore produced with a rapidity close to that of the projectile. This production mechanism gives a unique opportunity to investigate hypernuclei and their decay at extreme isospin and to directly measure hypernuclear magnetic moments.

As a first step of the HypHI project, the Phase 0 experiment was performed in August and October 2009 at the GSI Helmholtz Centre for Heavy Ion Research (Darmstadt, Germany) using a ^{6}Li beam at 2 A GeV impinged on a ^{12}C target. The aim of this first experiment is to demonstrate the feasibility of hypernuclear spectroscopy with heavy ion beams by identifying ${}^{3}_{\Lambda}$H, ${}^{4}_{\Lambda}$H and ${}^{5}_{\Lambda}$He hypernuclei from their mesonic weak decay modes.

The present thesis represents the achievement of this Phase 0 experiment. Several important steps have been undertaken: the design of the experimental apparatus through detailed Monte Carlo simulations, construction and commissioning of the different detector components, the development of the experimental trigger system as well as the online analysis software and the reconstruction (tracking) software and finally the data analysis and the production of the first preliminary results.

An introduction to the hypernuclear physics is presented in Chapter 1. Perspectives that hypernuclear study can induce are discussed as well. Previous hypernuclear experiments and their main results are summarized. The next generation of experiments planned in the future is also briefly discussed at the end of the chapter.

Chapter 2 is dedicated to the physics processes on which the HypHI project is based on. The models describing heavy ion collisions are presented, and theoretical aspects of the hypernuclear production are underlined. Physics prospects of the HypHI project are then expressed.

The first experiment of the project (the Phase 0 experiment) is presented in Chapter 3. The physics motivations are detailed and the experimental setup used in this experiment is described.

Chapter 4 gathers the details of the design of one of the new detectors built especially for the experiment: a Time-of-Flight wall dedicated to the detection of positively charged particles. The achieved performances during the experiment are presented and compared to the design expectations. The full optimization of the complete apparatus via Monte Carlo simulation is presented as well.

The design, development and implementation of the data acquisition and trigger systems are discussed in Chapter 5, and in particular, details on the different trigger parts are presented. The trigger is one of the crucial challenges for this experiment since the hypernuclear production cross section is seven orders of magnitude lower than the total reaction cross section.

Chapter 6 is dedicated to the development of online and offline analysis software of the experiment. The methods of track reconstruction developed for the offline analysis are presented in details. A good momentum resolution is a crucial pre-requisite for a high precision spectroscopy. Therefore sophisticated tracking methods have been implemented. In the last part of this chapter, the event reconstruction method is presented and the results

of the reconstruction with simulated data are summarized. The background rejection study is described and the expected performances of the experiment are given as well.

In the last chapter (Chapter 7) the first preliminary results of the experiment are reported. Important information of calibrated data for the event reconstruction procedure is given. The results of the reconstruction of Λ-hyperon candidates are reported as well as the first results of ${}^{5}_{\Lambda}$He hypernucleus candidates. To conclude this work, the future expectations from the experimental data are emphasized. Perspectives on hypernuclear physics are presented, and in particular, the future of the HypHI project and the J-PARC experiments is discussed.

1 Introduction to hypernuclear physics

Hypernuclear physics offers a unique opportunity to look into the properties of the hyperon-nucleon and hyperon-hyperon interactions. A bound system of nucleons and hyperons can be investigated as a micro-laboratory to study those interactions.

1.1. Aims of hypernuclear physics

1.1.1. Physics of hyperons

Hyperons are part of the light baryon group which can be generated from the flavor SU(3) group of the three light quarks u, d, s. The distinction of those three quarks is provided by the energy scale, $\Lambda_{QCD} \approx 217$ MeV, at which QCD becomes strongly coupled. Indeed, their masses are slightly inferior to Λ_{QCD} while c-, b- and t-quarks are clearly superior.

The two diagonal generators I_3, the 3^{rd} component of the isospin, and the hypercharge Y can be used to represent the $SU(3)_f$ group. They are defined by the relation of Gell-Mann-Nishijima [18, 19] in a way of:

$$Q = I_3 + Y/2 = T_3 + (B + S)/2 \tag{1.1}$$

where B corresponds to the baryon quantum number, S to the strangeness and Q to the charge.

Every light baryons inside of the flavor SU(3) group can be labeled by their quantum numbers I_3 and Y. Figure 1.1 represents the ground states of the octet of baryons of spin 1/2 and the decuplet of baryons of spin 3/2. The hyperons are baryons which have a non-null strangeness degree of freedom. The first generated hyperons are the isospin singlet Λ and isospin triplet Σ particles which include one s-quark, followed by the doublet Ξ particles including an additional s-quark.

Masses of hyperons differ from the mass of nucleon because the $SU(3)_f$ symmetry is broken due to the large difference between the masses of u, d and s quarks.

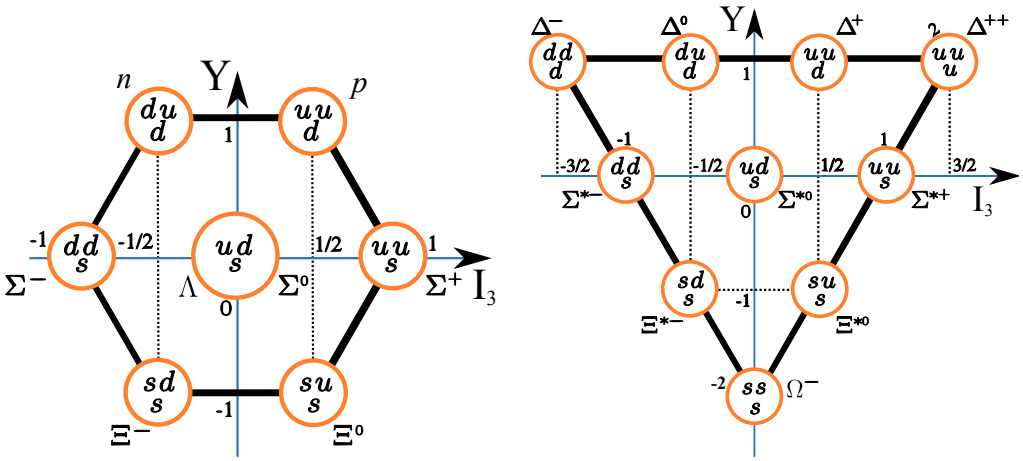

Figure 1.1.: Baryon octet and decuplet under the $SU(3)_f$ which are built from the combination of d-, u-, s-quarks.

Λ, $\Sigma^{-,+}$, $\Xi^{-,0}$, Ω^- have a lifetime around 10^{-10} s. They decay due to the weak interaction, by involving generally a pion emission. Those decay branches are called mesonic weak decays. However, the Σ^0 hyperon decays via a γ emission associated with a Λ particle. The resonance states shown in the decuplet of baryons of spin 3/2 decay due to the strong interaction. The mean free path $c\tau$ varies from 2.4 cm up to 8.71 cm depending on the kind of hyperons.

The baryon-baryon interaction within $SU(3)_f$ is described by 64 vertices, and only NN interactions are well known from the nuclear scattering experiments and are well explained by the one meson exchange theory. The 60 remained vertices corresponding to YN and YY interactions are difficult to be studied by scattering experiments. The difficulty is to produce a workable hyperon beam with a suitable energy for scattering experiments. Moreover, a target made of hyperons is impossible to produce due to their short lifetime.

However, It has turned out that hyperons can be bound inside a nucleus and that the interaction involving hyperons can be studied with such a bound system. A hypernucleus is a bound system of neutrons, protons and one or more hyperons. They are denoted by ${}^{A}_{Y}Z$ which corresponds to a hypernucleus with a charge number Z, a total baryon number A and with a kind of hyperon Y. The structure of a hypernucleus can be affected and described by the nature of the elementary YN and YY interactions. The first studied hypernuclei have been the Λ-hypernuclei, made of nucleons and Λ particle(s).

For a hypernucleus that contains only one Λ particle, the binding energy of the Λ can be expressed with the charge number Z and the neutron number N as:

$$B_\Lambda = M({}^{A-1}Z) + M_\Lambda - M({}^{A}_{\Lambda}Z) \tag{1.2}$$

where $M({}^{A-1}Z)$ is the mass of the nucleus without the hyperon and $M({}^{A}_{\Lambda}Z)$ is the total mass of the hypernucleus. For heavier nuclei around A=120, the Λ binding energy is saturated at around 25 MeV [20, 21].

1.1.2. From nuclear to hypernuclear physics

The study of a Λ-hypernucleus provides information about the strength of the YN interaction [16]. So far, the nature of the hyperon-hyperon (YY) interaction is not known, however, it could be studied via double Λ hypernuclei.

There are very few double Λ hypernuclear data and thus the interaction between pairs of hyperons is not constrained experimentally. Depending on the strength of the YN interaction, the core of a neutron star may be composed of hyperons, strange quark matter, or kaon condensates as shown in Figure 1.2 [22]. The YN interaction has then a crucial role for understanding the structure of neutron stars. One of the interests in the hypernuclear physics is related to this unsolved question of the neutron stars [14, 23].

Neutron stars are created as a result of the collapse of the core during supernova explosions. These compact but massive objects have a typical radius of about 10 km and masses of $1-2\mathrm{M}_\odot$, where $\mathrm{M}_\odot$ denotes the mass of the Sun. Nuclear matter inside the core of a neutron star is compressed to an extreme density, which is several times the normal nuclear density, $\rho \gg \rho_0 = 3 \cdot 10^{14}\mathrm{g/cm}^3$. Free hyperons are unstable and decay through the weak interaction, although the conditions in neutron stars can inverse this process

and allow the conversion of nucleons into hyperons. The hyperon formation turns out to be then energetically favorable. The equation of state which includes only interactions of nucleons gives a model for the neutron star which does not properly reproduce the astrophysical measurements [23]. Considering the presence of hyperons significantly softens the equation of state of dense hadronic matter. For example, this leads to a prediction of a lower neutron star mass, which is closer to the measurements than the predictions with only nucleons. [23]

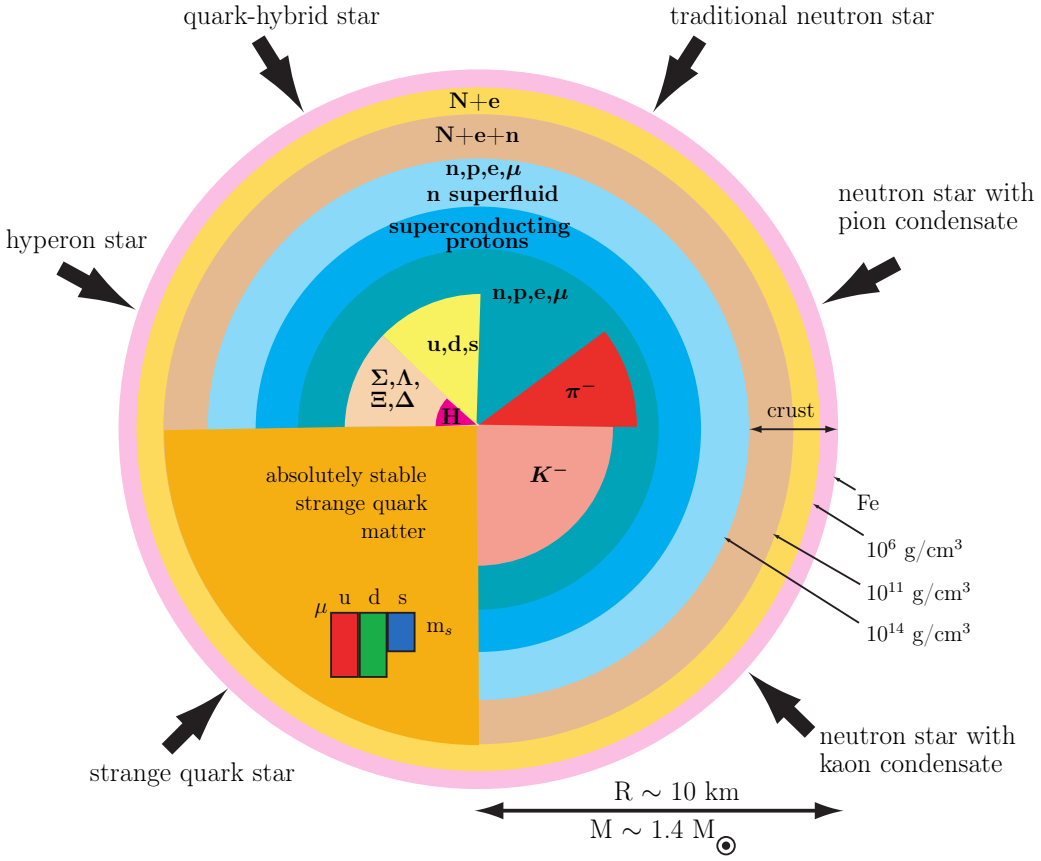

Figure 1.2.: Competing structures and novel phases of subatomic matter predicted by theory to make hyperon appearance in the core of neutron stars [22].

1.1.3. Properties of hypernuclei

Inside a baryonic system with nucleons, all nucleons are subjected to the Pauli exclusion principle.

When a Λ hyperon is included, it does not suffer from Pauli blocking like the other nucleons and penetrates deeply in the nuclear system. Thus, the Λ hyperon can occupy

orbitals such as s- and p-states which are very far away from the Fermi surface of nucleons. Therefore, it turns out that deeply bound orbitals inside of the nucleus can be studied with a hyperon as a probe. Furthermore, the hyperon-nucleon and nucleon-nucleon interactions can be studied via the weak decay of hypernucleus, which occurs in a similar way as the hyperon mesonic weak decay.

The study of the weak decay of a Λ-hypernucleus aims to understand the stability of the system and how the many-body nuclear system affects particles of the Λ decay. Moreover, the decay process also reflects the influence of the medium on the Λ-hyperon itself and on the weak interactions [24].

In addition to the mesonic weak decay similar to the one of hyperons, hypernuclei have a second type of weak decay which is non-mesonic.

Modes of the decay of a Λ-hypernucleus can be summarized as follow:

- the mesonic weak decay, which corresponds to the emission of a meson (π) [25]:

$$\Lambda \rightarrow N + \pi \tag{1.3}$$

  which is the free decay of the Λ-particle but now occurring in the medium;

- the non-mesonic weak decay (NMWD), described by the following process [26]:

$$\Lambda + N \rightarrow N + N \tag{1.4}$$

  which is only possible in a nucleus.

In the process of mesonic weak decay (1.3), the Q-value is about 40 MeV and corresponds to the mass difference between Λ and its decay products. When the decay occurs, the transfered energy is mostly carried by the pion. The outgoing nucleon remains with about 5 MeV of energy ($Q_{value} \times m_\pi/(m_N + m_\pi)$). Thus, its momentum arises to be:

$$p_N = \sqrt{2\, m_N E_N} \approx 100 \text{ MeV/c} \tag{1.5}$$

which is less than the Fermi momentum $k_F \approx 270$ MeV/c. The mesonic weak decay in nuclei is thus considerably restrained by the Pauli principle. Therefore, for heavy hypernuclei such a decay mode is suppressed.

On the other hand, the non mesonic weak decay is not concerned by the Pauli blocking. In this process, the Q-value is around 176 MeV. Considering this energy to be equally shared between the two nucleons, the nucleon momentum during the decay is:

$$p_N = \sqrt{2\, m_N E_N} \approx 400 \text{ MeV/c} \tag{1.6}$$

which is much larger than the Fermi momentum k_F, thus the two nucleons can escape from the residual nucleus. With such a large momentum transfer, it is possible to investigate the interaction at short distances.

It can be noticed that the non mesonic weak decay, $\Lambda N \rightarrow NN$, is the equivalent of the NN scattering process, $NN \rightarrow NN$, used to study ordinary nuclei. While the NN scattering process gives only access to the parity violating part of the weak interaction, the study of the NMWD grants access also to the parity-conserving part, which is not masked by the strong interaction as in the weak $NN \rightarrow NN$ reaction.

1.2. State of the art of hypernuclear physics

1.2.1. Known hypernuclei

The first hypernucleus was discovered by Danysz and Pniewski in 1953. It was formed in a cosmic ray interaction in a balloon flown-emulsion plate [27]. Since this first discovery, several stages of investigation have been undergone. Figure 1.3 shows all the Λ hypernuclei known until now [17]. The investigation methods used to discover these hypernuclei are indicated in the figure.

In the beginning, hypernuclei were studied via emulsion experiments. The binding energy of light Λ hypernuclei ($A \leqslant 16$) has been measured from their weak decay. It was found that the Λ potential depth is about 2/3 of the potential of the nucleon [28, 29]. However, data were limited to the binding energies of ground states, and excited states could not be investigated.

The second stage of investigation was started during the 70's with several spectroscopy experiments using K^- beams at CERN and later at Brookhaven National Laboratory (BNL). Those studies accessed the excited states of hypernuclei by the (K^-, π^-) reactions.

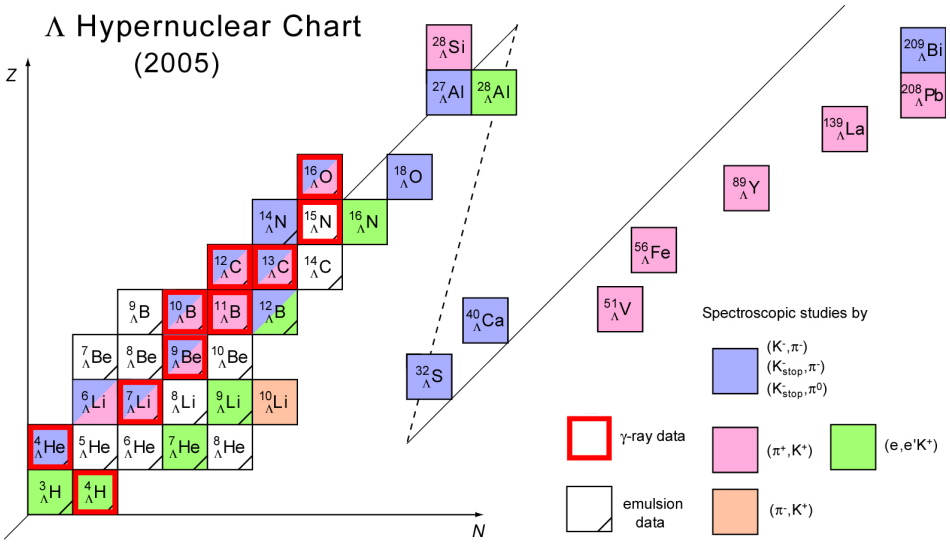

Figure 1.3.: Λ hypernuclear chart. It shows the experimentally identified Λ hypernuclei and the experimental methods used to study them (reaction spectroscopies of (K^-, π^-), (π^+, K^+), $(e, e'K^+)$, γ spectroscopy, and the emulsion method) [17])

An in-flight (K^-, π^-) reaction has been used in which a recoilless condition was introduced. The structure of p-shell hypernuclei was studied and the spin-orbit splittings were found to be quite small [30, 31]. Those experiments using the (K^-, π^-) reaction suffered from the low kaon beam intensity which affected the statistics of the experimental data.

The third stage began in the middle of the 80's with a new method of production. The (π^+, K^+) reaction was used at the Alternating Gradient Synchrotron (AGS) of BNL [32, 33] and then at the Proton Synchrotron (PS) of the High Energy Accelerator Organization (KEK) [34, 35, 36, 37]. For the past decade, this technique has been applied broadly to investigate many Λ hypernuclei with very high quality measurements.

The (π^+, K^+) reaction offers a large momentum transfer to a produced Λ-hyperon, therefore, it is suitable to study higher spin states with larger excited energies. With the both (K^-, π^-) (π^+, K^+) reactions, the precision of the spectroscopy measurements have been carried out with a resolution of the order of the keV thanks to the use of a germanium detector array called Hyperball [38]. Those precise measurements have unveiled new information on the hyperon-nucleon interactions [17].

During this past decade, a new and important method for the hypernuclear production has been developed by using the $(e, e'K^+)$ reaction. The first successful $(e, e'K^+)$ spectroscopy measurements were properly carried out at the Thomas Jefferson National Accelerator

Facility (JLab) [39]. Λ hypernuclei in a wide mass range from ${}^{3}_{\Lambda}$H up to ${}^{208}_{\Lambda}$Pb were investigated during this three-stage period as summarized in Figure 1.3.

1.2.2. Models of hyperon-nucleon interactions

There are several models which can be applied to describe the structure of hypernuclei. In the following, two models will be briefly discussed as examples. One of them is to consider the N body problem within an effective interaction model with G-matrix calculations. A Λ hypernuclear wavefunction can be written as a core nucleus potential and a Λ hyperon. The hypernuclear Hamiltonian is then expressed as follows:

$$\boldsymbol{H} = \boldsymbol{H}_{\mathrm{CoreNucleus}} + t_{\Lambda} + \sum v_{\Lambda N}^{\mathrm{effective}} \tag{1.7}$$

where $\boldsymbol{H}_{\mathrm{CoreNucleus}}$ is the Hamiltonian for the core nucleus, t_{Λ} is the kinetic energy of the Λ hyperon and $v_{\Lambda N}^{\mathrm{effective}}$ describes the effective ΛN interaction. At first, the effective interaction can be considered from the two-body interactions in free space. One-boson-exchange models such as Nijmegen [40] and Jülich interactions [41] are widely used to describe the elementary two-body interactions.

A phenomenological approach of the effective interaction can be considered to model the structure of hypenruclei [42, 43]. The phenomenological formula which describes the spin-dependence for the ΛN effective interaction for p-shell Λ hypernuclei is specified by five radial integrals, denoted by Δ, S_{Λ}, S_N and T associated with the operators $\boldsymbol{s}_{\Lambda} \cdot \boldsymbol{s}_N$, $\boldsymbol{l}_{\Lambda N} \cdot \boldsymbol{s}_{\Lambda}$, $\boldsymbol{l}_{\Lambda N} \cdot \boldsymbol{s}_N$ and $S_{12} = 3(\boldsymbol{\sigma}_{\Lambda}\hat{\boldsymbol{r}})(\boldsymbol{\sigma}_N\hat{\boldsymbol{r}}) - \boldsymbol{\sigma}_N\boldsymbol{\sigma}_{\Lambda}$:

$$V_{\Lambda N}(r) = V_0(r) + V_{\sigma}(r)\ \boldsymbol{s}_{\Lambda}\,\boldsymbol{s}_N + V_{\Lambda}(r)\ \boldsymbol{l}_{\Lambda N}\,\boldsymbol{s}_{\Lambda} + V_N(r)\boldsymbol{l}_{\Lambda N}\,\boldsymbol{s}_N + V_T(r)\,S_{12} \tag{1.8}$$

with the $s_{\Lambda}\cdot p_N$ wavefunction for the spin-spin term $V_0(r)$, the Λ-spin-dependent spin-orbit term $V_{\sigma}(r)$, the nucleon-spin-dependent spin-orbit term $V_N(r)$ and the tensor term $V_T(r)$. Low-lying level energies of p-shell hypernuclei can be described with radial integrals over the $s_{\Lambda} \cdot p_N$ wave function for each of the five terms in Eq. 1.8. These integrals, denoted as $\bar{V}$, Δ, S_{Λ} , S_N and T , can be determined from p-shell Λ hypernuclear data, and then compared with theoretical predictions given by free ΛN interactions through G-matrix calculation.

1.3. Current and future experiments

1.3.1. Current spectroscopy experiments

As shown in Figure 1.3, a Λ-hypernucleus can be produced via several reactions. It is induced from a nucleon-hole hyperon-particle state (a nucleon in the target being converted to a Λ hyperon). The three typical reactions, (K^-, π^-), (π^+, K^+) and $(e, e' K^+)$ are elementary processes which involve either a strangeness exchange in the case of a kaon beam (K^-, π^-), or a strangeness production via $s\,\bar{s}$ creation, resulting to a Λ hyperon and a kaon.

Once a Λ-hypernucleus is produced in an excited state, it decays through strong, electromagnetic and weak interactions according to the nature of the states. Hypernuclear states in which a Λ hyperon is bound in an orbit above the p-shell are often nucleon unbound and decay by emitting nucleons. Even for high-lying Λ hypernuclear states above the nucleon emission thresholds, the calculated spreading widths are narrower than a few 100 keV, in contrast with the case of a nucleon deep hole state [44, 45]. This is because:

1. ΛN interaction is weaker than the nucleon-nucleon interaction,
2. ΛN spin-spin interaction is weak and therefore spin vector $p_N - h_N$ excitation is suppressed,
3. a Λ hyperon with zero isospin can excite only isoscalar $p_N - h_N$ modes of the core nucleus,
4. no exchange term with nucleons is required.

These characteristics make the widths of Λ-hypernuclear states considerably narrower than states in an ordinary nucleus at the same excitation energy.

1.3.2. Future double-Λ and Ξ hypernucleus experiments

There are several new facilities in which research topics on hypernuclei have been granted and especially about double strangeness hypernuclei, including double Λ or Ξ hyperons.

At J-PARC in Japan, several new experiments on hypernuclei have been planned [46, 47]. Double-Λ hypernuclei will be studied via a new generation of emulsion experiment. It

is expected to obtain a large statistics of emulsion data. Hundreds of new double-Λ hypernuclear events are presumed to be found.

High-precision hypernuclear γ spectroscopy is also one of the main hypernuclear physics programs. In a wide mass number range, hypernuclei will be studied mainly using the (K^-, π^-) reaction with intense K^- beams and the further upgraded Hyperball (Hyperball-J) [47]. Gamma-ray spectroscopy of double Λ hypernuclei is also planned [47] via the (K^-, K^+) reaction, giving the opportunity of spectroscopic study of Ξ-hypernuclei which will provide information on the ΞN interaction [47].

In the PANDA experiment at FAIR, bound states of Ξ^--atoms are expected to lead to the double Λ hypernuclei [48] via the production of low momentum Ξ^- hyperons and their capture in atomic levels. Indeed, the reactions $\bar{p} + p \rightarrow \Xi^-\bar{\Xi}^+$ and $\bar{p} + n \rightarrow \Xi^-\bar{\Xi}^0$ followed by re-scattering of the Ξ^- within the primary target nucleus will be used, and after stopping the Ξ^- in an external secondary target, the formed Ξ-hypernuclei would be converted into double Λ-hypernuclei.

1.3.3. Exotic single hypernucleus experiment: The HypHI project

A new method to perform precise hypernuclear spectroscopy with stable heavy ion beams and rare-isotope (RI) beams at GSI and towards FAIR has been proposed by the HypHI collaboration. It aims to study hypernuclei at extreme isospin and extreme strangeness as well as the hypernuclear magnetic moments. Until recently, hypernuclei have been investigated by induced reactions of meson- or electron beams on stable target material, granting access to elementary process of strangeness production or strangeness exchange. Thus, only hypernuclei close to the beta-stability region have been produced and studied, since the stable target nucleus used as a target in the experiments is converted to a hypernucleus.

In addition to this well established method, the HypHI project will study hypernuclei by means of collisions of stable heavy ions and RI beams on stable target materials. Thanks to this production mechanism, hypernuclei are produced around the projectile rapidity. They are formed by coalescence of a Λ-hyperon in the fragment. It gives an opportunity to investigate hypernuclei at extreme isospin since hypernuclei can be produced as a projectile fragment, which it is known to have a wide isospin distribution. It is the only

way to produce extremely proton- and neutron-rich hypernuclei. Furthermore, it is the only process to access to hypernuclei with more strangeness than two.

Because of the energy threshold of a Λ particle production ($\sim$ 1.6 GeV for an elementary reaction of $N\,N \rightarrow \Lambda\,K\,N$), the energy of the projectile should exceed 1.6 AGeV with nuclear collisions. Consequently hypernuclei must be studied in-flight. Stable heavy ion beams and RI-beams meeting this condition as above are available at GSI.

With this method, one can investigate hypernuclear magnetic moments, $\Lambda - \Sigma$ coupling in the nuclear matter, the production of hypernuclei close to the drip-lines, the decay of exotic hypernuclei, charge symmetry breaking ΛN interactions, Coulomb dissociation of loosely bound hypernuclei and hypernuclei with multiple-strangeness.

In the following chapters, the details on the physics motivations of the HypHI project will be presented and especially the first experiment of the project.

2 The HypHI project

The HypHI project aims to study hypernuclei with a new approach: an invariant mass spectroscopy with induced reactions of stable heavy ion beams and RI-beams on a stable target. In the present chapter, the concept of participant-spectator, used to describe relativistic ion collisions, is briefly introduced. The theoretical studies about the hypernuclear production in ion collisions, which has motivated the HypHI project, is then summarized. The basic ideas of the project are discussed and the main physics motivations are then defined.

2.1. A new approach of hypernuclear production

2.1.1. Relativistic nucleus-nucleus reactions and physics with spectator fragments

During the collisions of two nuclei, the nature of the reaction depends on the observable called the impact parameter b. It is an important observable to characterize the initial geometry of the nucleus-nucleus collision.

This observable corresponds to the distance between the straight line trajectory of the center of the two nuclei before their interactions. It gives information about the centrality of the collision. When the impact parameter is larger than the sum of both radii of the projectile and of the target nuclei, R_p and R_t, the reaction is mainly an elastic scattering process due to the Coulomb force. In this case, if a low beam energy provides an energy

in the center of mass frame close to the Coulomb barrier, the projectile is deflected by the Coulomb force. Results of elastic scattering experiments provide the information of the nuclear potential near the nuclear surface. However, at a large beam kinetic energy, this effect becomes negligible. Nuclear interactions start to play a role in the collision when the impact parameter is smaller than the sum of both radii, $R_p + R_t$.

In a peripheral collision which occurs at an impact parameter of the order of $R_p + R_t$, two types of processes should be considered. A process of deep inelastic scattering is dominant when the energy of the beam is less than few tens of MeV. In such a process, the nuclear system of both nuclei is conserved but exchanges energies between those two systems. Most of the kinetic energy is used to access excited collective modes such as rotation and vibration. As the impact parameter decreases, the overlap of the two nuclear potentials increases, and the two nuclei transfer more nucleons.

When the kinetic energy is larger than hundreds of MeV, the probability of formation of a composite-nucleus is predicted to be low. Instead, the most of the cross section is predicted to go into reactions which can be described in terms of a participant-spectator concept.

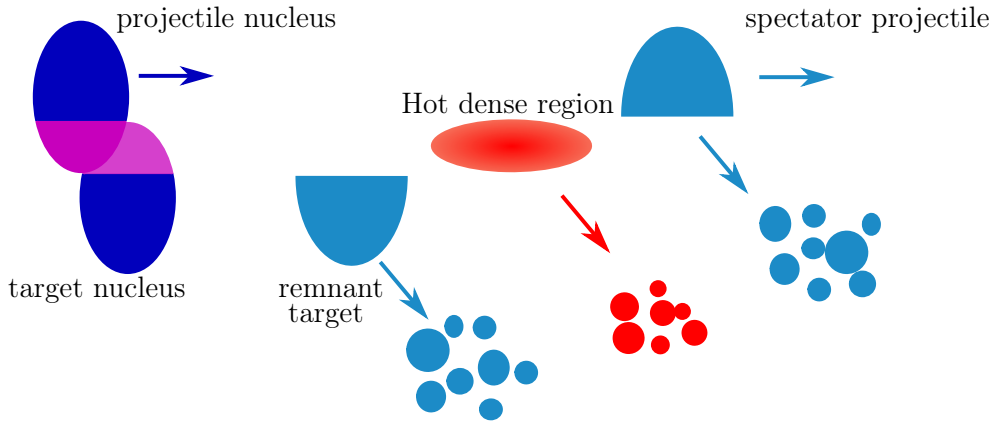

Figure 2.1.: The collision of a projectile nucleus with a target nucleus. The hot participant region is formed by nucleons from the overlapping region between the projectile and the target. At relativistic energies it induces three excited sources which are the projectile spectator, the remnant of the target nucleus and the hot participant region. Those sources decay into light particles and fragments.

Figure 2.1 schematically describes this scenario in which the geometrical overlapping region of nucleons of the projectile and of the target forms a hot and dense region called the participant region.

The property of the participant region depends on the impact parameter of the reaction; the number of nucleons and the energy density of the participant region increases in function of the centrality of the collision. Spectators, which are the target and projectile remnants, stay outside of the overlapping region.

Each of those three sources (projectile, and target spectators and the participant region) is excited and compressed because of an increase of temperature and density. The hot participant region decays via emission of light particles and intermediate mass fragments when it reaches the maximum of its compression.

The fact that the projectile fragments are emitted with a speed close to the beam velocity also has practical consequences for in-flight spectroscopy. This feature is one of the key roles in the hypernuclear spectroscopy with the HypHI project.

2.1.2. Processes for hypernucleus formation with heavy ion collisions

The formation of hypernuclei with heavy ion collisions was discussed in 1973 by Kerman and Weiss [49]. The production of exotic hypernuclei was especially emphasized. In this first investigation, the formation cross section of hypernuclei was roughly estimated. The formation process is modeled by the coalescence of the produced Λ, via $N + N \rightarrow N + \Lambda + K$, with a nucleus. The produced Λ was thought to have a large enough longitudinal momentum to be re-scattered at least once to be captured by the projectile spectator. Their flaw was that they did not include the momentum distribution of a Λ hyperon produced by nuclear collisions.

This problem has been solved by Wakai, Bando and Sano within several publications [50, 51, 52, 53]. The hypernuclear formation is modeled through a phase space coalescence between the spectator fragments and the hyperons from the participant region. From the hot participant region, hyperons are produced at the mid-rapidity region with a wide rapidity distribution being enough to overlap with the rapidity region of the target to the one of the projectile as illustrated in Figure 2.2. If hyperons are inside the fragment spectators and their velocities match those of the fragments, a hypernucleus can be formed [50].

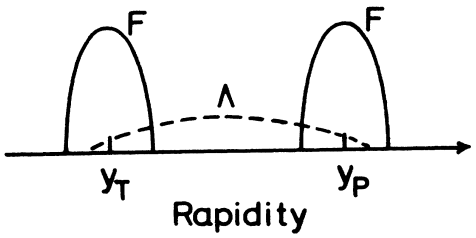

Figure 2.2.: Rapidity distribution of produced Λ hyperons and fragments (F) from the target (y_T) and the projectile (y_P) [51].

In this model, the hypernuclear production cross section is assumed to be factorized into a product of the cross section for hyperon production and fragment production as follows [51]:

$$\frac{\gamma}{\sigma_r}\frac{d^3\sigma^{(\Lambda F)}}{dk_c^3} = \left(\frac{m_\Lambda + m_F}{m_\Lambda m_F}\right)^3 S_{\Lambda F} \left(\frac{\gamma}{\sigma_r}\frac{d^3\sigma^{(\Lambda)}}{dk_c^3}\right)\left(\frac{\gamma}{\sigma_r}\frac{d^3\sigma^{(F)}}{dk_c^3}\right) \tag{2.1}$$

Where $k_c = (k_\Lambda + k_F)/(m_\Lambda + m_F)$ is the momentum per particle with $m_\Lambda = M_\Lambda/M_n$, $m_F = M_F/M_n$, $\gamma = (1 + (k_c/M_n)^2)^{1/2}$ and M_n is the nucleon mass.

The function $S_{\Lambda F}$ is the coalescence factor describing the probability of finding the produced Λ in the phase space region of the fragment. It includes terms corresponding to the spatial and the temporal distribution. By assuming the harmonic oscillator wave function for the produced Λ in the hypernuclei and a Gaussian form for the spatial extension of fragments and Λ-particle as $D^{(i)}(\mathbf{r}) = (\sqrt{\pi}\,\beta_i)^{-3}\,\exp[-(\mathbf{r}/\beta_i)^2]\,(i = \Lambda \text{ or } F)$, it has been demonstrated that $S_{\Lambda F}$ can be expressed as [51]:

$$S_{\Lambda F} = (2\pi)^3 \sum_{nl}(2l+1)\mathcal{S}_{\Lambda F} \tag{2.2}$$

with:

$$\mathcal{S}_{\Lambda F}(0s) = (\sqrt{\pi}\alpha)^{-3} \tag{2.3}$$

$$\mathcal{S}_{\Lambda F}(0p) = (\sqrt{\pi}\alpha)^{-3}(\beta_{\Lambda F}/\alpha)^2 \tag{2.4}$$

Where $\alpha = \sqrt{b_\Lambda^2 + \beta_{\Lambda F}^2}$ and $\beta_{\Lambda F} = \sqrt{\beta_\Lambda^2 + \beta_F^2}$ and b_Λ is the harmonic oscillator size parameter characterizing the Λ wave function in the hypernucleus. The expression of b_Λ is given by $((\hbar^2/M_\Lambda)/\hbar\omega_\Lambda)^{1/2}$. This expression of $S_{\Lambda F}$ only includes the effects of spatial

distribution. The expression which includes also the effects of temporal distribution is calculated in Ref. [51].

It has been also emphasized that secondary processes from (K, π) and (π, K) reactions have an appreciable production cross section for hypernuclear production because of the large production of K^- and π mesons in heavy ion collisions. In addition, it has been estimated that these secondary processes contribute to about 10% to 20% of the production mechanism of hypernuclei at energies of approximately 10 A GeV as the projectile energy [53].

The authors proposed several estimations of the total production cross section of hypernuclei. They evaluate the inclusive cross section of the Λ particle, $d^3\sigma^{(\Lambda)}/dk_c^3$, and of the cross section of nuclear fragments, $d^3\sigma^{(F)}/dk_c^3$ [52, 53]. Results are shown in Figure 2.3.

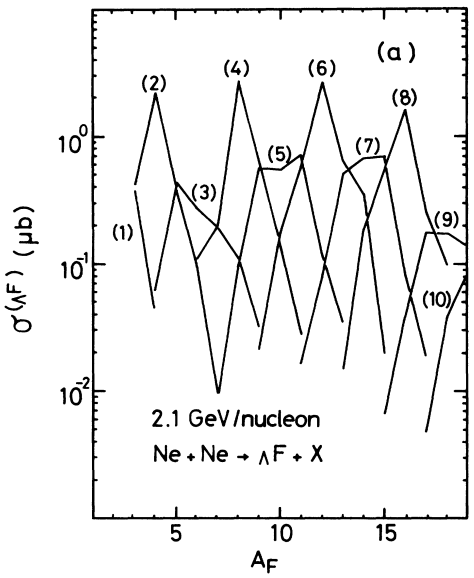

Figure 2.3.: Total production cross section of hypernuclei in Ne+Ne collisions at 2.1 A GeV as a function of the fragment mass number A_F. The number in parentheses corresponds to the atomic number Z [51].

2.2. Models of heavy ion collisions

2.2.1. Transport models

The reaction mechanism becomes more complex at high energies when heavy-ion projectiles are involved.

A major complication is introduced when multiple non-equilibrium processes occur during the evolution from the initial target-projectile contact to the equilibrated final state. The problem is frequently approximated by a two-step model that assumes a fast collision stage followed by statistical decay of the system at a much later time. The fast stage is described by models that attempt to account for mass and energy dissipation during the collision. The second stage is governed by statistical decay mechanisms such as particle evaporation and fission.

For heavy-ion reactions an additional complication with the intra-nuclei cascade model is that it ignores mean-field effects, which become relevant when there is extensive mixing of target and projectile nucleons. The dynamical evolution of a heavy ion collision can be described by a microscopic theory based on the Bolzmann-Uehling-Uhlenbeck (BUU) formalism. In this formalism the time evolution of the mean-field is described by a one-body density-distribution function that is solved simultaneously with a nucleon-nucleon collision integral, thus accounting for both the mean field and the N-N collisions. The collision integral is calculated via an intranuclear cascade. Pauli blocking is preserved in the theory.

This type of models has been proven to be effective to describe the multiplicities and spectra for energetic nucleons, as well as small-angle particle-particle correlations and integrated spatial distributions. However confronting theory with heavy residue data, several insufficiencies appear in BUU-type calculations. Firstly, the time at which thermalization has been achieved is unknown, and secondly, there is a lack of density fluctuations in the model that would provide a mechanism for the formation of nuclear clusters.

In an effort to develop a full dynamical theory of fragment production, density fluctuations have been incorporated via the classical quantum molecular dynamics (QMD) approach.

2.2.2. Event generators

In order to design the experimental apparatus of the HypHI experiments, Monte Carlo simulations have been performed. For the Monte Carlo simulations, the hypernuclear production with reasonable kinematics and cross section must be considered, and the hypernuclear events should be used to check the performance of the experimental apparatus and reconstruction methods. The generated events of background with the same theoretical background should also be used for the study of background rejection. For the stage of the design of the experiments, in the HypHI project, event generators based on the UrQMD model [54] and the GiBUU model [55] were used.

The UrQMD event generator was used to simulate the reaction of heavy ion collision for the kinematics of produced particles. Hypernuclear events are produced in a second step from the coalescence of produced Λ particles and fragments by a phase-space cut. While, the GiBUU transport model developed to simulate the formation of hypernuclei has been used to cross check the results of UrQMD and to estimate the production cross section.

UrQMD

In the molecular dynamics of the collision, the evolution of the N-body phase-space density, f^N, is given by the equation of Liouville :

$$\frac{df^N}{dt} = \{f^N, H^N\} + \frac{\partial f^N}{\partial t} = 0 \tag{2.5}$$

where $f^N(x_1, p_1, x_2, p_2, \cdots, x_N, p_N)$ includes the initial conditions of the Hamiltonian at N body, H^N.

For given initial conditions describing the system at a time t_0, one can write:

$$r_i = r_i(t = t_0) \text{ and } p_i = p_i(t = t_0)\ i = 1, \cdots, N \tag{2.6}$$

Where r_i and p_i are respectively the position and the momentum of the particle i.

The propagation of nucleons in the system is described by the Hamilton's equation of motion:

$$\dot{r_i} = \frac{\partial H^N}{\partial p_i} \text{ and } \dot{p_i} = -\frac{\partial H^N}{\partial r_i}, i = 1, \cdots, N \tag{2.7}$$

To apply this formalism to the heavy-ion collision, the model of molecular dynamics is extended to the model of quantum molecular dynamics QMD which includes the Fermi motion, the hard scattering and the Pauli blocking of the final state of the collision. The idea of the QMD model is to propagate nucleons in the phase-space:

$$f_i(r, p, t) = \frac{1}{(\pi\hbar)^3} \exp\{-\frac{(r - r_i(t))^2}{2L^2} - \frac{2L^2}{\hbar^2}(p - p_i(t))^2\} \tag{2.8}$$

where:

- r, $r_i(t)$ is the position in the coordinate space.
- p, $p_i(t)$ is the position in the momentum space.
- L is the theoretical width of the bunch of waves, a parameter which is not a physical observable and is determined so as not to influence the results of the model. [56]

The QMD model includes the 2-body and 3-body interactions of nucleons. Those nucleons evolve in an interaction potential which consists of the Coulomb force, the Yukawa potential, a local potential (with Skyrme parametrization of 2- or 3-body forces [57] with a dependence of the density directly linking to the equation of state) and one additional term which takes into account the momentum dependence of the interaction.

The reaction in the QMD model is a combination of binary collisions between nucleons within the Pauli blocking principle until the final state. Fragments are then formed at the equilibrium via coalescence in the phase-space.

Hybrid GiBUU+SMM

The theoretical description of hadron-nucleus and heavy-ion reactions is based on the semi-classical kinetic theory of statistical mechanics [58]. The covariant extension of this equation is the relativistic Boltzmann-Uehling-Uhlenbeck (RBUU) equation, [59] for the $f(x, k^*)$ 1-body phase space distribution function for the hadrons. In particular, nucleons,

hyperons and all resonances up to a mass of 2 GeV, as well as mesons, pions, kaons, are explicitly propagated. In the collision term the short-hand notations $f_i = f(x, k_i^*)$ for the particle and $\tilde{f}_i = (1 - f(x, k_i^*))$ for the hole distributions are used, with the 4-momentum $k^{*\mu} = (E_k^*, \vec{k})$:

$$\left[k^{*\mu}\partial_\mu^x + (k_\nu^* F^{\mu\nu} + M^*\partial_x^\mu M^*)\partial_\mu^{k^*}\right] \; f(x,k^*) = \\ \frac{1}{2(2\pi)^9}\int \frac{d^3k_2}{E^*_{\mathbf{k}_2}}\frac{d^3k_3}{E^*_{\mathbf{k}_3}}\frac{d^3k_4}{E^*_{\mathbf{k}_4}} W(k\,k_2|k_3\,k_4)[f_3\,f_4\,\tilde{f}\,\tilde{f}_2 - f\,f_2\,\tilde{f}_3\,\tilde{f}_4] \quad (2.9)$$

where $E^*_{\mathbf{k}} = \sqrt{M^{*2} + \mathbf{k}^2}$.

The collision integral exhibits explicitly the final state Pauli-blocking while the in-medium scattering amplitude includes the Pauli-blocking of intermediate states. The collision term includes 21 mesons and 60 resonances. We note that all elastic and inelastic processes, such as resonance production and absorption with associated meson production, are included.

In particular, inelastic processes with strangeness production are explicitly accounted for $BB \to BYK$, $B\pi \to YK$, $BK \to BK$ (with isospin exchange between K^0 and K^+), which are important for the production of hyperons. An exact solution of the set of the coupled transport equations for different hadrons is not possible. Therefore, the commonly used test-particle method for the Vlasov part is applied, whereas the collision integral is modeled in a parallel-ensemble Monte Carlo algorithm. The numerical implementation for the solution of Eq. 2.9 is the one of GiBUU. [60].

The formation of hypernuclei depends on the fragmentation process between nucleons, and in particular between nucleons and hyperons, which is taken into account in dynamical transport models.

It is well known that the fragmentation process cannot be dynamically described within transport models of Boltzmann-type, since, in such approaches, only one-body phase-space densities are calculated and the dynamical phase-space evolution of physical fluctuations is neglected. In situations with long time scales for the fragmentation process, such as spectator dynamics in heavy-ion collisions and dynamics in hadron-induced reactions, a statistical description of the fragmentation process can be applied.

The Statistical Multifragmentation Model (SMM), [61, 62], has been widely applied to multiple fragment production. In its standard version, SMM does not account for strangeness degrees of freedom. However, it has recently been attempted to extend the

statistical approach by including hyperons. The formation of spectator hypernuclei is obtained via the phase space coalescence model explained in Section 2.1.2. The theoretical calculations for ^{12}C+^{12}C collisions at 2 A GeV have provided the first estimation of production cross section from a dynamical model. Table 2.1 summarizes the total inclusive cross section obtained for $^{4}_{\Lambda}$H, $^{4}_{\Lambda}$He, and $^{5}_{\Lambda}$He hypernuclei. It includes also the portion of mesonic scattering process described in Section 2.1.2. Figure 2.4 shows the inclusive rapidity distributions of $^{3}_{\Lambda}$H, $^{4}_{\Lambda}$H, $^{4}_{\Lambda}$He, and $^{5}_{\Lambda}$He hypernuclei.

Table 2.1.: Inclusive production cross sections for different types of hypernuclei in reactions ^{12}C + ^{12}C at 2 A GeV [55]. The contribution from exclusive pion-nucleon scattering, $\pi\ N\ \rightarrow\ Y\ K$, is also shown .

	$^{4}_{\Lambda}$H	$^{4}_{\Lambda}$He	$^{5}_{\Lambda}$He
Total yield (μb)	2.2	4	1.4
Pionic contribution (μb)	0.3	0.2	0.03

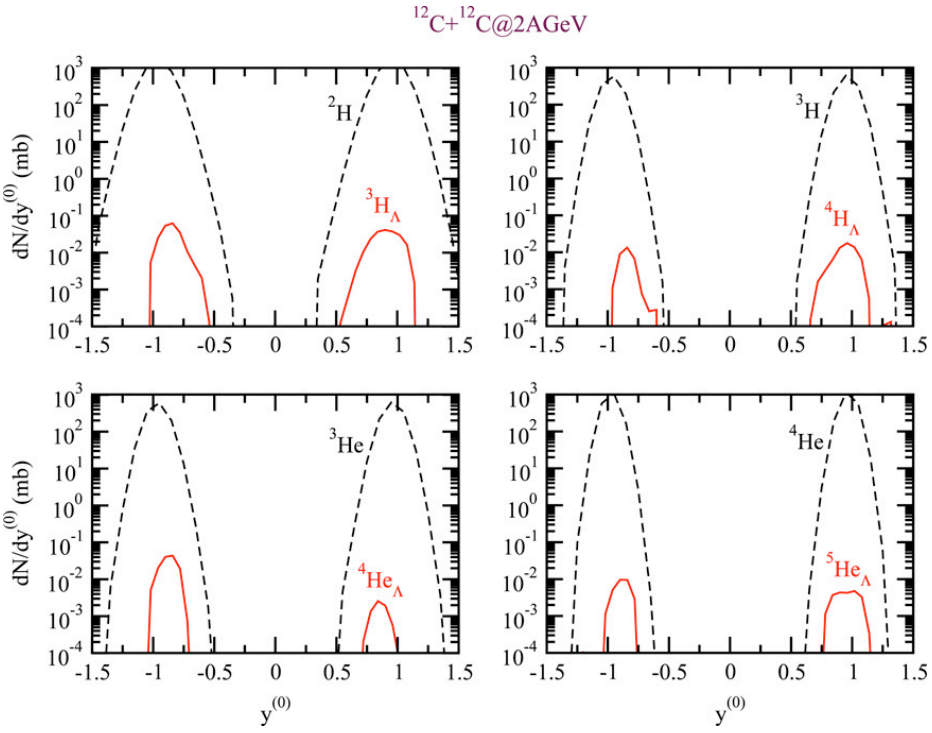

Figure 2.4.: Rapidity distributions as function of the rapidity $y^{(0)}$ (normalized to the projectile rapidity in the c.m. frame) of different particle types (as indicated) for the system ^{12}C +^{12}C at 2 A GeV [55].

2.3. Physics subjects with hypernuclear spectroscopy with heavy ion induced reactions

2.3.1. Extension of the hypernuclear landscape

Hypernuclei have been intensively studied via meson induced reactions such as (π^+, K^+) and (K^-, π^-) on stable targets. Those elementary processes produce only hypernuclei around the β-stability line. So far, only those hypernuclei have been studied, as explained in the previous chapter.

The investigation of the structure of ordinary nuclei has already extended the nuclear chart toward the proton and neutron drip-lines. However, hypernuclei toward the neutron and proton drip-line have still remained completely unknown because of the production mechanism which has been used so far. As the study of neutron or proton rich nuclei close to the drip-lines has expanded our knowledge of the nuclear structure, the study on hypernuclei toward the hypernuclear drip-lines will provide new opportunities to investigate the charge and isospin dependences of the YN interaction. For instance, in ΛN interactions, the possibility of a $\Lambda N - \Sigma N$ coupling in nuclear medium can introduce an isospin dependence in the ΛN interactions in which a free Λ has normally no isospin.

The hypernuclear proton-drip line has been reached only on the ${}_{\Lambda}$H, ${}_{\Lambda}$He and ${}_{\Lambda}$Li hypernuclei, and no hypernucleus has been found at the hypernuclear neutron-drip line. In single-Λ-hypernuclei, a Λ-hyperon is bound by occupying the 1s orbital, thus lowering the total energy of the hypernuclear system. As a result, the proton and neutron drip lines for Λ hypernuclei are expected to move toward the proton and neutron rich side, respectively [63].

The radii of Λ-hypernuclei are decreased in comparison to those of the core nuclei, which manifests the energy gain for binding more neutrons and the shrink of the nuclear shape. The calculation would indicate that the neutron drip-line of Λ-hypernuclei may be further away from the β-stability line than for ordinary nuclei.

A glue-like role of a Λ hyperon in neutron rich hypernuclei was also studied for Ne and Ca hyper-isotopes to the drip line within the relativistic mean field approach [64, 65]. It has been concluded that the region of stability is extended and the neutron drip line is shifted for Λ-hypernuclei with respect to ordinary nuclei [66].

One of the main goals of the HypHI project is to extend the hypernuclear chart to the proton drip line up to ${}_{\Lambda}$Si hypernuclei and neutron drip line up to ${}_{\Lambda}$Li hypernuclei

Exotic Λ hypernuclei may provide unique information on the charge symmetry breaking (CSB) $\Lambda - N$ interaction. In contrary to the N-N case, where this effect is masked by the Coulomb interaction, the CSB interaction is rather apparent in the $\Lambda - N$ pair due to zero Λ charge and isospin.

This subject is far from complete understanding. From the binding energy of ${}^{4}_{\Lambda}$H and ${}^{4}_{\Lambda}$He, it is deduced that $\Lambda - proton$ attraction is stronger than the $\Lambda - neutron$ one [24]. A larger CSB effect may be expected in very proton/neutron rich hypernuclei. It may cause a change in the difference between $\Lambda - proton$ and $\Lambda - neutron$ interactions which may induce the shift of positions of drip-lines. Therefore, it is expected that the study of neutron and proton drip lines in the hypernuclear landscape may provide information on CSB.

2.3.2. Hypernuclear magnetic moment

The history of nuclear physics shows that the electromagnetic matrix elements are sensitive to the wave functions of many body systems, and the magnetic moments of nuclei have been a driving force of various new ideas in nuclear theories.

The magnetic moments can be the most sensitive probes on the wave function of the Λ-hyperon in the nuclear matter. The magnetic moment could be sensitive to the spin and angular-momentum structure of hypernuclei, to the spin-dependent YN interactions, and to the shell structure of hyperons in hypernuclei.

It was revealed that the hyperon-induced configuration mixing is small. Experimental hypernuclear magnetic moments were predicted to be around the Schmidt lines based on the shell model calculations [67, 68], as expected by weak YN interactions. However, magnetic moments of hypernuclei could be different from the values on the Schmidt lines if there is an exchanging current from heavier mesons, $\Lambda - \Sigma$ coupling and the exotic phenomena of the Λ-hyperon in hypernuclei [69, 70]. For ordinary nuclei, the one meson exchange currents such as the pionic current and the delta excitation are significant in nuclear magnetic moments. For hypernuclei, kaons will play a similar role as pions. Measurements of the magnetic moment of hypernuclei could be the most relevant for searching for some unusual effects.

This measurement of hypernuclear magnetic moments is the ultimate goal of the HypHI project and is proposed to be performed with 20 A GeV heavy ion beams at the FAIR facility.

It has to be noted here that the access to the hypernuclear magnetic moments can be achieved only by studying hypernuclei as projectile fragments with heavy ion collisions since the hypernuclei must be separated and proceeded in the magnetic field in flight.

2.4. Aims of the HypHI project

In the following, several physics subjects of the HypHI project are summarized. In addition to the conventional hypernuclear spectroscopy with meson-beam and electron-beam induced reactions, the following subjects can be extensively studied with the HypHI projects [71]. They are:

- Hypernuclei toward the proton and neutron drip-lines,
- Magnetic moments of hypernuclei,
- $\Lambda - \Sigma$ coupling in the nuclear matter,
- Decay of exotic hypernuclei,
- Charge symmetry breaking in YN interaction,
- Coulomb dissociation of loosely bound hypernuclei,
- Measurements of the binding energy of exotic hypernuclei.

2.4.1. Phases and respective goals

The project consists of four distinguishable phases [71]:

Phase 0 : Pilot experiment at cave C as a proof of principle.

Phase 1 : Experiment at cave C at the current GSI facility.

Phase 2 : Experiments with the R^3B facility of the NUSTAR in FAIR.

Phase 3 : Experiments with a hypernuclear separator at 20 A GeV in FAIR.

The Phase 0 experiment aims to demonstrate the feasibility of precise hypernuclear spectroscopy with induced reaction of heavy ion beams by producing and reconstructing light hypernuclei. The Phase 0 experiment has already been performed. This work is dedicated to the design and conduct of the Phase 0 experiment. In the Phase 1 experiment, proton rich hypernuclei will be studied. The investigation of neutron rich hypernuclei will be continued at FAIR, as Phase 2. The R^3B experimental hall and its superconducting magnet will be employed in this phase, together with RI-beams from the super-fragment separator (super-FRS). As Phase 3 which is the main goal of the project, a magnetic separator of hypernuclei is to be developed to study hypernuclear magnetic moments, hypernuclei at drip-lines and hypernuclei with multi-strangeness.

The Phase 0 experiment has already been performed to demonstrate the feasibility of the hypernuclear spectroscopy with heavy-ion-beam induced reactions. Since the hypernuclear production with heavy-ion beam has not been well studied yet, the phase 0 experiment is to confirm the results of the previous experiments with streamer chambers at JINR in Dubna. The next phase will concentrate on the investigation of heavier hypernuclei than ${}_{\Lambda}$Li toward the hypernuclear proton drip line.

As for the last phase, the ultimate goal of the HypHI project is to measure directly hypernuclear magnetic moments and hypernuclei at drip lines. At FAIR, heavy-ions can be accelerated by SIS-100 to provide ion beams with energies close to 20 A GeV and hypernuclear spectroscopy with stable heavy-ion beams would be performed at those energies. Measurements of hypernuclear magnetic moments would then be reachable. At 20 A GeV, the Lorentz factor is $\gamma = 22.5$, therefore the lifetime of hypernuclei is longer, around $\tau_{eff} = 4.5$ns ($\gamma\beta\tau_{eff} = 1.35$ m). With a longer lifetime, hypernuclei can be selected and identified by spectrometers consisting of a superconducting bending magnet. In addition, in Phase 3, hypernuclei at nucleon drip lines as well as hypernuclei with multi-strangeness will be studied.

3 Phase 0 of the HypHI project

In this chapter, an overview of the experimental approach of the HypHI project is presented. The experimental challenges are summarized and in particular, the goals of the Phase 0 experiment are described in detail. The Phase 0 experiment focuses on the study of light hypernuclei, ${}^{3}_{\Lambda}$H, ${}^{4}_{\Lambda}$H and ${}^{5}_{\Lambda}$He, in order to demonstrate the feasibility of a precise hypernuclear spectroscopy by means of ion collisions. The methods used to study these hypernuclei of interest are introduced, and the experimental setup of the Phase 0 experiment is then described.

3.1. Aims and challenges

In Chapter 2, theoretical background of the production of hypernuclei in relativistic nucleus-nucleus collisions have been briefly emphasized. However, the experimental information on the hypernuclear production with heavy ion beams has remained rather poor. The Phase 0 experiment aims to overcome the experimental difficulty of the hypernuclear production at 2 A GeV of projectile energies.

3.1.1. Feasibility of a hypernuclear spectroscopy experiment with heavy ion beams

The production of hypernuclei by means of heavy ion induced reactions has been first theoretically studied by Kerman and Weiss [49]. Keman and Weiss indicate that it is

the only possible way to form hypernuclei with several units of strangeness and other exotic strange nuclei. In heavy ion collisions at high energy, the reaction mechanism is neither dominated by the coulombian effects anymore, nor by deep inelastic scattering. As discussed in Chapter 2, the concept of participant-spectator model is more appropriate to describe this reaction mechanism.

There is a participant region corresponding to the overlapping region between the two nuclei of the collision and a spectator region. This region represents nuclear parts which are not reacting and not enduring a large disturbance. In this participant region with a suitable initial energy of the projectile, hyperons such as Λ, Ξ or Σ particles can be produced via elementary processes like NN $\rightarrow \Lambda$KN or NN $\rightarrow \Sigma$KN.

Produced hyperons have a wide rapidity distribution because they are produced around the mid-rapidity region. Due to this wide rapidity distribution, hypernuclei can be induced by coalescence of a hyperon with a fragment of the projectile. The velocity of these induced hypernuclei will thus be close to the one of the projectile. With an energy higher than 1.6 A GeV, which is the energy threshold of elementary process of Λ production, produced hypernuclei should have a large Lorentz boost.

The expected velocity β is greater than 0.9, which means a Lorentz factor around 3 for a 2 A GeV projectile energy. The large Lorentz boost will increase their lifetime by the Lorentz factor. Decays of hypernuclei can thus be studied in-flight and will take place around 15-20 cm behind the target in case of $\gamma \sim 3$.

In 1988, hypernuclear production by heavy ion beams was investigated in Dubna [72, 73] with beams of 3.7 A GeV ^{4}He and 3.0 A GeV ^{7}Li on a polyethylene target. A production cross section for $^4_\Lambda$H was evaluated around 0.3 μb for a 3.7 A GeV ^{6}Li beam. Those experimental estimations have been reproduced by a theoretical calculation based on a model of a Λ coalescence in projectiles, as discussed in Chapter 2 [51, 52].

More recently, $^3_\Lambda$H has also been produced and identified with central 11.5 A GeV/c Au+Pt collisions by the BNL AGS E864 collaborations [74]. It should be noted that the AGS experiments studied light hypernuclei at the target rapidity region, while the HypHI experiments aim to study hypernuclei in the projectile rapidity region in order to drastically increase the level of confidence since the lifetime of the produced hypernuclei can only be measured with hypernuclei in flight.

Even though two experiments at JINR and BNL have estimated the production of hypernuclei with heavy ion beams, the feasibility of a precise hypernuclear spectroscopy with heavy ion beams has not been yet established experimentally. The study of this feasibility is the aim of the Phase 0 of the HypHI project. The Phase 0 will confirm results of the previous experiments focusing on ${}^{3}_{\Lambda}$H, ${}^{4}_{\Lambda}$H and ${}^{5}_{\Lambda}$He mesonic weak decay, but will also measure the non-mesonic weak decay of those selected hypernuclei, the coalescence factor, the possible ${}^{5}_{\Lambda}$He polarization and its π^- decay asymmetry, and the p, n, Λ radii inside of hypernuclei. The experimental setup of Phase 0 will be discussed in the following Section 3.2.

Very recently, the STAR collaboration of the Relativistic Heavy Ion Collider (RHIC) at Brookhaven National Laboratory has observed hyper-triton as well as anti-hyper-triton [75]. They performed an invariant mass spectroscopy in flight, and it shows significant hypernuclear invariant mass peak without any background subtraction. Furthermore, they reproduce the known lifetime of hyper-triton by measuring hypernuclear decay vertex displacement. In general, confidence level of the mass peak depends on the cut conditions in data analyses. For hypernuclear reconstruction with heavy ion beams, many cut conditions with kinematics have to be required in order to dig out the hypernuclear events from huge background events. Often, it has been demonstrated that a mass peak can be produced by miss reconstruction due to the cut conditions and improper background subtraction. However, if the lifetime measurement is available, one can confirm the mass reconstruction by checking the consistency of the measured lifetime to the known values. Furthermore, an event reconstruction requiring a secondary vertex can clearly select hypernuclear events in-flight, thus the result of the STAR experiment reveals hypernuclear reconstruction with confidence.

The way of the event reconstruction is very similar to the experimental concept of the HypHI project, which clearly demonstrates that it is the only way to look into hypernuclei in flight, being close at the projectile rapidity region, in order to perform hypernuclear spectroscopy with a reasonable level of confidence. It must be emphasized that hypernuclear spectroscopy with heavy ion beams on a fixed target can be confident only when the hypernuclei are reconstructed near the projectile rapidity region.

3.1.2. Invariant mass spectroscopy and secondary vertex measurement

In the past experiments with meson or electron induced reactions, the measurements of the residues were impossible because the residues do not escape the target. One can identify the residues by measuring gamma rays. However, this identification is usually difficult because of the low efficiency of gamma ray detections.

The gamma-ray measurements also require the pre-knowledge of the structures of the residual nuclei. However, they are not always known, leading to an ambiguity on the identification of residues.

With the experimental concept of the HypHI experiments, such as Phase 0, all particles from hypernuclear decay will be measured and identified thanks to the in-flight spectroscopy. Thus, it is possible to calculate the invariant mass of the hypernucleus from its daughter particles as in the equation 3.1,

$$M_{hyp} = \sqrt{(\sum E_{decay})^2 - \| \sum \overrightarrow{p}_{decay} \|^2} \tag{3.1}$$

Secondary decay vertices will be reconstructed with full information from tracker detectors up and downstream of a dipole magnet. Thus, hypernuclei and free Λ will be as well discriminated from the particles from the primary reaction which constitute the background for the hypernuclear reconstruction.

3.1.3. Decay channels of hypernuclei of interest

In the Phase 0 experiment, ${}^{3}_{\Lambda}$H, and ${}^{4}_{\Lambda}$H and ${}^{5}_{\Lambda}$He are to be produced by heavy ion collisions by using ^{6}Li projectiles at 2 A GeV.

Charged pionic mesonic weak decay (MWD) of these hypernuclei will be mainly observed, namely, ${}^{3}_{\Lambda}\mathrm{H} \rightarrow \pi^- + {}^{3}\mathrm{He}$, ${}^{4}_{\Lambda}\mathrm{H} \rightarrow \pi^- + {}^{4}\mathrm{He}$ and ${}^{5}_{\Lambda}\mathrm{He} \rightarrow \pi^- + {}^{4}\mathrm{He} + p$. These hypernuclei are expected to be produced with a velocity close to that of the projectile. The kaon production, which is associated to the hypernuclear production, corresponds to the strangness production in the participant region. Because of the large Lorentz factor of the relativistic hypernuclei, most of the hypernuclear decay takes place in-flight behind the target (the

mean decay path is expected to be around 15 cm, with $\gamma \sim 3$ if the mean-life at rest is about 200 ps). The trajectories of all charged particles emitted from and behind the target are measured. With the reconstruction of the secondary vertex behind the target, several observables will then be accessible:

- Production cross section of the ${}^{3}_{\Lambda}$H, ${}^{4}_{\Lambda}$H and ${}^{5}_{\Lambda}$He hypernuclei.
- Lifetime of ${}^{3}_{\Lambda}$H, ${}^{4}_{\Lambda}$H and ${}^{5}_{\Lambda}$He.
- Polarization of hypernuclei produced in heavy ion collisions.
- Coalescence mechanism in fragmentation reactions.

In addition to the main physics topic to demonstrate the feasibility of the hypernuclear spectroscopy, other topics will be studied as well. The non-mesonic weak decay of those light hypernuclei will be investigated like the decay branch of ${}^{4}_{\Lambda}$He $\rightarrow$ d + d. The π^+ emission of ${}^{4}_{\Lambda}$He may be also investigated via the ^{4}He $\rightarrow \pi^+ +$ n + ^{3}H decay channel. This decay mode has drawn the attention because the free Λ decay channels do not include a π^+ decay. Several theoretical explanations are possible, but still the π^+ emission puzzle is not solved. Another topic to investigate is the measurement of hypernuclear radius via the interaction cross section [76].

Furthermore, the non-mesonic weak decay of hypernuclei can be studied in detail with the HypHI experiment. In the former experiments with meson beams induced reactions, the measurement of the whole proton spectrum was not feasible because of the difficulty to measure the low energy protons due to the thick target in which hypernuclei are produced and stopped. In the HypHI experiment, since the hypernuclear decay products are emitted in the space behind the target where there is no material around the decay position, the measurement of the proton spectrum is not disturbed by the target material as in the former experiment. Therefore, the measurement of the whole proton spectrum down to the null energy is feasible.

Lifetime measurement

With event reconstruction and identification of selected hypernuclei, a fitting procedure on the secondary vertex will allow to measure the secondary vertex position and to determine the hypernuclei trajectory from the target. By taking the Lorentz boost event by

event, the distribution of the decay length of the hypernuclei grants access to the lifetime measurement.

The average decay length is extracted from a maximum likelihood fit. It uses an exponential decay distribution function convoluted with a Gaussian resolution function:

$$P(l_i, \sigma_i; l_0, \sigma_0) = \frac{1}{l_i s_0 \sigma_i \sqrt{2\pi}} \int \exp(-\frac{x}{l_0}) \exp(-\frac{(x-l_i)^2}{2 s_0^2 \sigma_i^2}) dx \tag{3.2}$$

where l_i are the measured decay length, and l_0 is the decay length of the parent. s_0 is a scaling factor on the calculated decay length errors σ_i. Those decay length errors are determined on an event by event basis from a projection of the covariant matrix of the fitted vertex along the event thrust axis. The contribution of the uncertainty in the transverse beam position is also combined inside σ_i.

The lifetime measurement is one of the most essential features of the HypHI experiments. As previously discussed, only the invariant mass reconstruction with huge background does not provide a confidence on the hypernuclear reconstruction since the analyses procedure may be complex for hypernuclear spectroscopy with heavy ion beams. Therefore, the lifetime measurement is essential to drastically increase the confidence level. Otherwise, the experimental results remain doubtful.

Production cross section

The production cross section for the produced hypernucleus can be obtained by integrating the yield of its invariant mass spectrum. For this purpose, the possible background signal has to be understood. The contribution from a background signal or from a miss-reconstruction has to be comprehended from Monte Carlo simulations of the experiment taking into account the efficiency and the resolution of each detector. Once the background contribution has been subtracted from the invariant mass spectrum of each hypernucleus, one can calculate the production cross section from the reaction rate:

$$\sigma_{prod} = \frac{N_{hyp}}{\epsilon_{trig} \cdot \epsilon_{reco} \cdot Acc \cdot BR \cdot \mathscr{L}_{beam}} \tag{3.3}$$

Where ϵ_{trig} and ϵ_{reco} correspond respectively to the efficiency of the trigger system and of the reconstruction analysis. *Acc* represents the detection acceptance of the full apparatus. The production cross section is also a function of the branching ratio, BR, of the decay channel of the studied hypernucleus. The luminosity of the beam, $\mathscr{L}_{beam}$ on the target is needed to obtain the production cross section. The luminosity is defined by the intensity of the beam N_{beam} integrated along the time of the experiment times the number of atom in the target per cm^2.

For deducing the cross section, there is a very important issue. Since the integration of the invariant mass peak of the hypernuclear signal has to be performed, the significance of the mass should be large enough. In the HypHI experiments, the minimum requirement for the mass reconstruction is that a peak of hypernuclear mass must be visible with a reasonably large significance without any background subtraction. In the invariant mass reconstruction, it often happens that the peak of the background distribution coincides with the energy of the mass peak of interest because of kinematics and other cut conditions. It sometimes leads to miss-reconstructions (fake peaks). Therefore, in the HypHI project, the analyses require the observation of a mass peak with the background distribution. In order to achieve a clear mass spectrum, it is essential to require the measurement of the secondary vertex and the lifetime, which can be achieved only by in-flight spectroscopy for the case of hypernuclei with heavy ion beams with a fixed target. By missing one of this information, the hypernuclear reconstruction remains doubtful. It should be also noted that the reconstruction of hypernuclei in the projectile rapidity region is the only way to fulfill all the requirements mentioned above, since the GiBUU calculations, as discussed in Chapter 2, do not predict the production of hypernuclei in the mid rapidity region.

3.2. Experimental principle and apparatus

During the Phase 0 experiment, a primary beam of ^{6}Li at 2.0 A GeV with an intensity of 10^7 particles per second has been impinged on a 8 g/cm^2 thick carbon target. Hypernuclei produced in the target during the collision have a velocity close to the one of the projectile, as explained in Section 3.1.1. Hence, hypernuclei decay occurs well behind the target and can be easily distinguished from the primary vertex produced by the nucleus-

nucleus reactions in the target. Tracking layers in front and behind the decay volume of hypernuclei are used for vertex reconstruction.

From the two different weak decays of hypernuclei, mesonic weak decay (MWD) and non-mesonic weak decay (NMWD), daughter particles will travel through a dipole magnet for the momentum analysis needed for the invariant mass calculation of hypernuclei. In addition to the tracking layers placed in front of the dipole magnet for the vertexing, other trackers are set up downstream from the magnet to improve the tracking. Tracking information from upstream and downstream is needed for the momentum calculation. For MWD channels, π^- particles and residues of decayed hypernuclei will be identified by their Time-of-Flight and energy deposit in different hodoscope walls mounted behind the dipole magnet.

This experimental method for hypernuclear spectroscopy by means of heavy-ion beams gives several benefits. The decay of hypernuclei will be observed in-flight in the air with this intended apparatus giving the opportunity to measure the full energy spectrum of the particles decaying from hypernuclei. Every daughters produced from the secondary decay are identified by the magnetic spectrometer, as well as particles from the primary vertex. For the first time, the particle emission after a hypernuclear decay is measured in addition to π^-. The secondary decay, which is expected to occur around 15 cm behind the target, is clearly distinguishable from the other background events coming from the primary reaction. Furthermore, the lifetime of hypernuclei can be deduced from the position of vertices after reconstruction. The Lorentz boost from the primary reaction concentrates every produced particles in a small solid angle allowing us to have an effective detection solid angle close to 4π.

Figure 3.1 shows the full experimental setup which has been placed in cave C during spring 2009. The cave C is one of the experimental hall dedicated to nuclear reaction experiments at GSI, located at the end of the heavy-ion synchrotron SIS18 and of the Fragment Separator FRS used to obtain rare isotope beams.

The setup consists of a magnetic spectrometer based on a large acceptance dipole magnet, the ALADiN (A Large Acceptance Dipole magNet) magnet [8]. The maximum bending power of the magnet is around 2.3 Tm for a 2500 A current intensity in its coil. Fragments from the heavy ion collisions are separated from each other according to their magnetic rigidity through the ALADiN magnet.

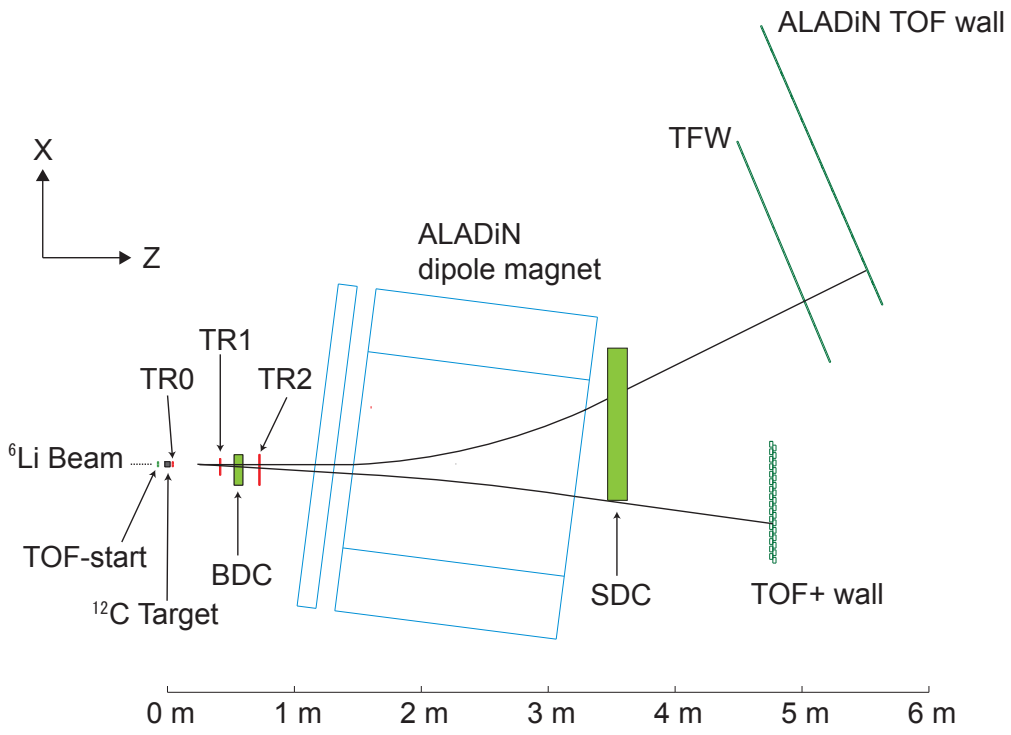

Figure 3.1.: Setup of the phase 0 experiment in cave C.

For this experiment, the magnetic field has been set to 0.75 T in order to have a fair separation between fragments by optimizing the acceptance for π^-. Positively and negatively charged particles from hypernuclei must be detected while keeping a fair acceptance for light particles behind the magnet.

The main part of the apparatus of the experimental setup is made of dedicated tracking detectors up- and downstream of the magnet (TR0, TR1, TR2, SDC, BDC). In front of the target, a small hodoscope array system is used for beam measurements and for time reference for Time-of-Flight measurements. It is referred as TOF-Start.

Three other hodoscope walls (ALADiN TOF wall, TOF+ wall and TFW) are used first as last tracking layers and as stop counters for the Time-of-Flight (TOF) measurements, providing thus particle identification. On the π^- flight path side, the two walls ALADIN TOF wall and TFW are used together to increase the tracking redundancy for the π^- detection.

In the following, the details of the detectors used in the Phase 0 experiment will be described.

3.2.1. Detection apparatus, purposes and reasons of choices

Tracking system

As shown in Figure 3.1, it has been proposed to use 4 tracking detectors, TR0, TR1, BDC, and TR2 behind the target and another drift chamber, SDC, behind the dipole magnet. The system in front of the dipole magnet is used for the determination of decay vertices of hypernuclei. The full system tracks all charged particles which are propagating in the forward direction. A multiplicity of 3 to 12 particles per reaction is expected upstream from the dipole magnet. Therefore, each tracking detector is able to handle such a multiplicity. Among those five detectors, three are four scintillating fiber detector arrays (TR0, TR1 and TR2) and two are drift chambers (SDC, BDC) with high counting rate capability, placed down- and upstream of the ALADiN magnet.

Fiber Detector:

Every scintillating fiber detector is made of SCSF-78 (Kuraray) scintillating fibers. Those fibers consist of an inner diameter core of 0.73 mm and an outer diameter cladding of 0.83 mm. They have a long attenuation length (over 4 m) with a decay constant of 2.8 ns. The layout of the fiber bundle has been chosen to align in a same row four fibers perpendicularly to the beam axis with a pitch of 0.59 mm between adjacent fibers. A schematic view of this alignment can be seen in Figure 3.2. The angle between fiber rows and the particle tracks has a direct influence on the hit multiplicity and on the viable position resolution of the bundle. To minimize the possible cross talk of the fibers and the cluster size of the particle hit detection, each row of the fiber bundle has been aligned on a grid of the readout of the Photomultiplier Tube (PMT) as shown in Figure 3.2.

The configuration of the TR0 fiber detector is slightly different because it is placed right behind the target. This configuration avoids high induced current of the high counting rate of the beam itself. Each three neighboring channels of fiber rows are connected to three different PMTs. For TR0, 1 and 2, the readout of scintillating photons is done with the Hamamatsu Photonics H7260KS MOD multi-anode photomultiplier tubes. It has a grid in the glass window in front of the photo-cathode to separate each pixel in order

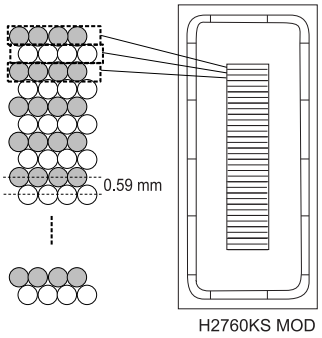

Figure 3.2.: Cross section of fiber alignment on the grid of the PMT.

to reduce cross talks. Table 3.1 summarizes the dimensions of each layer of the fiber detectors, and the number of the readout channels and PMTs. Figure 3.3 shows a picture of achieved detectors TR0, TR1 and TR2 for the vertical tracking with the connection to their PMTs.

Table 3.1.: Summary of the fiber detectors with their size, number of channels and connected PMTs.

Name	Active width (mm)	Channels	PMTs
Tr0x	39	64	3
Tr0y	39	64	3
Tr1x	139	224	7
Tr1y	76	128	4
Tr2x	245	416	13
Tr2y	113	192	6

The measured position resolution during several test experiments has been estimated to 0.21 mm in RMS (Root mean square) for ^{6}Li particles and 0.46 mm in RMS for Z=1 particles. The detection efficiency has been evaluated to 96% for ^{6}Li and 90% for Z=1 particles [77].

The TR0 layer, which is placed right behind the target, is also used to measure the energy deposit of charged particles just at the exit of the target in order to distinguish between Z=1,2 and 3 particles and to discriminate and tag background events of ${}^{4}_{\Lambda}$H and

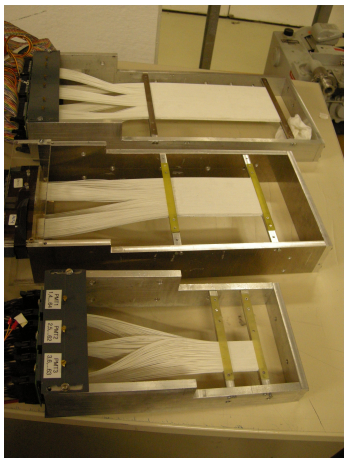

Figure 3.3.: Picture of a Y set of the fiber detectors.

${}^{3}_{\Lambda}$H hypernuclear events [77]. Details on the event reconstruction analysis will be given in Chapter 7.

The two other scintillating fiber detectors are placed between the target and the ALADiN magnet, at the distance of respectively 40 and 70 cm from the target center, as shown in Figure 3.4. Neither TR1 nor TR2 are centered on the beam axis in order to optimize the acceptance for π^- particles. The position optimization procedure will be discussed in Chapter 4.

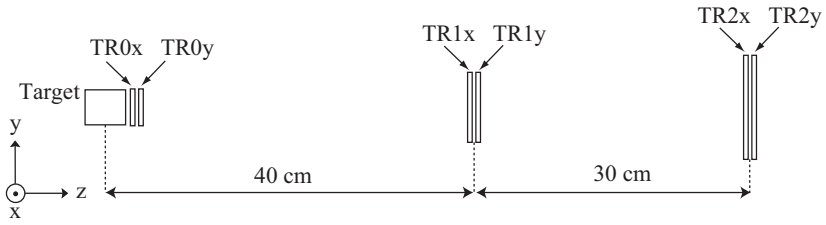

Figure 3.4.: Scheme of the Fiber detector positions.

Associated readout electronics:

A chip with 4 integrated low walk double-threshold discriminators (DTDs), the GSI-chip3, has been chosen for the front-end electronics of the fiber detectors. The main features are the small time walk and the high possible integration. The discriminator board housing 8 DTD chips has been developed for the MAMI C KaoS experiment [78]. The front-end board is connected directly to the multi-anode photomultiplier. Each discriminator board

processes 32 channels and is controlled via a VME bus. For the TR0 detector in addition, analog signals are also used for measurements of energy deposition by QDC. More details will be given in Chapter 5.

Logic signals from the discriminator board are fed to a FPGA (Field-programmable gate array) based logic module, the VUPROM2 module. This module has been developed by the HypHI group and the Experiment Electronics Department (EE) of GSI. The logic module uses a XILINX VIRTEX4 FPGA with a 400 MHz clock which gives a 2.5 ns granularity for the time measurement. Those logic signals from the full set of fiber detector are used for the secondary vertex trigger. More details about the VUPROM2 implementation will be discussed in Chapter 5.

Drift chambers:

The drift chamber, BDC (*Beam Dirft Chamber*), which is mounted between TR1 and TR2 was originally developed for the secondary meson beam lines at KEK [79] and was transfered to GSI for the HypHI Phase 0 experiment. A photograph of the BDC is shown in Figure 3.5. It consists of three pairs of wire planes, xx', uu' and vv'. The xx' pair-plane is used for the horizontal tracking, and the uu' and vv' pair-planes are placed with angles of ± 15 degrees, respectively, with respect to the wires in the xx' pair-plane in order to determine the horizontal and vertical hit positions (see Figure 3.5). The position resolution of the drift chamber is around 0.3 mm in FWHM (Full Width Half Maximum).

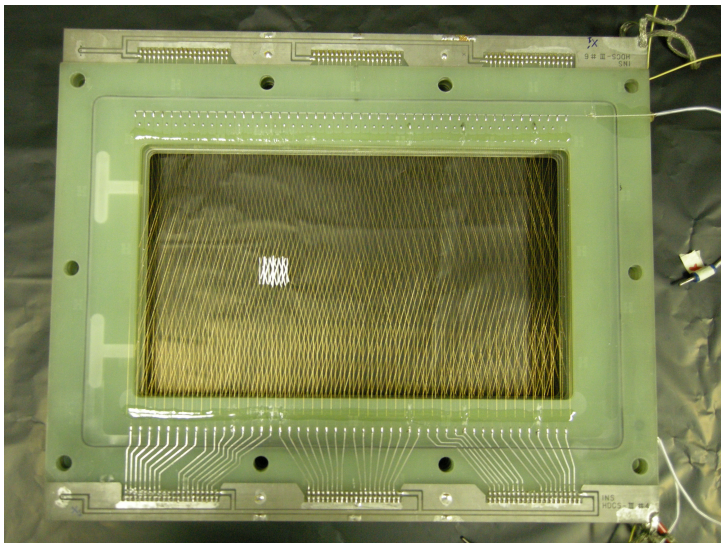

Figure 3.5.: Picture of the small drift chamber BDC.

The distance between sense wires in one single plane is 5 mm, and the corresponding single planes in the pair-plane are shifted by half of the cell size (2.5 mm) in order to resolve the left/right ambiguity around the sense wires. Between the sense wires in each single plane, there are potential wires. For the phase 0 experiment the volume in the BDC is filled with a gas mixture of Ar (70%) and CO_2 (30%).

In order to make BDC operational even though it is placed in the beam axis, a beam killer has been implemented by wrapping sense wires with Teflon sheets in all the six single planes. To wrap the sense wires, a Teflon sheet with a thickness of 0.08 mm is used and sense wires are wrapped by three turns of the Teflon sheet. The size of the beam killer is 1.5×1.5 cm^2 . For the xx' planes, 7 adjacent sense wires with a length of 1.5 cm are wrapped. For the uu' and vv' planes, 6 adjacent sense wires with different length are wrapped in order to cover the area of the beam killer. Figure 3.5 shows the area where those sense wires have been masked in all the six plane with the Teflon wrapping.

The second drift chamber, SDC (*Scattered Drift Chamber*), originated also from KEK, is used for tracking charged particles behind the dipole magnet. Figure 3.6 shows the detector placed at the rear side of the magnet. The size of the drift chamber is 120×90 cm^2. It is shifted along the x-axis by 21 cm to cover the π^- particles with a reasonable acceptance for positively charged fragments. Sense wires, which are around the trajectory of the beam, have been deactivated to avoid a high counting rate from the beam particles. The position resolution is similar to the small drift chamber's, BDC.

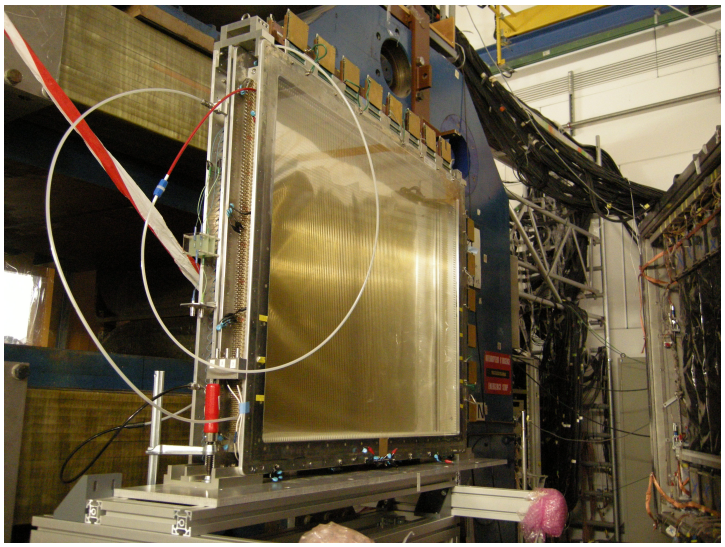

Figure 3.6.: Picture of the big drift chamber BDC behind the ALADIN magnet.

Associated readout electronics:

The readout of both drift chambers have also been shipped from KEK to GSI, and includes the preamplifier and amplifier/discriminator discussed in [79]. Signals from discriminators are fed to VUPROM2 module with a 2.5 ns time readout granularity, similar to the readout of the fiber detectors.

Particle identification system

A Time-of-Flight system is used to measure the velocity of each particle, in order to identify the particles going through the dipole magnet. This system needs a start and a stop time, provided by the TOF-Start detector and the three other Time-of-Flight walls placed behind the magnet.

TOF-Start:

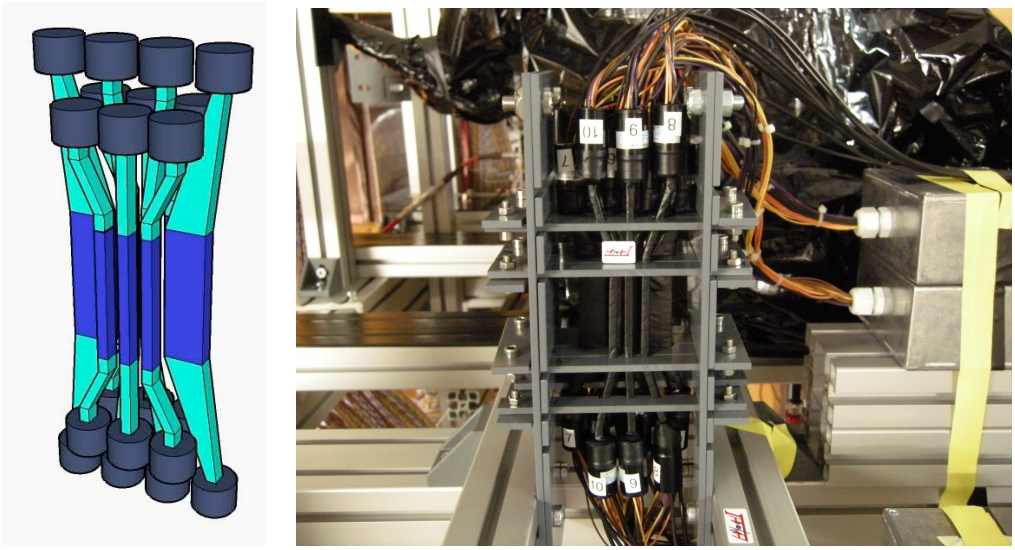

Figure 3.7.: Scheme and picture of the TOF-Start detector.

The TOF-Start detector consists of 10 plastic scintillating fingers. Figure 3.7 shows a scheme and a photograph of the TOF-Start detector. Hamamatsu R7400U-06 photomultipliers are used to read out scintillation photons from both ends of each finger. The detector is arranged in three layers with a 1 mm overlap between adjacent fingers. The width of the fingers around the beam center region is 4 mm in order to handle a high beam intensity of 10^7 particles per second over the detector. This detector has an active

area of 50 × 53 mm^2. The achieved time resolution is around 200 ps in FWHM (Full Width Half Maximum)[80].

TOF+ wall:

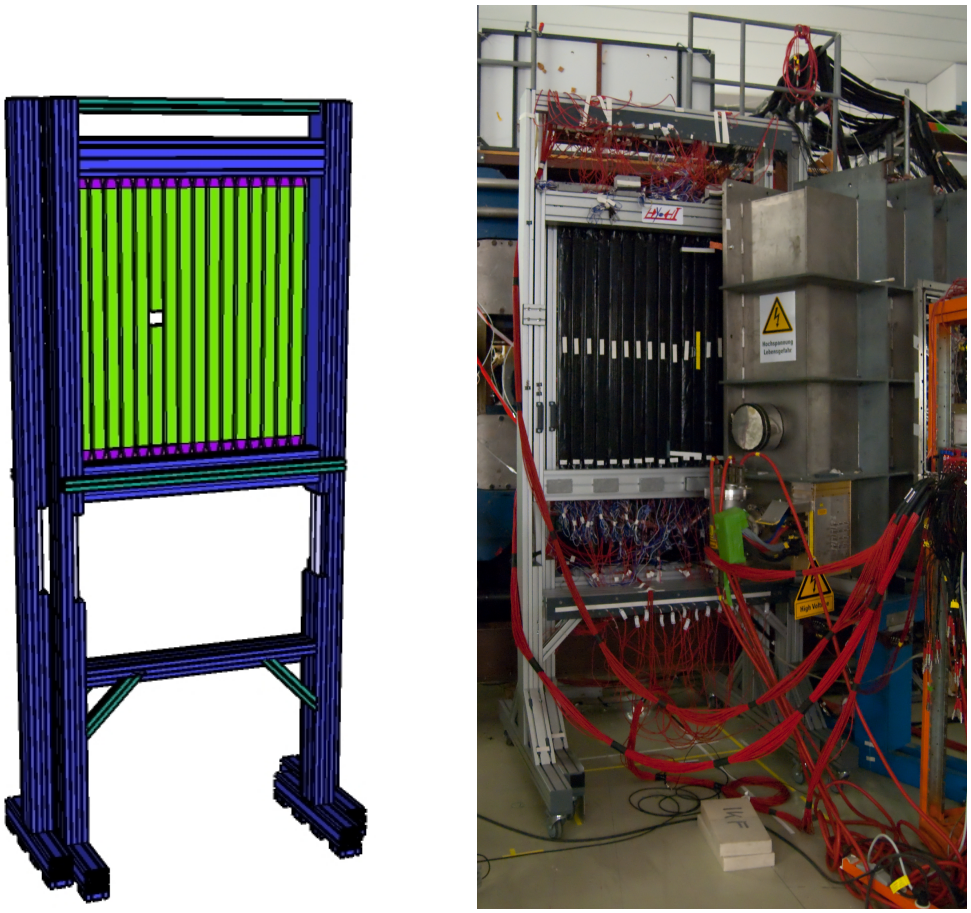

Figure 3.8.: Scheme and picture of the TOF+ wall during the phase 0 experiment.

Time-of-Flight measurements are made by fast plastic scintillator arrays: TOF-Start detector, ALADiN TOF wall, TFW and TOF+ wall. The start signal is provided by TOF-Start mounted in front of the target. For negatively charged particles up-bent in Figure 3.8, the stop signals are provided by the ALADiN TOF wall or TFW wall.

The first one has been used for the multi-fragmentation experiments [8]. The second wall has used in LAND experiments. For positively charged particles down-bent in Figure 3.1, the TOF+ wall consists of two layers of 16 plastic scintillator bars. Each bar is read out by two Hamamatsu H7415 photomultiplier tubes attached to its two end faces. The active area of the TOF+ wall is around 1 m^2. There is a hole of 7.5 × 6.5 cm^2 to allow

the passage of the beam through the detector without damaging the plastic scintillators. Figure 3.8 shows the TOF+ wall used in the phase 0 experiment. The design of the TOF+ wall will be discussed in detail in the next Chapter 4.

The front end readout electronics of the detector consists of two distinct branches, for energy and time measurements. Both information is recorded by CAEN VME QDC and TDC (time to digital converter), respectively. Details of the readout will be discussed in Chapter 5.

ALADIN TOF and TFW wall:

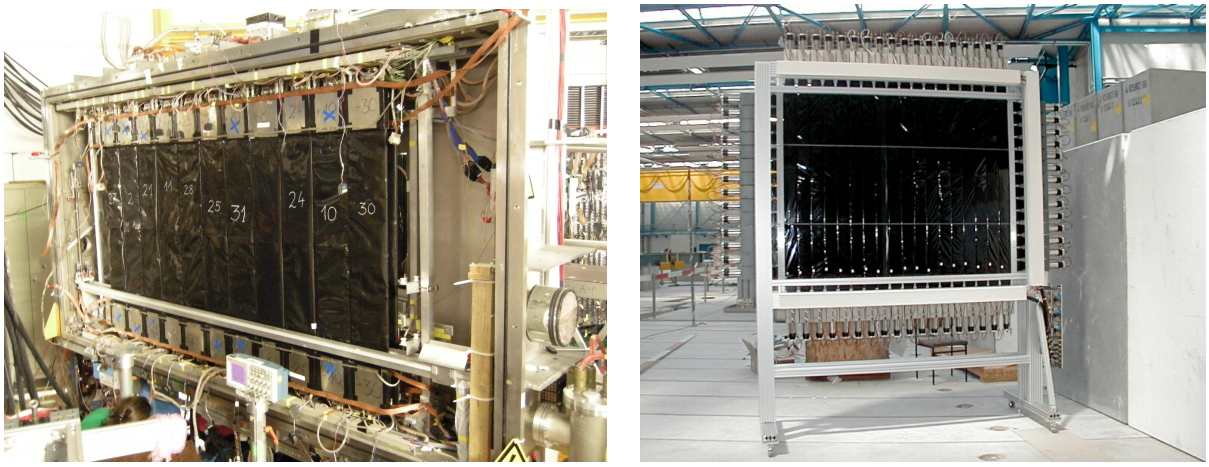

Figure 3.9.: Picture of the ALADIN TOF wall (left) and TFW (right).

The ALADiN TOF wall and TFW wall are used as stop counters for TOF measurements and tracking behind the ALADiN magnet for negatively charged particles (mainly π^- and electrons).

Figure 3.9 shows both TOF walls placed close to each other during the experiment. The ALADIN TOF wall consists of two layers of 96 plastic strips, each with a width of 2.5 cm and a thickness of 1 cm. It covers 2.4 m in the horizontal direction and 1.1 m in the vertical direction. The granularity of the position measurement is approximately 2 cm in the horizontal direction. The readout is done by HAMAMATSU photomultipliers R3478 from both sides of the plastic strips. Therefore, the total number of readout channel is 384. Energy and time information are digitized by FASTBUS ADC and TDC, respectively. A time resolution of 140 ps (RMS) has been measured for ions with $Z > 20$ from a Au+Au experiment at 600 A MeV [81]. In the Phase 0 experiment, only the first layer has been used since the other half of the detector was damaged by the previous experiments.

TFW is a 1.89 × 1.47 m^2 Time-of-Flight Wall. Its main purpose is to provide a fast trigger signal from pion detection instead of the ALADIN TOF wall which was initially considered for this task. It provides a rough position measurement with 10 cm resolution. The energy deposit of π^- is measured as well. The TFW wall consists of two planes of 18 × 14 paddles of 5 mm thickness, 10 cm wide plastic scintillators, read out at both ends with PMTs. It is also used to measure the time-of-flight and the position. Those measurements are in redundancy with the ALADIN TOF wall in case that it fails to detect the incoming particles. If ALADIN TOF wall detects successfully incoming π^- the redundancy is useful for the tracking measurement behind the dipole magnet. The granularity of the ALADIN TOF or TFW in association with the drift chamber SDC is sufficient for the invariant mass reconstruction of the hypernuclei.

Trigger system

One of the major challenges is the design of the trigger for the data taking and the reduction of the background. Three types of triggers for the data acquisition system have been used: a vertex trigger, a pion trigger and a trigger produced by the TOF+ wall for Z = 2 particles.

The vertex trigger is made of signals from the three sets of fiber detectors, TR0, 1 and 2. The logic signals from the discriminator boards are fed to the VUPROM2 logic modules. They examine if there is a secondary vertex outside the target caused by free-Λ and hypernuclear decays, and produce a trigger signal out of this inspection. The secondary vertex trigger performances have been studied based on Monte Carlo simulations. All the combinations of two x-y hit positions are considered after clustering all the neighboring hits in TR1 and TR2. The vertex trigger checks if it is possible to associate a hit on TR0 with a combination of hits between TR1 and TR2 considering a straight line. All possible straight tracks, which are coming from the primary vertex are then removed. The remaining hit multiplicity on TR1 and TR2 corresponds to an indication of secondary tracks and thus produces a vertex trigger. The decision procedure is handled with several stages of VUPROM2 logic modules. More details will be given in Chapter 5.The π^- meson coming from hypernuclear decays are detected by the two TOF wall, TFW and ALADiN TOF wall. The pion trigger requires a hit in the TFW wall above a certain energy threshold.

Another type of trigger is requested with TOF+ wall by requiring a hit with an energy-loss cut corresponding to Z = 2 particles which are the decay products of ${}^{3}_{\Lambda}$H, ${}^{4}_{\Lambda}$H and ${}^{5}_{\Lambda}$He. This trigger design, and its implementation will be discussed in Chapter 5.

Trigger efficiencies have been investigated by using Monte Carlo simulations with ${}^{4}_{\Lambda}$H and associated particles events, and full background events, produced by UrQMD calculations. The efficiency of the secondary vertex trigger has been estimated to 14% with a background reduction of 1.7%. The efficiencies of the pion and the TOF+ triggers have been evaluated to 20% and 99% with reduction of background down to 15 and 14% respectively. When all these trigger decisions are combined the efficiency is about 7% with a background reduction of 0.017%. The estimated trigger rate for the ${}^{4}_{\Lambda}$H decay channel is around 340 Hz with the combination of those three triggers. Considering the expected production cross section from other hypernuclei, such as ${}^{3}_{\Lambda}$H and ${}^{5}_{\Lambda}$He, the trigger rate is up to 2.3 kHz which fulfills the data acquisition rate.

4 Design and simulation of the Phase 0 experiment

In the previous chapter, the HypHI Phase 0 experiment has been discussed in details from the experimental setup to the trigger system. In the present chapter, the conception and the design of the experimental setup are discussed.

In the first part, the conception of a Time-of-Flight wall detector, dedicated to the detection of fragments resulted from the hypernuclear decay, is defined. The design of this specific detector has been optimized through detailed Monte Carlo simulations and the achieved design is reported. The development and test procedures have been carried out. The achieved performances during the Phase 0 experiment and the comparison with the design expectations are described.

In the second part, the detector dimensions and their positions have been optimized by using precise Monte Carlo simulations. In particular, a realistic field map of the magnetic field has been used and the resulting modifications of the apparatus are reported. This optimization procedure, which have led to the final detector configuration described in Chapter 3, is presented at the end of this chapter.

4.1. Detector design

4.1.1. GEANT4 simulations

The design of the full apparatus has been carried out by means of Monte Carlo simulations based on the GEANT4 framework [82]. Hypernuclear production and their decay

processes were implemented in the GEANT4 framework. Hypernuclear decay modes were taken from information already reported in former works, such as lifetime, branching ratio and the number of decay particles. Event-wise, physics simulations use the UrQMD or GiBUU event generators as an input for a more realistic event production than the event generator of GEANT4 for hadronic production. Several methods have been employed to describe the apparatus. A first precise design presents details of the active area of all detectors with parts of their holding structure in order to understand possible interferences. A second apparatus model is described by generic tracking detectors. Those generic trackers are assimilated to tracking planes with the closest properties to underlying detectors. This universal approach allows several fast tests before the full implementation of the detectors.

After several tests and reviews of the simulation code, the design of the detectors was defined. At the beginning of the present work, the design study of a new time-of-flight wall dedicated to positively charged particles detection, TOF+ wall, was performed.

4.1.2. TOF+ wall design

For the Phase 0 experiment of the HypHI project, detection of positively charged particles from hypernuclei decay is crucial for the vertex reconstruction and the invariant mass calculation of hypernuclei. The TOF+ wall has been designed to fulfill several requirements.

Specifications and constraints

The design of the TOF+ wall should meet several important restrictions and specifications:

1. The size of the detector has been chosen to cover, as much as possible, the profile area of the positively charged particles decaying from a hypernucleus of interest (p, ^{3}He, ^{4}He).

2. A hole through which the remaining primary beam passes is needed because of the high beam intensity of 10^7 ions per second and the maximum counting rate of 1 MHz that the PMTs can handle.

3. It is required to avoid a high multiplicity per scintillating bar to be able to ascertain the position of the particles from the decay of hypernuclei. This condition is satisfied by segmenting the wall.

4. The detector is one of the stop counters for the Time-of-Flight measurements of the experiment. A good time resolution, smaller than 200 ps, is therefore required.

5. The TOF+ wall is also used as the last tracking layer behind the magnet. A reasonably good horizontal and vertical position resolutions are thus required.

6. Signals from the TOF+ wall are used to produce a trigger signal for the data acquisition system on the detection of Z=2 particles.

Achieved design and expected performance for particle detection

The beam hole:

In the Phase 0 experiment, a ^{6}Li beam with a high intensity of 10^{7} ions per second is used. The interaction probability on the target has been evaluated to be 20%. The remained beam particles then illuminate the wall. A hole in the TOF+ wall allows the beam to pass through the detector without interaction, avoiding to create a blind-spot. The limitation of the counting rate for the PMTs is about 1 MHz, which has to be compared with the beam rate of 10 MHz. For a beam with an intensity distribution of 3D Gaussian profile with a diameter of 1 cm in width, the size of the hole has been chosen to be 6.6 cm vertically and 7.5 cm horizontally. It corresponds to more than 6 times the standard deviation, σ, of the 3D-Gaussian profile of the beam after its propagation to the wall. The bars with the hole are constituted by two separated smaller bars with a gap to create the hole. Those two smaller bars are wrapped in a reflective Mylar to keep the optical propagation of the produced light in those two scintillating bars.

Detector size:

The size of the detector is determined by the hit profile of the particles coming from the hypernuclear decay at the position of TOF+ wall. The optimal size of detection is 97.5 cm horizontally and 1 m vertically. With the optimal size which includes the inefficiency of the hole, the detection efficiency of decay fragments is as follows:

- for ^{3}He : 96.6% of the decay ${}^{3}_{\Lambda}\mathrm{H} \longrightarrow {}^{3}\mathrm{He} + \pi^{-}$

- for ^{4}He : 94.3% of the decay ${}^4_\Lambda$H $\longrightarrow$ ^{4}He + π^-
- for proton : 97.2% and ^{4}He : 93.1% of the decay ${}^5_\Lambda$He $\longrightarrow$ ^{4}He + p + π^-

Detector segmentation:

The other important issue is to avoid multiple hit per scintillating bar on the detector. It should be fair enough to create a segmentation of the detector. The direction of the segmentation has been defined to be horizontal in order to perform a fair enough position resolution in the x-direction, allowing to discriminate the space on the horizontal direction. It was chosen to compose the TOF+ wall with two overlapping layers of vertical bars. Each of those bars is 4.5 cm wide, and those two layers are overlapping by 1.5 cm. This allows a 1.5 cm position granularity in the x-direction by requiring a coincidence of the neighboring bars. To achieve the full size of the detector, the TOF+ wall is composed of 32 Bicron BC-408 scintillating bars with a length, width and thickness of 100 cm, 4.5 cm and 2.5 cm, respectively.

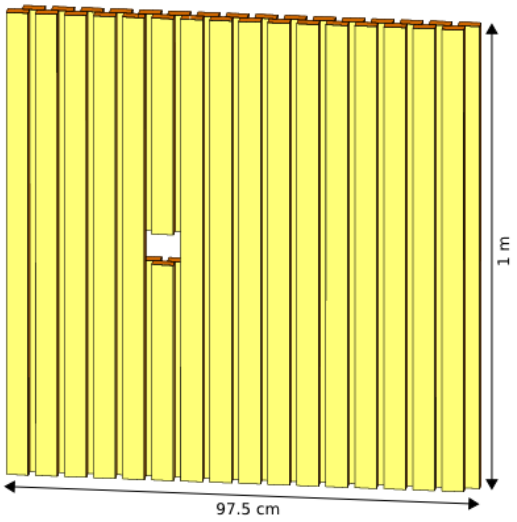

Figure 4.1.: Scheme of the TOF+ wall.

Figure 4.1 shows the full configuration of the wall. The hit density per bar obtained from the MC simulations is summarized in Table 4.1.

Counting rate:

With the designed configuration of the TOF+ wall, the counting rate on each bar can be evaluated in order to estimate if the design can fulfill the requirements in the realistic

Table 4.1.: Hit multiplicity per scintillating bar in the TOF+ wall.

1 hit	2 hits	3 hits	4 hits	5 hits
95.87%	3.77%	0.31%	0.038%	0.0053%

beam situations. A simulation has been performed with one million events including a reaction such as; 80% of ^{6}Li, corresponding to the remained beam after the reaction, and 20% of events coming from the UrQMD event generator to simulate the interaction probability in the reactions of ion collisions. Figure 4.2 shows the counting rate for each bar named by their ID number. The maximum counting rate per bar was estimated to be 362 kHz, which is observed to be two third bellow the maximum rate that can be handled by the PMT.

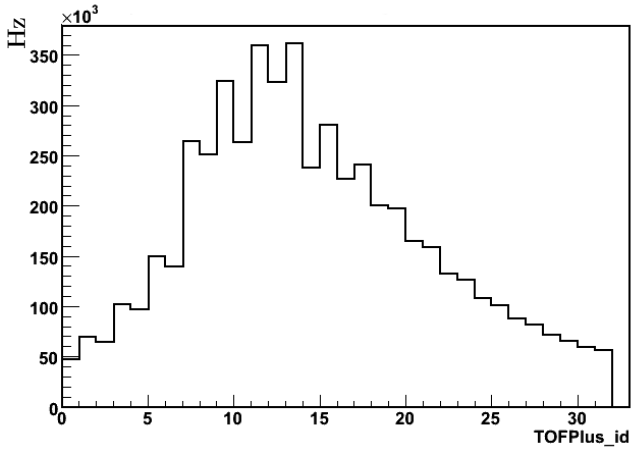

Figure 4.2.: Counting rate per bar in Hz.

Light guide design and Photomultiplier tube selection

In addition to the definition of the configuration of the TOF+ wall, there are detailed designs to be made in order to perform the realistic construction of the detector. As it has been discussed above, TOF+ is a wall of scintillator bars. Those scintillator bars should have a fast time response, a short decay time and a long attenuation length. It has been chosen to use Bicron BC-408 plastic scintillators, which are commonly used for large TOF detectors. The BC-408 plastic bars have a 2.1 ns decay time and a light attenuation

length of 210 cm. The number of scintillation photons is around 1000/MeV for Minimum Ionizing Particles (MIPs) and four times more for α-particles.

Photomultiplier tube (PMT) specifications have to fulfill the following requirements: being fast, with a high gain and small enough to fit in the layout of the wall. The decision was made to use a modified H7415 PMT from Hamamatsu, which is a 1.125 inches PMT with booster cables available and a tapered base. In the PMT, the last three dynode stages can have external voltages via the booster cable in order to stabilize the voltage in the last dynode stages at high current.

The rectangular transverse section of the bar and the circular base of the selected PMTs are different. This may introduce an efficiency loss if they were directly attached together. A light guide can be used between those two to improve their light transmission efficiency. A dedicated Monte Carlo simulation has been developed to model the geometrical optics propagation and to select the best parameters to maximize the efficiency. The geometry of the light guide used in this simulation is shown in Figure 4.3. It has been decided not to have a light guide doing the transition from a rectangular shape to a circular one to simplify the manufacture of the light guide. The shape of the light guide is a trapezoid with a square shape for the side in contact with the circular base of the PMT. The subfigure on the right side of Figure 4.3 shows the different cases in which the square side of the light guide and the circular base of the PMT can match each others: when the surface of the PMT (in red) is smaller, bigger, or an intermediate size, in comparison with the light guide surface (in blue).

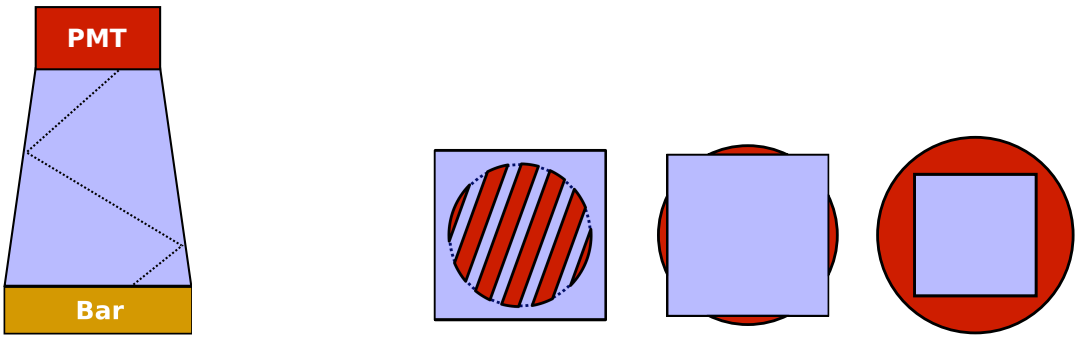

Figure 4.3.: Cross section of the light guide (in blue) and of the PMT (in red) with transversal view (left) and top view (right). The top view is represented in three cases, for which the contact area between the PMT and the light guide is different.

The efficiency of the light guide depends on its length and the cross section between the PMT and the surface of the light guide. The MC simulation was used to find what those two parameters should be in order to maximize the light transmission efficiency.

The input parameter in the MC simulation was the initial incidence angle of the light propagating in the scintillating bar before reaching the light guide. This incidence angle has to be larger than the critical angle of the total reflexion in the surface of the bar. The light guide and the surface of the bar are glued with an optical cement which avoids any optical discontinuity between the surfaces. In the MC simulation, the incidence angle follows an uniform distribution. The position of the entrance of the light was uniformly distributed on the surface of the light guide.

The first set of achieved simulations demonstrates that the transmission efficiency depends on the length of the light guide for an arbitrary surface size. For each case described in the right side of Figure 4.3, the cross section is different:

- If the base of the PMT includes all the square shape of the light guide, there is not loss of light from the cross section between those two shapes.

- If the base of the PMT is completely inside of the square surface of the light guide, the efficiency is defined as the ratio between the area of the base of the PMT and the one of the light guide: $\pi \cdot r^2/a^2$.

- If the square side of the light guide is bigger than the base of the PMT but not enough to include it, the efficiency from the cross section difference is defined by the ratio between the area of the PMT effectively in contact with the light guide and the area of the side of the light guide:

$$\mathrm{Eff} = \frac{2\mathrm{a}\sqrt{\mathrm{r}^2 - (\frac{\mathrm{a}}{2})^2} + (\pi - 4\arccos(\frac{\mathrm{a}}{2\mathrm{r}})) \cdot \mathrm{r}^2}{\mathrm{a}^2} \tag{4.1}$$

Figure 4.4 shows the dependence described above, with and without consideration of the cross section between the PMT and the light guide surface. The figure shows the importance to include the efficiency from the difference of the cross section. It is easy to evaluate what the transmittance should be between the bar and the PMT when there is no light guide (or with a really small length). In case of an 1.125 inches PMT the effective diameter of the PMT is 2.5 cm, so the transmittance is $\pi \cdot (2.5/2)^2/(2.5 \cdot 4.5) = 43.6\%$.

Only the graph including the cross section efficiency reproduces this value (the value of the small plateau at the beginning of the graph).

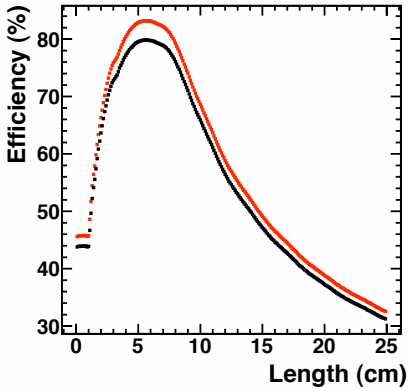

Figure 4.4.: Efficiency versus Length for a 2.05 cm × 2.05 cm square surface: in red, the efficiency without the influence of the cross section between surfaces of the PMT and the light guide. In black, the corrected efficiency including the cross section difference.

To find a correct couple of parameters for the light guide, further simulations were performed by changing the size of the side of the light guide from 1.2 cm to 2.6 cm and its length from 0 to 25 cm. By stepping the size of the light guide, the best length which maximizes the transmittance is found. The evolution is shown in Figure 4.5, which gives a maximum of efficiency for a size of the light guide of 2.05 cm × 2.05 cm.

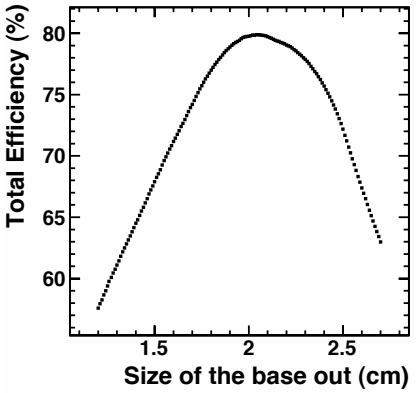

Figure 4.5.: Efficiency versus size of the base of the light guide: for each size, the maximum efficiency is calculated depending on the length.

This simple simulation deals with a 2D problem of light propagation. However, with the selected base size, the light guide will be a trapezoid. As a first estimation, it was decided to find the length which is optimal for a 2D propagation on both sides. Figure 4.6 shows that the best length is quite different in both sides. Thus, the selected length is 5 cm in order to take into account the efficiency of those two simulations.

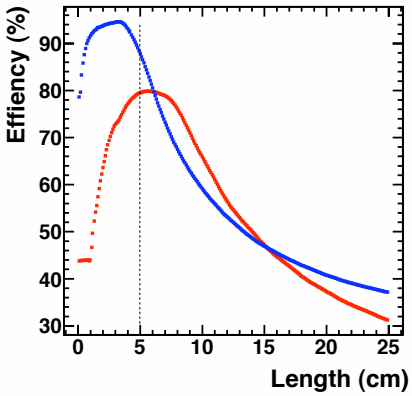

Figure 4.6.: Total efficiency considering both sides.

With the optimized light guide configuration, it is expected to have a transmittance of around 72% considering the efficiency of both sides, instead of 43.6% without a light guide.

A 3D model has been built using the geometry package of ROOT [83], in order to check the first estimations realized with only a combination of 2D models of the light guide. Monte Carlo simulations of the light propagation in the light guide have been implemented. Figure 4.7 shows the trapezoid light guide in which simulated ray traces are also represented; in blue, the ones which reach the PMT and in red the ones lost inside of the light guide.

Several Monte Carlo simulations have been carried out to achieve a good estimation of the efficiency. In total a simulation of 500 ray traces has been performed 5000 times. The resulting estimation of the light guide efficiency is 72.62% as shown in Figure 4.8. The distribution of the number of reflections in the 3D model is in average around unity. Indeed, 37.6% of the ray traces reach the PMT surface without any reflection, 49.5% of them are reaching the surface with one reflection and only 12.9% of ray traces need two reflections.

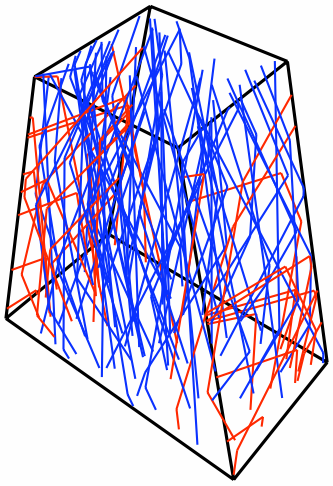

Figure 4.7.: 3D model of the light guide with simulated ray traces. In blue the ray traces of the light from the scintillator bars to the PMT base, and in red the ray traces which have been bent out of the light guide.

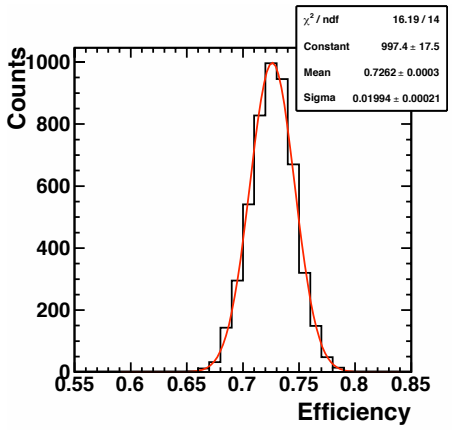

Figure 4.8.: Efficiency estimation from 5000 simulations of 500 ray traces.

Performances of TOF+ in the Phase 0 experiment

In the Phase 0 experiment in October 2009, the detector was operated in real conditions with a beam intensity of 10^7 particles per second. It was observed that the detector design is reasonably good to fulfill the requirements. A high intensity beam was handled properly by the hole. Time and energy loss measurements were fair enough to perform particle identification. The hit position profile in the horizontal (x) and vertical (y) directions also showed a reasonable particles distribution.

Time and position resolutions:

After the calibration of the TOF+ detector, the time resolution has been extracted for each scintillating bar. Figure 4.9 summarizes in the left panel the value of the calculated time resolution and in the right panel the y-position resolution for each scintillating bar. They were obtained by measuring the time difference between the adjacent bars, which were successively hit by the scattered particles. The variance of this difference represents the time resolution of the bars. The mean value of the time resolution has been evaluated around 122.2 ps in RMS (Root Mean Square). The vertical y-position resolution has been also estimated since the position is calculated as a difference of the time observed in the top and bottom PMTs. The mean value of the position resolution of the detector is 17.9 mm in RMS.

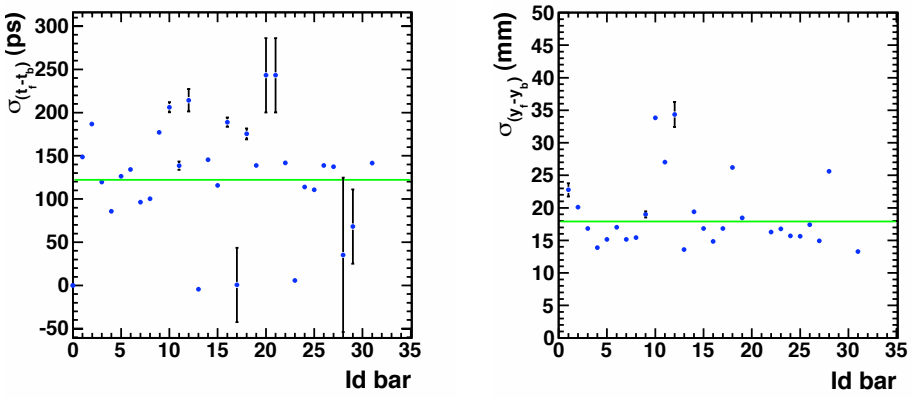

Figure 4.9.: Time resolution (left) and vertical y-position resolution (right) of each scintillator bar. The green lines correspond to the mean value of the time and y-position resolution.

Hit pattern:

By looking at the minimum bias data recorded during the experiment, which in principle correspond to a scaled down trigger by beam particles, the counting rate in the TOF+ wall was estimated in order to compare with the rate obtained by the simulations. In Figure 4.10, the counting rate is shown for different bar IDs (from 1 to 32). It has been normalized with the number of events used for this measurement. The maximum counting rate at the bar which is close to the hole region is estimated to be around 112 kHz. It is three times smaller than the estimation from the simulation.

In the right panel of Figure 4.10, the xy-position profile is plotted. In the figure, the hole is clearly visible in the profile. It shows that the detector was operational with high beam intensity, by fulfilling the requirement and constrains in the stage of the design studies.

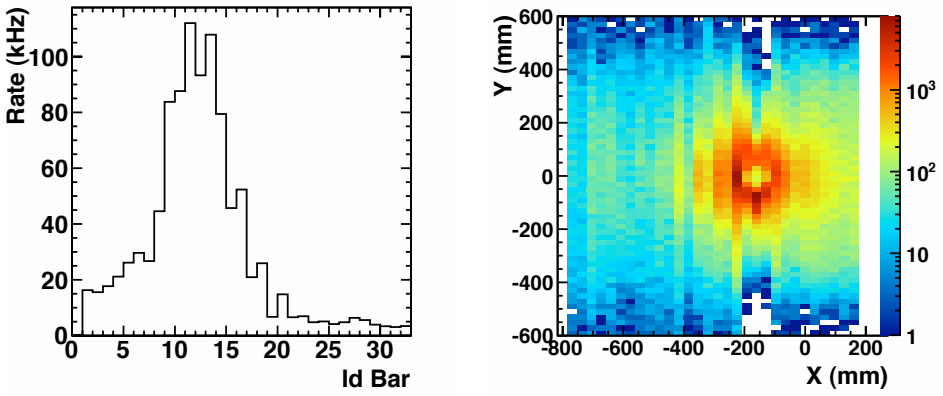

Figure 4.10.: Counting rate on the TOF+ wall normalized by the event rate (left) and the xy profile of the TOF+ wall (right).

Particle identification with measurements of the energy deposit:

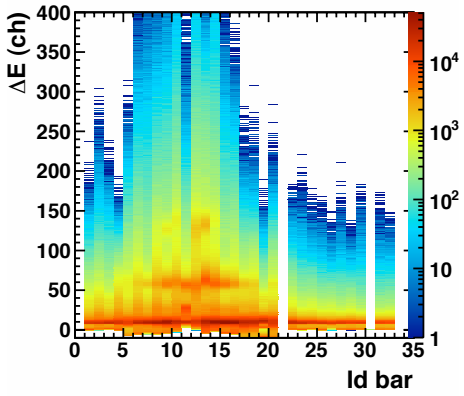

Figure 4.11.: Calibrated energy deposit in each scintillating bar. Particles of charge Z=1, Z=2 and Z=3 can be seen respectively around channels [10; 15], [55; 60] and [130; 137].

The particle identification (PID) of fragments employes the energy deposit and their reconstructed momentum. In order to make the PID being simpler, the gain of the PMT channel including the light transmission efficiency of each bar has been matched. After the gain matching, the energy deposit observed in the different bars can be compared. Figure 4.11 shows this calibrated energy deposit as a function of the ID of each bar. It is

observed that charged particles are separated for different charges: Z=1, Z=2 and Z=3. The particle identification using the reconstructed momentum will be described in the Chapter 6.

4.2. Optimization of the detector configuration

In this section, details of the optimization of the detectors used in the Phase 0 experiment will be discussed. Detailed discussion on the magnetic field of the ALADiN magnet will be also given.

4.2.1. Realistic magnetic field map

The field map of the ALADiN dipole magnet has been measured by the ALADiN collaboration. The field map was also calculated by using the program package ANSYS [84]. The result of calculation is in fair agreement with the measured field map. Thus, the MC simulations employ the calculated field map. Changes between a theoretical box-like field map and this measured one are fairly enough to be taken into account during the detector's optimization.

The realistic magnetic field is mainly carried by its y-component, and the x- and z-components are negligible. In Figure 4.12, the profile of magnetic field $By(x, z, y)$ of 0.75 T is shown in zx-, zy- and xy-plane of the laboratory frame.

In the case of the magnetic field shown in Figure 4.12, the dipole magnet does not have a clamp in the downstream region in order to increase the geometrical acceptance of detections of π^-. This leads to a small asymmetry in the tail of the field. This asymmetry is easily evinced. In the zy- and zx-plane, it can be noticed that the field only depends of the z-coordinate. The projection in xy-plane reveals that the magnetic field is fairly constant.

Indeed, Figure 4.13 represents the profile of the normalized deviation $\delta By/By$ as a function of x and y with respectively (z,y) and (z,x) free. Those figures show that the variations of magnetic field in x- or y-directions are negligible: they are less than 1%. The representation of the magnetic field can thus be simplified and be expressed only as a

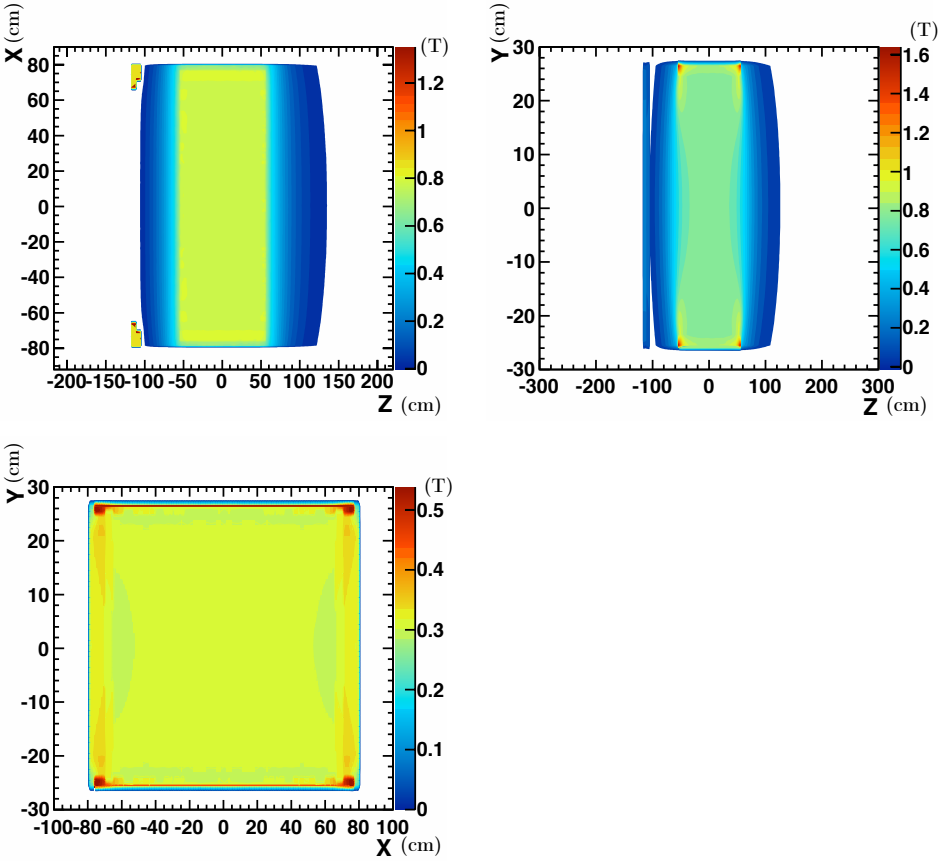

Figure 4.12.: Calculated field map of the ALADiN magnet.

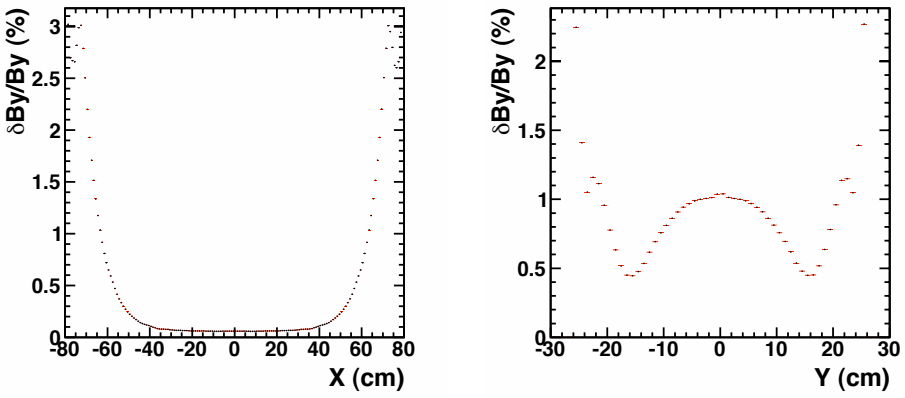

Figure 4.13.: Normalized deviation of the y-component of the realistic magnetic field.

function of the z-coordinate. This description of the magnetic field is useful for the track reconstruction analysis in Chapter 6.

4.2.2. Size of fiber detectors

The size of the fiber detectors has been optimized by studying the hit position profile of particles from the decay of Hydrogen- and Helium-hypernuclei.

As discussed in chapter 3, three arrays of fiber detectors are used for a precise tracking to obtain a good secondary vertex reconstruction. Vertices can be reconstructed only if all the particles from the decay have been measured in the different TOF walls behind the ALADiN magnet.

Particles with a low momentum are largely bent by the magnetic field and hit the cavity of the magnet. Thus, they do not go through the magnet to the detectors mounted in the downstream. It affects especially the detection of π^- meson from the mesonic weak decay. Thus, even with a large Lorentz boost, a large portion of π^- from the hypernuclear decay is not detected in the ALADiN TOF wall, which do not permit to reconstruct the hypernuclear event. It has been observed in the MC simulations that the space profile of the detected π^- behind the magnet is not symmetric in the x-direction in front of the magnet, the size and the place of scintillating fiber detectors have to be asymmetrically optimized.

The size of the fiber detectors hence covers the hit profiles of particles from the hypernuclear decay, which are detectable along the full setup. Table 4.2 summarizes sizes and positions of the arrays of fiber detectors. It shows the asymmetry in the horizontal axis of the detectors TR1 and TR2.

Table 4.2.: Summary of position and size of the fiber detectors.

Detector	Position and size (mm)				
	x		y		z
TR0	39	(-19.5 ; 19.5)	39	(-19.5 ; 19.5)	27.2
TR1	132	(-86 ; 46)	72	(-38 ; 38)	400
TR2	245	(-165 ; 80)	113	(-56.5 ; 56.5)	700

The number of the scintillating fibers per channel was also investigated via MC simulations and the test measurements with cosmic-rays. In the initial design, arrays with two fibers per channel was considered in order to minimize the thickness of the material. However,

it has been pointed out during detector tests that two layers of fibers do not provide enough photons to the PMT channel for energy measurements. The chosen solution was to increase the number of layers to four.

The influence of this modification has been investigated to estimate the deterioration in the position resolution, and especially the secondary vertex resolution during the hypernuclear event reconstruction in MC simulations. Figures 4.14 illustrate the influence of 4 layers instead of 2 layers in the fiber detectors, and Table 4.3 summarizes all secondary vertex resolutions between those 2 different designs. It was observed that the difference is caused by the particle multiple scattering effect which is larger in the case of thicker detectors.

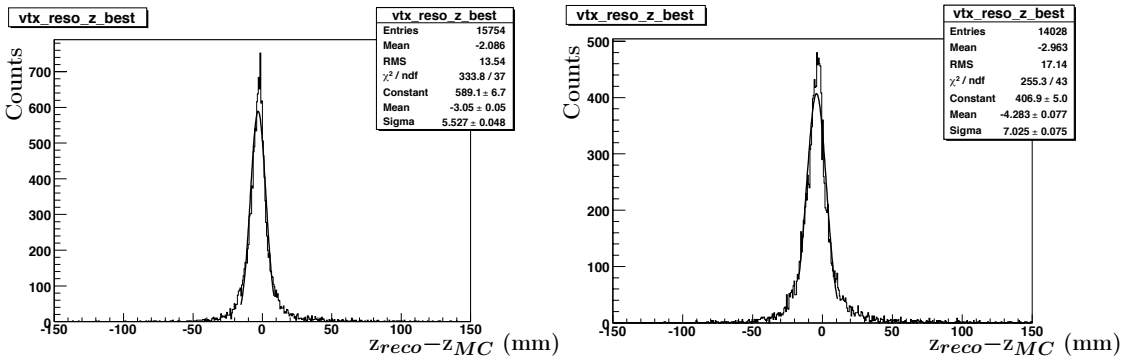

Figure 4.14.: Longitudinal vertex resolution in the 2 layer case (left) and 4 layer case (right).

Table 4.3.: Change in vertex resolutions between 2 and 4 layers in the design of the fiber detectors.

	x (mm)	y (mm)	z (mm)
2 layers	0.287	0.371	5.527
4 layers	0.416	0.524	7.025

4.2.3. Optimization for detector positions

The position of the full apparatus had several revisions during the development of this work. The first optimization was based on the proposal of the experiment. Before the installation of all the detectors in the experimental area, several adjustments were needed for the final optimization.

Intermediate design

After the first set of full simulations, the position of the detectors was optimized. The use of a more realistic field map slightly changed the optimal positions, enough to be considered. Especially the positions of TOF walls were modified because of a different π^- hit profile and position of the hole. Table 4.4 summarizes the geometry of the setup in the intermediate design.

Table 4.4.: Size and position of each detector in the intermediate design.

Detector	size and position (mm)				
	x		y		z
TR0	39	(-19.5 ; 19.5)	39	(-19.5 ; 19.5)	27.2
TR1	132	(-86 ; 46)	72	(-38 ; 38)	400
BDC	240	(-165 ; 75)	150	(-75 ; 75)	550
TR2	245	(-165 ; 80)	113	(-56.5 ; 56.5)	700
SDC	1200	(390 ; 810)	900	(-450 ; 450)	3400
ALADIN TOF	2300	(2740 ; 440)	1000	(-500 ; 500)	5500
TOF+	725	(-842 ; 117)	1000	(-500 ; 500)	5500

In this configuration the geometrical acceptance of the full apparatus has been evaluated. First the rejection of the beam by the hole is estimated to allow only 0.55% of the beam on the detector. The detection of all isotopes of hydrogen ions is meanly around 97% in all hypernuclear decay cases or from the primary reactions. The detection acceptance for He fragments is different between the hypernuclear decays considered, as shown in Section 4.1.2. The maximum detection efficiency of π^- on the ALADiN TOF wall is about 19% to 21% in the best case for the hypernuclear decay. This low geometrical efficiency is due to the ALADiN dipole magnet. At 0.7 T, only 20% of detectable pions are found behind the magnet.

Final design

While the installation of the setup in the experimental area, it has been found out that several positions were not fitting in experimental area. Therefore, the position of the detectors was optimized again according to the real situation of the experimental hall. It

turns that the ALADiN TOF wall has to be placed closer to the magnet than the one in the initial design. However, this configuration reveals the interaction of the massive holding structure of the ALADiN TOF wall interacts with the beam trajectory. In order to avoid the interaction, the ALADiN TOF wall has been shifted farther away from the beam axis, and it has been proposed to increase the strength of the magnetic field. The position of the ALADiN magnet and the strength of the magnetic field was re-optimized with MC simulations by studying the π^- acceptance in cases of the decay of ${}^{3}_{\Lambda}\mathrm{H}$, ${}^{4}_{\Lambda}\mathrm{H}$ and ${}^{5}_{\Lambda}\mathrm{He}$, as shown in Figure 4.15.

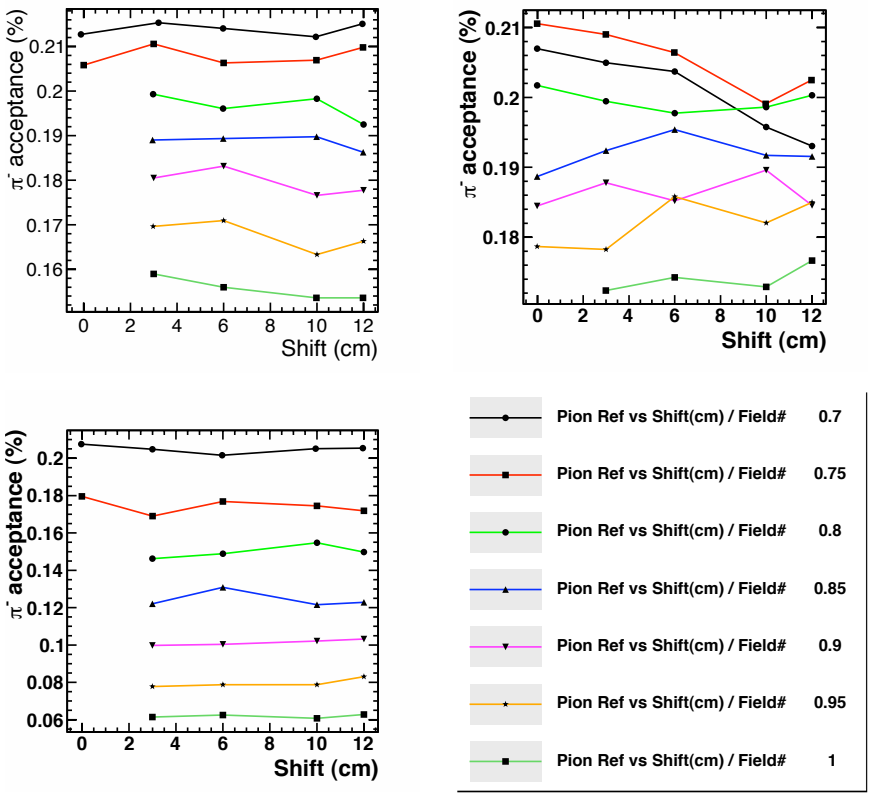

Figure 4.15.: π^- acceptance as a function of the x-position shift of the ALADiN TOF wall and of the strength of the magnetic field in case of ${}^{3}_{\Lambda}\mathrm{H}$ (top left), ${}^{4}_{\Lambda}\mathrm{H}$ (top right) and ${}^{5}_{\Lambda}\mathrm{He}$ (bottom left).

A portion of the beams interacting with the holding structure of the ALADiN TOF wall has also been investigated as a function of the amount of the shift of the ALADiN TOF wall, as shown in Figure 4.16. With those investigations, the final optimal position of the ALADiN TOF wall and the optimal field strength of the ALADiN magnet has been chosen respectively as 6 cm in x-direction and 0.75 T instead of 0.7 T. With the revised

optimal values, the only drawback which appeared was a much lower π^- acceptance in the case of ${}^{5}_{\Lambda}$He.

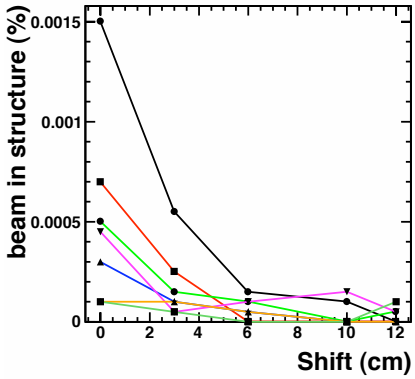

Figure 4.16.: Beam proportion in the holding structure of the ALADiN TOF wall. The color code is the same as in Figure 4.15.

The reduction of π^- acceptance in cases of ${}^{3}_{\Lambda}$H and ${}^{5}_{\Lambda}$He with the rise of the magnetic field strength is due to the kinematics of the mesonic weak decay of those hypernuclei. By increasing the strength of the magnetic field, the difference between angles of pion deflection of each kind of hypernucleus is enhanced. Figure 4.17 shows the momenta of π^- mesons as a function of the polar angle for decays of ${}^{3}_{\Lambda}$H (top left), ${}^{4}_{\Lambda}$H (top right) and ${}^{5}_{\Lambda}$He (bottom left). Pions from ${}^{4}_{\Lambda}$H decay are generally produced with a higher momentum than in other cases, which indicates that those pions have a smaller deflection angle after passing through the magnetic field than the two other decay cases.

Thus, the hit profile of each hypernucleus case is different on the ALADiN TOF wall. While pions from ${}^{4}_{\Lambda}$H are within the region closer to the beam on the detector, due to their smaller deflection, pions from ${}^{3}_{\Lambda}$H are located roughly in the middle of the detector. On the other hand, pions produced from ${}^{5}_{\Lambda}$He decay are on the opposite side of the case of ${}^{4}_{\Lambda}$H. This tendency is clearly shown in Figure 4.17.

By increasing the strength of the magnetic field, the hit profiles of pions from those three hypernuclei decay become wider. While the pion acceptance for the case of ${}^{4}_{\Lambda}$H is extended to the middle of the ALADiN TOF wall and thus increases, the acceptance for the cases of ${}^{3}_{\Lambda}$H and ${}^{5}_{\Lambda}$He become less. For a magnet field of 0.75 T, the ALADiN TOF wall should be 50 cm wider to be able to keep the similar acceptance for the three hypernuclear cases.

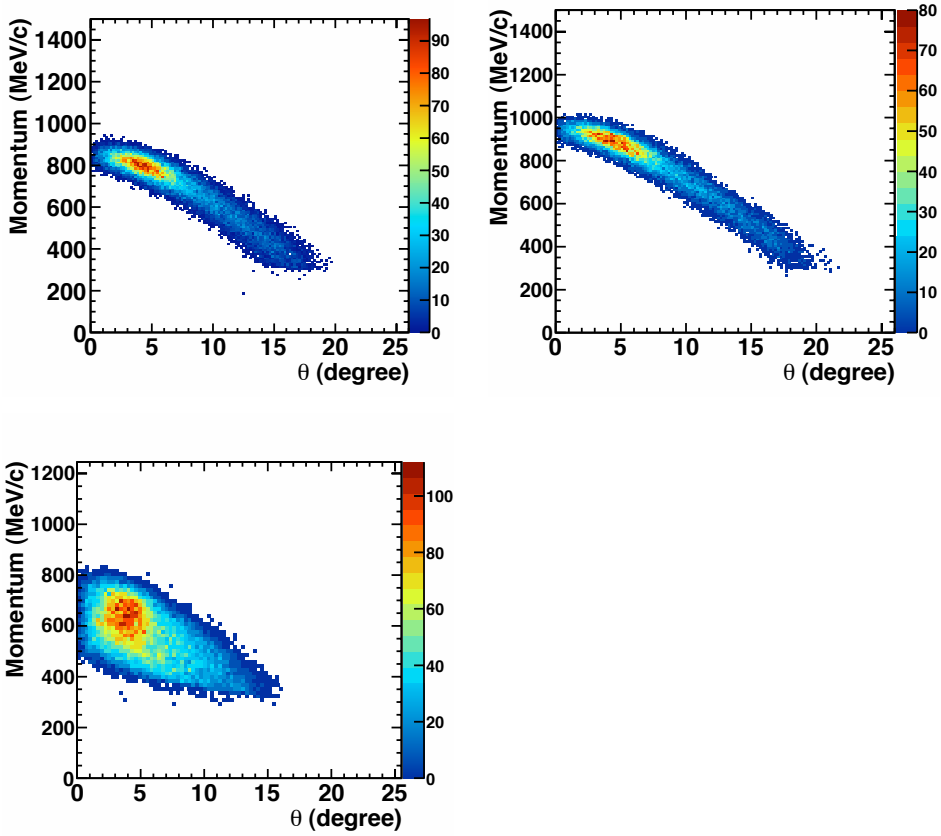

Figure 4.17.: Correlation of the momentum against the polar angle θ of π^- produced by the hypernucleus decay of ${}^{3}_{\Lambda}\mathrm{H}$ (top left), ${}^{4}_{\Lambda}\mathrm{H}$ (top right) and ${}^{5}_{\Lambda}\mathrm{He}$ (bottom left).

Therefore it has been concluded to rotate the ALADiN TOF wall instead of keeping the detector perpendicular to the beam axis. Another set of studies with MC simulations have been performed in order to optimize the angle of the ALADiN magnet, and the results of the study are summarized in Figure 4.18.

The left panel of Figure 4.18 shows the pion acceptance in case of ${}^{3}_{\Lambda}\mathrm{H}$, ${}^{4}_{\Lambda}\mathrm{H}$ and ${}^{5}_{\Lambda}\mathrm{He}$. The right panel shows the beam proportion on the holding structure, as a function of the angle used to rotate the ALADiN TOF wall from the perpendicular angle of the beam axis. The improvement of the pion acceptance is shown in the left panel of Figure 4.18. Before selecting the angle, it may be noticed that the acceptance increases with the rotation angle. While increasing the rotation angle, the obtained position resolution via hit clustering becomes poorer because incident particles would pass through more section of the scintillating bars. However, the possibility to recover the pion acceptance from the

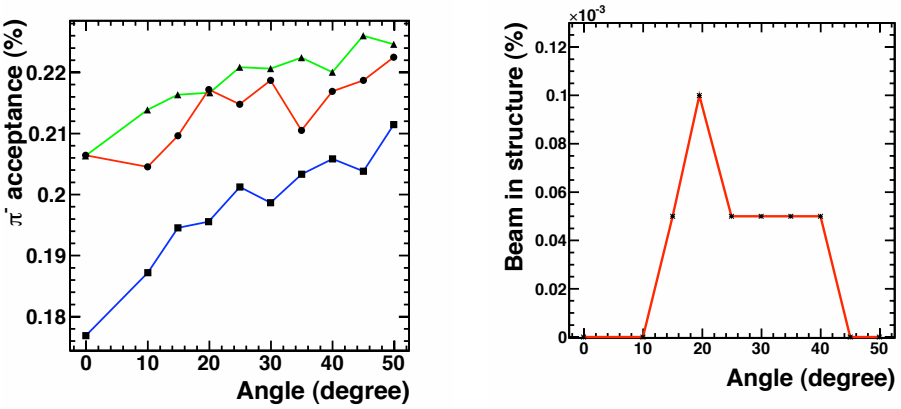

Figure 4.18.: Left panel: π^- acceptance as a function of the rotation angle of the ALADiN TOF wall in case of ${}^{3}_{\Lambda}$H (green triangle), ${}^{4}_{\Lambda}$H (red circle) and ${}^{5}_{\Lambda}$He (blue square). Right panel: beam proportion on the holding structure of the ALADiN TOF wall as a function of its rotation angle.

${}^{5}_{\Lambda}$He decay is a good perspective to consider. After all those considerations, it was decided to place the ALADiN TOF wall with an angle of 20 ° respect to the beam axis, after a shift of 6 cm in the x-direction from the initial orientation.

Summary of the new setup

The ALADiN TOF wall was placed with a 6 cm shift and with an angle of 20 ° in respects of the beam axis. In addition, the TFW wall was placed in front of it with the similar rotation and shift. Figure 3.1 of Chapter 3 which shows the setup layout represents the final configuration of the setup. The positions of the two TOF walls, the ALADiN TOF wall and the TFW, have been measured by the laser devices, and the angle of the two TOF walls were found to be respectively 23.8 ° and 22.8 °.

The position of TOF+ wall has been decided by the position of the hole in which the beam has to pass through. It has been placed in front of the holding structure of the two other TOF walls at 4.8 m from the target as shown in Figure 3.1. The inefficiency introduced by the hole is increased because of the Gaussian hit profile of helium fragments which is close to the hole. The modified geometry leads to an inefficiency of 2% in the detection of the helium fragments.

5

Design and development of the data acquisition and trigger system

One of the challenges of the Phase 0 experiment is to deal with the cross section difference of seven orders of magnitude between the total reaction cross section and the hypernuclear production cross section. It has been proposed to use an online selection via the trigger system in order to reject the background signal. The trigger system is a crucial aspect to handle the challenge of the Phase 0 experiment.

The current chapter focuses on the design and the development of the trigger system of the Phase 0 experiment and on the data acquisition system, which is strongly related to the trigger decision. First of all, the electronics system is described and a special attention on a newly developed logic module is drawn. Implemented features in the data acquisition system and the trigger decision strategy are summarized as well. The concept and design of the three parts, in which the trigger system consists of, are specified. Their development and full implementation are then presented. The implementation results obtained from several test procedures are reported. The performances of each trigger subsystem during the Phase 0 experiment are then presented and discussed. The achievement of full trigger system used during the experiment concludes the present chapter.

5.1. Data acquisition

The data acquisition system (DAQ) is in charge of the readout of the detector signals, hardware- and software-wise, and of the data transfer to a data storage center. In the

Phase 0 experiment, electronics provides a massive amount of channels to read out: more than a few thousands. The data acquisition system has to be able to handle the huge amount of channels with low latency. Several methods of hardware readout including electronics devices have been developed, especially the trigger module VUPROM 2, a newly developed VME logic module designed in collaboration between the HypHI group and the EE electronics group of GSI.

5.1.1. Electronics systems

For the Phase 0 experiment, different branches of electronics have been used according to the requirement of the detector readouts. Time-of-Flight detectors give both energy deposit and time information needed for the particle identification and position measurements, while only the time information from sets of fiber detectors and drift chambers is relevant. However, there are a few exceptions since the TR0 layer of the fiber detectors as well as the active target have been used to measure also the energy deposit of particles. In the case of TOF detectors, the TOF-Start detector requires the use of an amplifier in order to provide a clearer signal. Figure 5.1 summarizes those two different electronics chains with those exceptions. The top panel presents the TOF detectors branches and the bottom panel the fiber and drift chamber detectors.

Signals provided by the detectors have to be split to allow the measurements of time and energy deposit. The measurement of energy deposit is achieved by using analog signals fed to QDC modules, a charge-to-digital converter, integrating and measuring the charge of the signals within a time gate. Those signals have to be delayed to be synchronized with the trigger system decision.

On the other hand, the time measurement is based on logic signals obtained by discrimination of the analog output of the detectors. Different kinds of discriminators are used in the full electronic system to fulfill different purposes. It has been decided to measure leading and trailing edge of the signals from the fiber detectors in order to determine their pulse width. With those two pieces of information, the pulse width gives a correlated information about the energy deposit. This feature is provided by a specific discriminator with the double-threshold technique, as described in Chapter 3. Moreover, logic signals from the TOF+ wall are used in the trigger system to select Z=2 particles. Those signals are provided by another type of discriminator, described in the dedicated Section 5.2.1.

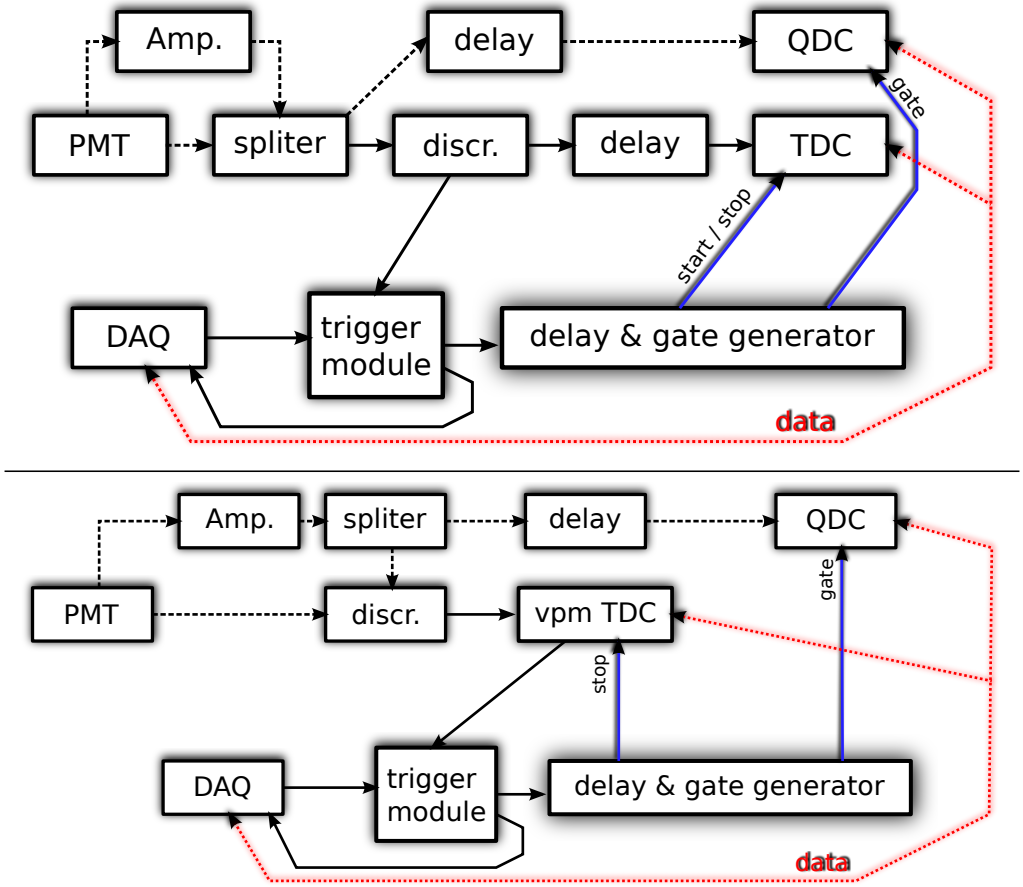

Figure 5.1.: Scheme of the electronics chain for one channel and its interplay with the trigger system and the data acquisition. Each panel corresponds to a different detector branch : in the case of signals from a Time-of-Flight detectors (top) or from Fiber & Drift chamber detectors (bottom).

The time measurements after the discriminator are treated by a TDC module (a Time-to-Digital Converter). These modules measure the time difference between the incoming signal and a common start or common stop signal, depending on the configuration of the TDC modules.

A unique electronics module, labeled as *vmp TDC* in Figure 5.1, has been used in the electronic setup. It is a dedicated TDC module based on a logic module on-boarding a *FPGA* (Field-Programmable Gate Array) chip which can be used for several purposes since it is programmable.

In the Phase 0 experiment, 46 modules have been used for time measurements of fiber and drift chamber detectors as well as for the trigger system. Those modules were developed

for the HypHI project in collaboration with the EE electronics group of GSI. They are called VUPROM2 (VME Universal PROcessing Module).

The data acquisition system follows the decision of the trigger system requesting the readout of digital acquisition modules, and it accepts the trigger signal if it is not busy from a previous event readout. Gates for the QDC modules, as well as common start and stop signals for the TDC modules are generated from the accepted trigger.

Those generated gates are sent to each digital acquisition module to inform it to proceed with the digitization of the incoming signals. It is important to synchronize the incoming signals to the readout modules with the signals from the trigger system in order to generate gates signals or other signals needed for the QDC and TDC modules with the proper timing.

5.1.2. VUPROM2 module

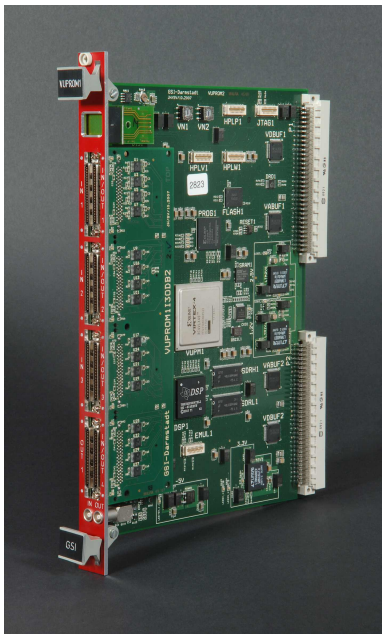

Figure 5.2.: Picture of the VUPROM2 module.

The VUPROM2 module, mentioned above, is a logic module which includes a FPGA chip, an electronic component used to build reconfigurable digital circuits. This particular module consists of 256 I/O channels, a *DSP* (Digital Signal Processor) and the FPGA chip which can be operated at 1 GHz and 400 MHz respectively and can be controlled by

a VME bus. One of the main features is the high channel density which allows to handle a large number of channels of the fiber and drift chamber detectors. These modules can easily be cascaded to each others thanks to highly dense *VHDC* (Very High Density Cable Interconnect) cables, which are extremely functional for the design and the implementation of the trigger system. The FPGA chip is the most essential part. It allows to program any logical operations and can be used for multiple tasks. The programming language used is the *VHDL* language (VHSIC Hardware Description Language; VHSIC: very-high-speed integrated circuit).

The VUPROM2 module is used in the Phase 0 experiments for several purposes. First, it has been programmed as a TDC module for the time measurement of the fiber detectors and drift chambers. This implementation has been cross checked during test experiments by comparing the time measurements achieved by a well known standard TDC module and by the VUPROM2.

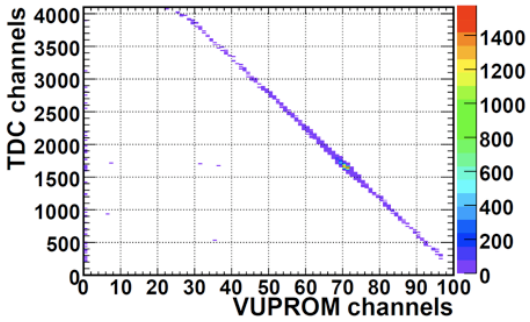

Figure 5.3.: Correlation between time measurements done by standard TDC module and the TDC implementation of VUPROM2.

The correlation is shown in Figure 5.3. The reason of the negative correlation is that the VUPROM TDC has been implemented in common stop mode, whereas the standard TDC module was used in common start mode. The VUPROM2 TDC runs with a clock at 400 MHz giving a 2.5 ns granularity for the time measurement with a full range of 500 ns, which can be configured by users. The implementation used for the time measurement of the fiber detectors has also another feature to measure leading and trailing edge needed for the pulse width measurement. For the drift chambers, the implementation includes a double-hit TDC. For a same channel, the module can record double time measurements by event from two consecutive pulses in the layer of the drift chambers.

The second use of this specific module was to build a full trigger system of electronics readout. As discussed in Chapter 3, the trigger system is composed by four stages with

different implementations: channel scattering, coincidence tensor algorithm, pulse width selection and full decision. Details will be discussed later on, in their own dedicated sections of this chapter.

The VUPROM2 modules are also used to manage a large number of scalers, used to count how often a detector channel or an intermediate signal is fired. For example, this allows to judge the rate of trigger decisions which have been accepted by the data acquisition system over the total number of trigger decisions. The scaler information is used to estimate the dead time of the DAQ, which is the period of time during which the DAQ is busy with the current event readout.

5.1.3. Features implemented in the DAQ system

The data acquisition system runs with the Multi Branch System (MBS), the DAQ framework developed at GSI [85]. This framework helps users to focus only on the readout procedure between the DAQ and the digital acquisition modules, like TDC or QDC modules. All other issues are arranged by MBS. It handles the readout processing, and it controls the data taking processors with synchronization of all those multi-branch processors by interconnected trigger modules. It also operates all the data transfers and the data writing between processor buffers and data storage units.

The MBS system provides and handles trigger type mechanisms to allow users to read functions out to react and proceed differently as a function of the type of the accepted trigger. In the Phase 0 experiment, the DAQ includes a data size reduction procedure based on a zero-suppression method. To avoid processing all the ten-thousand-possible channels, digitization modules and the data acquisition system can read out only fired channels. Thus, the DAQ can speed up the readout and data transport over the network by associating indexes and values of the non-zero channels, instead of keeping the channel order and the full readout.

In the case of time measurements by TDC modules, the zero suppression is easily accomplished because signals are logic. If there is no input, there is no time difference measurement from the common reference signal. Thus, inside TDC modules, channels with zero time difference are simply ignored.

In the case of charge measurements by QDC modules, this method is not called zero suppression but pedestal rejection: a value lower than a certain threshold value is not considered to be read out.

Analog signals for charge measurements have a baseline (or zero noise level) usually called pedestal. The pedestal signal does not carry any information since it comes from the baseline which shifts with the noises. Therefore, the corresponding baseline value has to be subtracted in order to perform a proper charge integration. The key of the pedestal rejection is to define the proper value for this threshold. Since the result of the measurement of the baseline distribution gives, after a certain time, a Gaussian distribution, it is easy to obtain the mean value μ_{ped} and the standard deviation σ_{ped} of the pedestal distribution. By assuming a threshold at $\mu_{ped} + 3 \cdot \sigma_{ped}$, only 0.1% of the pedestal signal is exceeding this limit. To determine this threshold value for each channel, the DAQ readout is set to measure every channels without the pedestal rejection every 10 thousand events, and if this threshold has moved, a new value is updated. During the experiment, it has been ensured that those threshold values do not move significantly.

With those methods in every digital acquisition modules, the data size of each event was minimized.

5.1.4. Trigger decision

The trigger system notifies the decision of data taking to the DAQ system. Different trigger decisions can be set and used with the MBS framework. For example, in the Phase 0 experiment, two specific trigger types were used; one to indicate physics events and another for the no-physics-meaning pedestal measurements. More refinement has been included for the physics trigger type. The trigger system is based on a cascaded VUPROM2 module architecture, allowing to record inside of the event structure the physics pattern used for the decision. For the Phase 0 experiment, a physics trigger decision corresponds to 4 different physics events: two patterns for hypernuclei decay (two or three body decay), the third one records the minimum bias event, which requires only a hit in the TOF-start detector and at least one hit on any fiber detector, and a last one for the data taking with the primary reaction in the target. Those last two patterns have been scaled down by a factor of 65536, (2^{16}), by comparing the frequency of the minimum biased events and the primary reactions in the target with the one of

the hypernuclear events in order not to conceal hypernuclei events that are the most important for the experiment.

Trigger decisions for the physics events will be discussed later in this chapter, especially for the hypernuclei trigger for which important developments were needed.

5.2. Design and development of the trigger system

In order to optimally operate the data acquisition on the physics interests of the Phase 0 experiment, a trigger system was needed for hypernuclear event selection. This trigger system has been designed to pick hypernuclei events out of the huge reaction background events.

The development and implementation of the full trigger system was one of the most essential part for the HypHI project. As discussed in Chapter 3, the trigger system is composed of three separated parts: one from the fiber detectors to compute a secondary vertex tagging, one from the TOF+ wall for charged particle tagging and the last one from the ALADiN TOF wall for the π^- hit requirement. All of them were computed in parallel. The final decision of triggering on a possible hypernucleus event is done by requesting the presence of all the three tags.

5.2.1. TOF+ trigger stage

The main goal of the TOF+ trigger stage is to be able to discriminate positively charged particles by means of time-over-threshold measurements.

Trigger signals in this stage must not depend on the hit position in the TOF+ wall to provide tags within fixed time. This behavior is essential for the trigger system to allow the master trigger module to take the final decision within a small interval of time.

The trigger decision is required to measure in real time the pulse width of the signal coming after the meantimer module, an electronic module which will be discussed in the following section. It will be shown that the pulse width is correlated with the deposited energy in the scintillator bar, thus to the charge of the particle. The trigger for Z=2 particles on the TOF+ wall is sent to the master trigger system by requesting a specific minimum pulse width.

Time over threshold: Principle and Methods

Two signals from a scintillating bar of the TOF+ wall are fed to a leading edge discriminator (LED) with pulse width dependency. Once a signal amplitude exceeds the fixed threshold value the LED generates a corresponding logic signal which ends when the analog input signal amplitude crosses again the threshold after reaching its maximum (it has to be noticed that signal amplitudes are all negative). Figure 5.4 shows three different signals from different particles recorded during a test experiment with a digital oscilloscope. If the threshold of the discriminator is set to -0.1 mV, the resulting logic pulse has different pulse widths for different signal amplitudes as illustrated in Figure 5.4. With this specific discriminator, it is possible to keep in a certain order the correlation between the charge via signals from energy deposit and the logic pulse after discrimination. This correlation is not precise, but good enough to take decisions via the dedicated trigger subsystem.

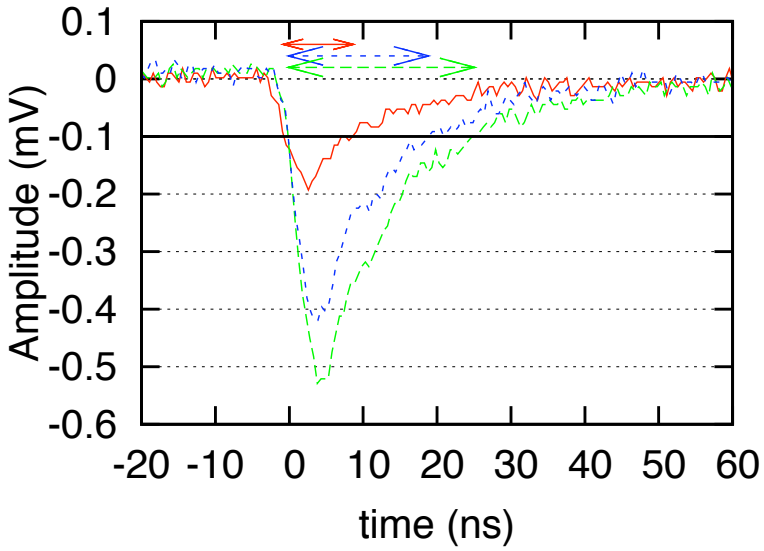

Figure 5.4.: Time over Threshold measurements. Each curve corresponds to the amplitude signal of a different particle passing through a scintillating bar. For each curve, an arrow represents the pulse width over the threshold of -0.1 mV (black horizontal line). Those signals have been recorded via digital oscilloscope.

The TOF+ bars are 1m long and have 2 PMTs at both ends, top and bottom, as described in Chapter 4. Signals from the same scintillating bar cannot be taken individually because of the light dispersion inside of the considered bar, which would produce different timing. The amplitude of signals induced by the two PMTs of the same bar is thus different

enough to exhibit a difference in pulse width. This difference induces a difficulty to discriminate the charge of the particle on the trigger level. It is then necessary to combine the information from signals from the two PMTs to remove position dependency of the arrival time and pulse amplitude.

One of the common methods to overcome the position dependency (i.e. the light dispersion) of the analog signal's amplitude in the trigger level is to use a *mean-timer* module. The principle of the circuit algorithm is to introduce a delay chain on board to compensate the difference of the propagation inside the scintillating bar and to have at the end a common logic signal resulting from the coincidence between the two incoming analog signals. Figure 5.5 shows a diagram of this principle and the time propagation of signals in the vertical y-axis. From a hit in the scintillating bar, photons propagate inside the bar with the speed of light in the plastic bar. They reach both PMTs, which is represented when arrows reach both y-axis in the figure. Produced analog signals propagate to the same electronic circuit and reach this delay chain, corresponding to the second arrow starting from the intersection with the first arrow and the y-axis. If the delay line is long enough, a new coincidence point can be reached as shown in Figure 5.5. If different signals coming from a different position in the scintillating bar are considered, it can be demonstrated that the coincidence point is the same:

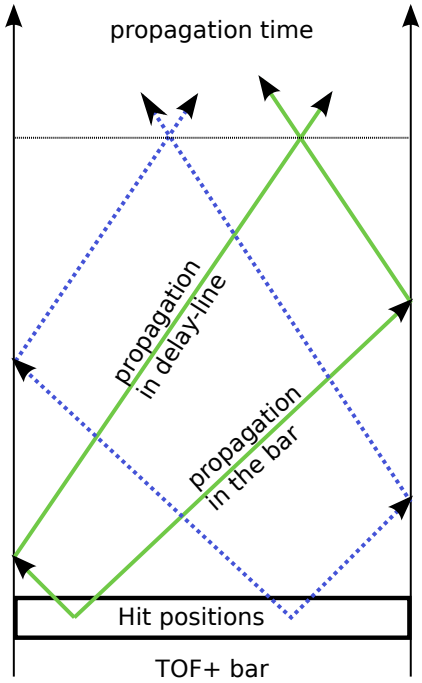

Figure 5.5.: Time propagation of the signals in the bar and delay-line of meantimer.

This principle can be mathematically demonstrated. From the time of the hit, the two times when signals reach both PMTs are defined by:

$$\begin{cases} t_{left} &= (L_{bar}/2 + x_{hit})/v_{bar} \\ t_{right} &= (L_{bar}/2 - x_{hit})/v_{bar} \end{cases} \tag{5.1}$$

And the time when both logic signals are in coincidence is expressed by:

$$\begin{cases} t_c &= (L_{delay}/2 + x_{coinci})/v_{delay} + t_{left} \\ t_c &= (L_{delay}/2 - x_{coinci})/v_{delay} + t_{right} \end{cases} \tag{5.2}$$

The coincidence time is then:

$$t_c = 1/2 \cdot L_{delay}/v_{delay} + 1/2 \cdot (t_{left} + t_{right}) \tag{5.3}$$

$$= 1/2 \cdot \frac{L_{delay}}{v_{delay}} + 1/2 \cdot \frac{L_{bar}}{v_{bar}} \tag{5.4}$$

Thus, it can be found that the defined time is always constant. Even with bars which have a hole, a mean time can be defined. In addition to the fact that those equations show that it is possible to create a logic signal produced in a constant time, it is also possible to create a *mean-pulser* principle. Indeed, with the same delay chain principle, it is viable to obtain a mean value of the pulse width from both analog signals. The time of the trailing edge of the logic signal can be formulated with the same expression as Eq. 5.1 and the coincidence of the trailing edge can be also defined as in Eq. 5.2. At the same time, the trailing edge is $t_{left} + Width_{left}$ or $t_{right} + Width_{right}$, which gives a coincidence time for the trailing edge defined by:

$$t_{c2} = 1/2 \cdot \frac{L_{delay}}{v_{delay}} + 1/2 \cdot \frac{L_{bar}}{v_{bar}} + 1/2 \cdot (Width_{left} + Width_{right}) \tag{5.5}$$

Thus, the resulting signal after the coincidence of the two delay chains is produced in constant time. Moreover, the width of this signal is the average of both input signals $t_{c2} - t_c = 1/2 \cdot (Width_{left} + Width_{right})$. The important point about the delay chains is

that these chains have to be long enough to allow the coincidence between the two input signals, from their leading edge to their trailing edge.

Design and implementation

The principle described above has been implemented in an onboard circuit by discretization of the two delay chains by a serial of delay cells as in Figure 5.6.

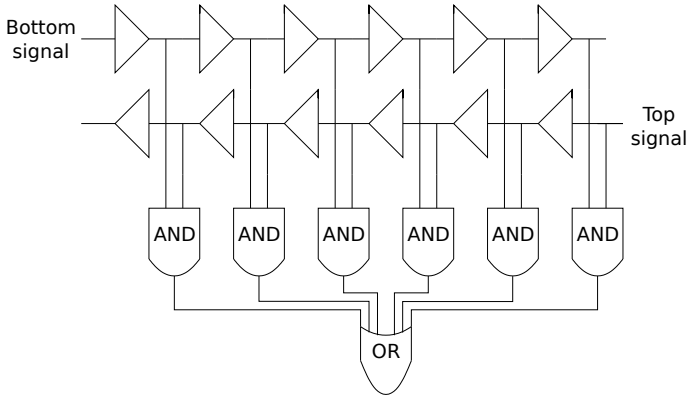

Figure 5.6.: Scheme of the mean timer circuit.

The TOF+ trigger system consists of two pieces. First, there is the time-over-threshold discriminator which contains also the meantimer circuit. In the second stage, the VUPROM2 logic module is used for the pulse analysis and the trigger decision of the Z=2 trigger. The resulting decision is fed to the master trigger system.

The time-over-threshold discriminator is a Camac discriminator from the BNL-E949 experiment [86] which is equipped with a *"complex programmable logic device"* chip (CPLD), equivalent to a FPGA chip. Figure 5.7 is a block diagram of this module. The programmable chip is used to process logic signals after the discrimination. The meantimer circuit has been implemented in this CPLD chip, using the AHDL language, which has logic elements called "delay cells" of 1 ns.

The second part of the trigger system has been implemented in one VUPROM2 logic module already discussed in this chapter. A simulation of the procedure for the pulse width analysis has been performed. The principle of the pulse width analyzer is to propagate the incoming logic signal to another delay chain and to wait until the length of the signal is long enough to fire several requested cells or bits in this chain. Onboard VUPROM2 delay cells are in this case composed by D flip-flops synchronized with a 300

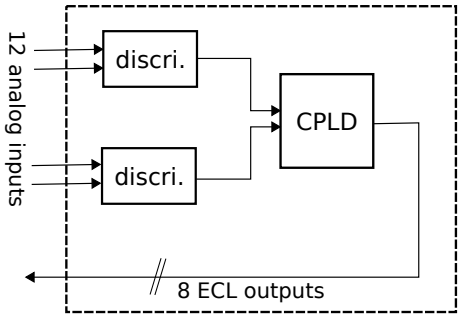

Figure 5.7.: Diagram of the camac module with a discriminator and CPLD chip.

MHz clock, giving a granularity of 3.33 ns per cell. The delay chain of flip-flops has the same structure as a shift register with the depth equal to the length of the delay chain. The incoming signal to be analyzed is fed to the serial input of the shift register and propagated. In order to judge the length of the incoming signal, the shift register needs to be equipped with a parallel output, which corresponds to the states of each flip-flop. In detail, this chain is named as a shift register with a configuration Serial-In Parallel-Out. After propagating the incoming signal in this shift register with a 300 MHz clock time, each of its bits can be examined to select the requested pulse width.

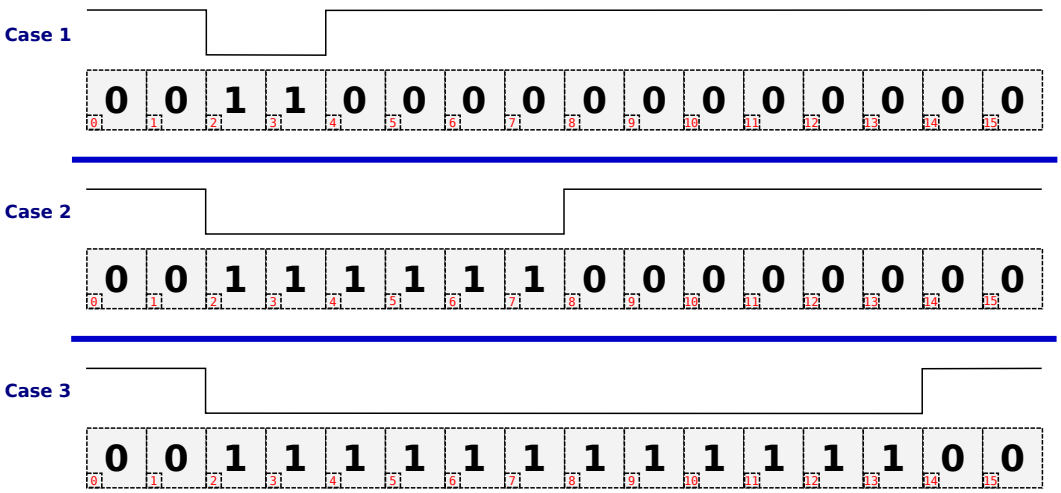

Figure 5.8.: Incoming logic signal with its status in the 16-bit shift register. Three cases with three different pulse widths.

Figure 5.8 shows three different cases in which an incoming logic signal propagates in a 16-bit shift register to illustrate the selection procedure. The coincidence between consecutive fired bits in the register allows to select certain pulse widths with an accuracy of the clock period. Indeed, in Figure 5.8, for instance, if states of bit 2 to bit 5 are requested to be

'1', the case 1 is rejected while the cases 2 and 3 are selected. At the same time, if an upper limit is also set, such as vetoing signal which has bit 2 to bit 11 in Figure 5.8, a case of a too wide pulse is also rejected. A lower and higher limit can be set to select only a specific range of pulse widths.

The investigation on the TOF+ trigger design gives the block diagram shown in Figure 5.9, from the analog signal from PMTs of one bar to the trigger decision. The full trigger system consists of such a decision chain for each bar of the TOF+ wall.

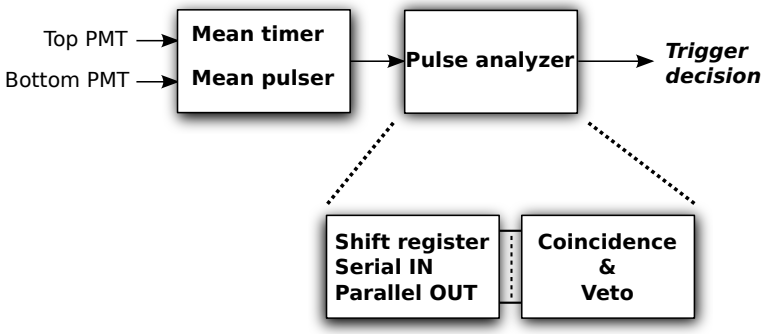

Figure 5.9.: Scheme of the onboard algorithm for one bar of the TOF+ wall.

Implementations and tests

A first test of the meantimer circuit has been carried out to demonstrate that the circuit properly delivers the output signal in constant time with an averaged pulse width. Logic signals after the threshold discriminator were split into two separated branches. One branch is fed to the meantimer circuit, while the other one is directly fed to a commercial CAEN TDC module which also records output signals from the meantimer. The TDC module measures the time from a common start to the leading edge and trailing edge of each signal. Thus, after recording the data, the pulse width of each logic signal can be calculated. The pulse width of the output signal of the meantimer is compared to the average of the two incoming signals calculated offline. The correlation profile between online and offline pulse width calculations of those two branches has been fitted with a straight line. The proportionality constant of each discriminator channel is plotted in Figure 5.10 (left) for tests with a run in laboratory (in blue) and a cosmic run (in black) in the experimental area. It shows a reasonable correspondence in both cases, in which the mean ratio is 1.016. On the right panel of Figure 5.10, the RMS value of the

Gaussian distribution of the online-offline difference is plotted for each channel of the tested discriminator. The mean value of this RMS distribution is 0.64 ns. This indicates that the meantimer circuit properly processes the average width with a good accuracy.

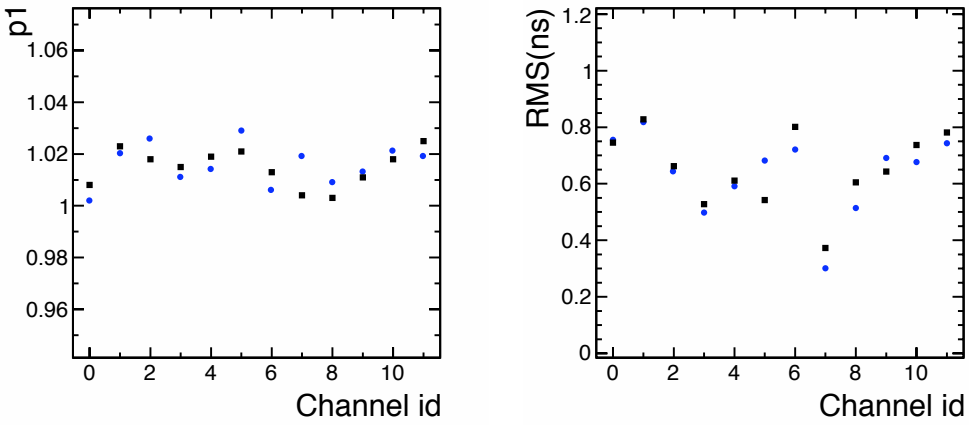

Figure 5.10.: Comparison between the online average of the pulse width and the width calculations of the same pulse offline. Left panel: the slope of the linear fit for each channel of the discriminator. Right panel: the RMS in ns of the difference online-offline for each channel.

A correlation between the measurement of the pulse width and the energy deposit in a scintillator bar has been investigated during a test experiment. The experiment involved two plastic scintillator detectors for the start and stop of the time-of-flight measurements, a prototype of two layers of fiber detectors, and three prototypes of scintillator bars of the TOF+ wall placed in a horizontal plane. Every detector was aligned in an axis rotated from the center of the target by 10 degrees from the beam axis. The beam used during the test experiment was ^{58}Ni at 0.85 A GeV and 1.9 A GeV and ^{12}C at 0.85 A GeV on a carbon target similar to the one of Phase 0. Time-of-flight and energy deposit from the start detector and all the three bars of TOF+ wall were measured to perform the particle identification. With the three TOF+ prototypes, the pulse width measurement was performed offline with the recorded time of leading and trailing edges of the logic signals. Figure 5.11 shows a correlation profile between the pulse width calculated offline and the normalized energy deposit for a single scintillator bar. It can be clearly observed in the figure that the measured pulse width is properly correlated to the energy deposit and thus to the Z^2 value of a particle in the TOF+ bar. This demonstrates that the width information via the time-over-threshold measurement can select the charge of the incoming particles of TOF+, especially for charged particles with Z= 2 .

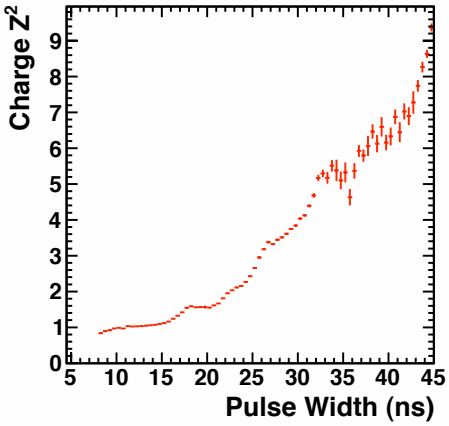

Figure 5.11.: Profile of the correlation between the pulse width of logic signals after time-over-threshold discrimination and the energy deposit in the TOF+ bar normalized to the energy deposit of MIPs. A strong correlation can be seen around the energy deposit of Z=2.

The efficiency of the Z=2 selection via this time-over-threshold measurement and the contamination from other species have been also investigated. The number of Z=2 particles selected and the number of miss-selections have been estimated by varying the interval of pulse width for the Z=2 selection. Figure 5.12 represents the systematic study estimating the contamination of other selected particles trough the pulse width selection as a function of the efficiency of the proper Z=2 selection. It shows a large amount of contamination of two Z=1 particles interacting in the prototype bar. It has to be reminded that the test setup of TOF+ bar was placed horizontally, and considering the reaction mechanism which had taken place, a large amount of Z=1 particles has been produced per reaction. With the specific position of the prototype bars, the amount of two Z=1 particles can be explained. In the Phase 0 experiment, the position of the TOF+ wall is such that the number of double hits in a same bar is very low, as shown in Table 4.1 of Chapter 4. Therefore, this contamination could be neglected. The two other contaminations, from single Z=1 and Z=3 particles, are fairly low. They are 0.4% and 2%-8% respectively when a very good Z=2 selection efficiency is considered. The contamination from Z=3 particles can also be neglected because in the Phase 0 experiment, the remaining ^{6}Li beam passes through the beam hole without interaction. Therefore, it should not affect the trigger decision. A major effort has to be made to reject Z=1 particles from the trigger decision since the common pattern in the hypernuclei decay is the Z=2 particles. In Figure 5.12,

the contamination of Z=1 particles is not increased when a loss interval of pulse width selection for Z=2 particles is used to reach the efficiency of 99%.

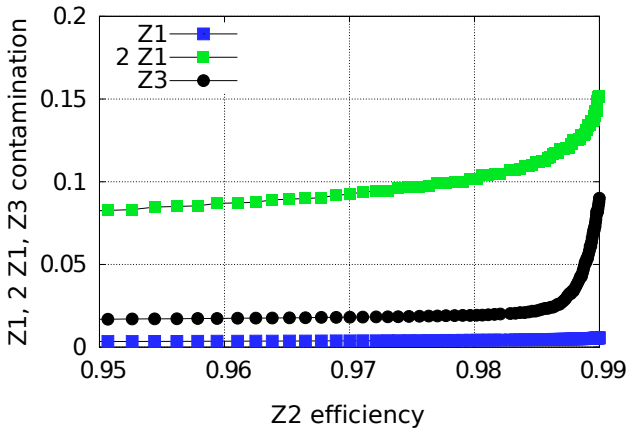

Figure 5.12.: Z=1, two-Z=1 and Z=3 particle contamination as a function of Z=2 particle selection efficiency (see text for more details).

This first test of the dedicated electronics for the TOF+ trigger with the TOF+ wall prototype has established the feasibility of the time-over-threshold measurement for particle discrimination. Another test experiment was performed with seven prototypes which had the configuration of the TOF+ wall but again placed horizontally.

This prototype of TOF+ wall was connected to the full electronic chain, including the programmable discriminators for the meantimer circuit as discussed in Section 5.2.1 and the VUPROM2 logic module for the pulse width measurement and analysis. In the experiment, averaging of the pulse width was performed online in the electronic circuit of the meantimer. The purpose of this experiment was to confirm the results of the previous test experiment presented above when all the processes are performed onboard. The beam condition was identical as the one of the Phase 0 experiment, a ^{6}Li beam at 2 A GeV on a carbon target. The main interest of the trigger study was to perform the particle identification independently in order to examine the efficiency of the pulse width selection.

In Figure 5.13, a distribution of the pulse width of independently selected Z=1 and Z=2 particles is plotted. The Z=1 particle contamination is observed in the figure when the pulse width is between 42 ns and 50 ns. In this study, the efficiency to select Z=2 particles with the pulse width measured by the VUPROM2 module was checked. In the offline analysis, the interval mentioned above was used to tag particles detected in a scintillator bar. Then, according to each trigger tag, the particle identification was performed independently. The efficiency of Z=2 particle tags has been thus estimated to

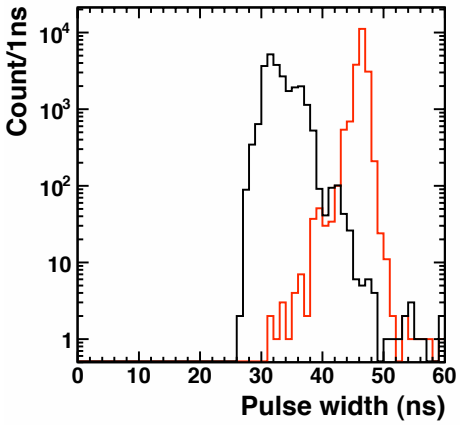

Figure 5.13.: Pulse width of Z=1 particles (in black) and Z=2 particles (in red) with independent particle selection.

be 99% and the Z=1 particle contamination was around 0.4%. Those values confirmed the results of the previous measurements.

Achieved performances

The design of the Z=2 trigger has been established during two test experiments. Values for each interval of selection have been deduced. For the Phase 0 experiment, only the lower bound between Z=1 and Z=2 particle selection has been set up to 37 ns in order to be on the safe side. The trigger decision sent to the master trigger module consists of 8 output channels, each of them representing 4 neighboring bars.

The effects of the Z=2 trigger are plotted in Figure 5.14. For each set of 4 neighboring bars, the amount of identified particles in respect to their energy deposit is plotted for two different trigger types. One corresponds to the minimum bias trigger which does not include the Z=2 trigger. The second trigger type is the hypernuclear trigger in which the Z=2 trigger is requested. Each amount of identified particles in each bar set is normalized by the total of counts in the set of interest.

Figure 5.14 shows, in the bottom left panel, a clear enhancement of the yield of Z=2 particles when the Z=2 trigger is requested. The reduction of the Z=1 particle yield is also visible in the top left panel. The set of bars numbered 2, 3, and 4 is placed where most of the Z=2 particles hit the TOF+ wall. The sets of bars ranging from number 6 to 8 correspond to the side of the TOF+ wall where there is no Z=2 particle hit. For

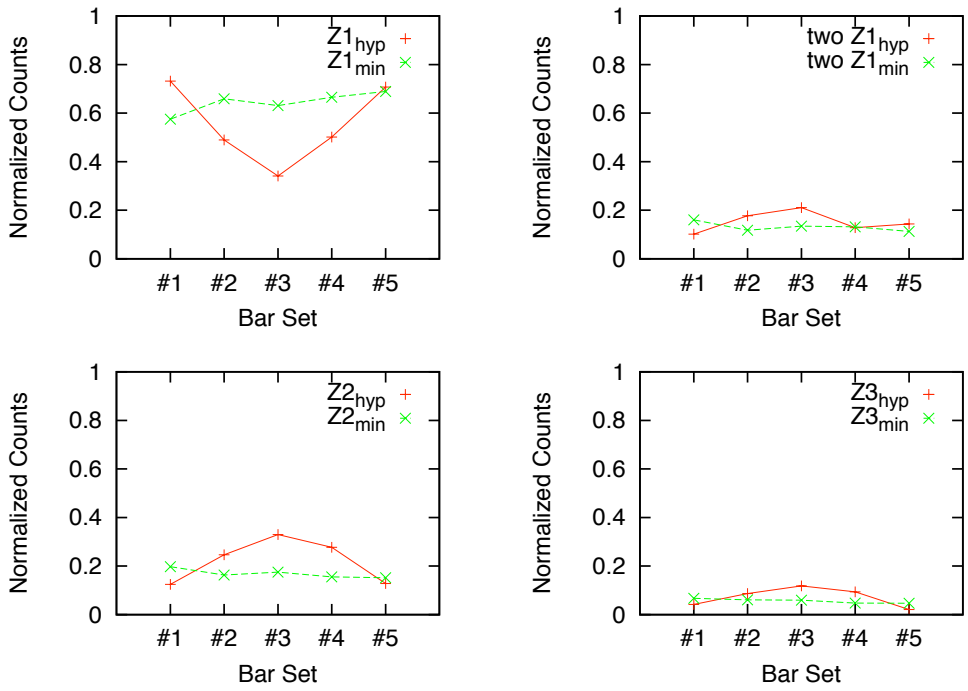

Figure 5.14.: Energy deposit in sets of scintillating bar. In green, yields from events tagged without Z=2 trigger while in red events are tagged with this trigger

this reason, those sets are not shown in Figure 5.14. The increase of Z=2 particle yield with a decrease of the Z=1 particle yield demonstrates that the Z=2 trigger tag worked as expected. Figure 5.14 shows also, in the top right panel, that the two Z=1 particle contamination is not so significant as it has been discussed, since the yield of two Z=1 particles is slightly constant. The contamination of Z=3 particles can be considered small as well, since there is no significant enhancement.

5.2.2. Secondary vertex tagging stage

The purpose of the secondary vertex trigger subsystem is to examine the presence of a secondary vertex between the two sets of fiber detectors TR0 and TR1 where the decay volume for hypernuclei and Λ particles is located.

Template matching: principle and methods

The idea behind *Template matching* is to define a track template from a collection of hits from the three sets of fiber detectors TR0, 1 and 2. By computing all possible track templates for primary tracks coming from the target and implementing them inside the trigger module, the vertex trigger aims to veto all those primary tracks and check all remaining hits on TR1 and TR2. Every template has been determined by Monte Carlo simulations. They combine the coincidence between hits from the three sets of fiber detector, which correspond to a primary track. Those templates form the veto matrix for primary tracks. Since each x- and y-layer of fiber tracker is independent, each plane is considered and the veto matrix consists of two parts for both layers.

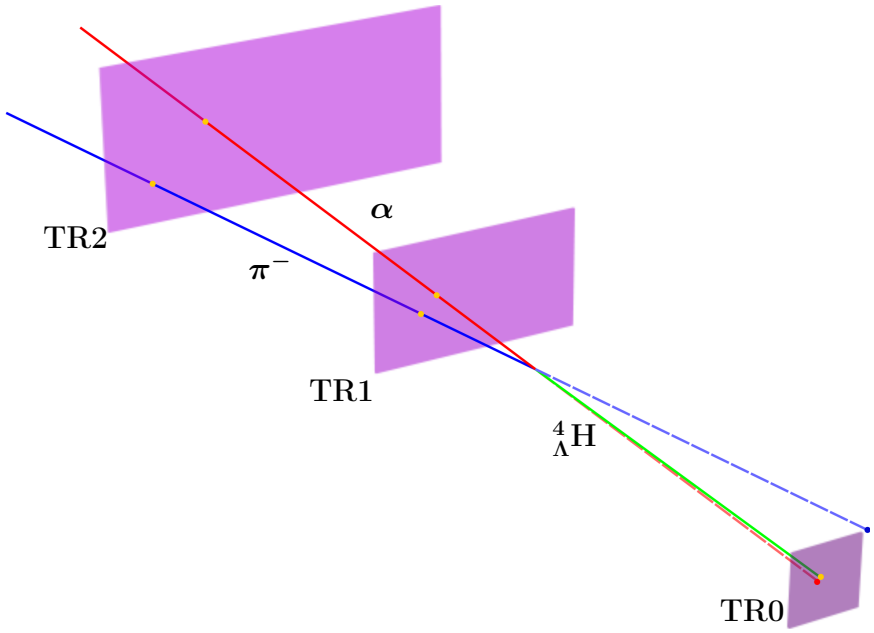

Figure 5.15.: Principle of the secondary vertex trigger: typical hypernuclear two body decay with a decay vertex behind the TR0 fiber detector. The primary track of a hypernucleus (in green), secondary tracks of the remaining fragments (in red) and associated π^- (in blue) are represented. Hits of each particle are rendered in yellow for each detector layer. Each secondary track has been propagated backward to the TR0 detection plane.

By vetoing the primary tracks, the remaining hit pattern corresponds to the π^- track from hypernuclear or Λ decay. An example of hypernuclear decay is shown in Figure 5.15. Thanks to the higher momentum kick for π^-, most of the π^- tracks (in blue in the figure) do not match the hits in the TR0 fiber detector, while the fragment from the hypernuclear

decay (in red) has a similar propagation as the hypernuclei (in green) coming from the target. The dashed line represents the backward propagation of the secondary tracks to the TR0 detector. It is observed in the figure that the track of fragments is very close to the hit from a hypernucleus. However the π^- track is not even on the detector plane. Vetoing the primary track pattern allows only tracks which correspond to a momentum kick which takes place behind the TR0 fiber detector.

Design of the secondary vertex trigger system

The veto matrix from the MC simulations gives for each primary track a triplet index of hits on each fiber detector corresponding to the tracks. The idea of vetoing is to reject the hits belonging to those primary tracks on each tracker behind the decay volume and then to evaluate the remaining hits. For this purpose, coincidence matrices for each x- and y-layer of TR1 and TR2 are built. Table 5.1 summarizes the number of needed evaluations in the coincidence matrix of each layer to veto the hits from the primary tracks.

Table 5.1.: Number of evaluations needed per fiber layer after the decay volume.

Layer	TR1x	TR1y	TR2x	TR2y
Matrix input	64 × 206	64 × 190	64 × 222	64 × 126
# Channels	222	126	206	190
Total evaluation	> 290k	> 150k	> 300k	>150k

A large number of channels to be processed in the trigger stage needs a fast and dense implementation. FPGA chips can fulfill this requirement, especially the VUPROM2 logic modules with their high density input.

The MC simulations of the vertex trigger system have shown that the trigger efficiency for hypernuclear events is about 20% with a background contamination of 2.8%.

An organization of the full vertex trigger is shown in Figure 5.16. It consists of four stages of VUPROM2 logic modules. As discussed in Section 5.1.2, VUPROM2 modules are used as TDC and scaler modules for all fiber trackers and drift chambers. The first stage is made of these VUPROM2 modules. In addition of TDC and scaler functionalities, those first stage modules are also used to fan-out each input in order to duplicate the signals to feed them to the next stage.

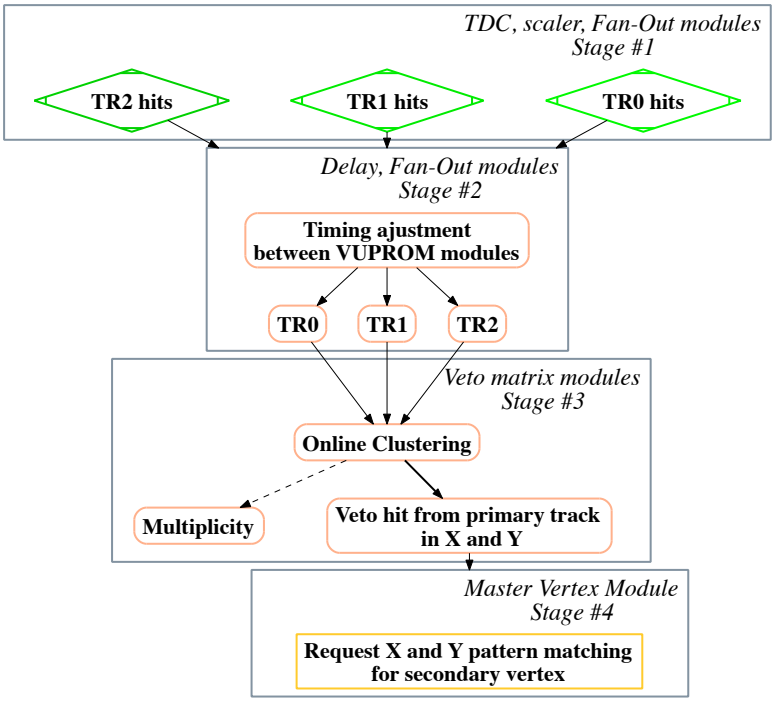

Figure 5.16.: Diagram of the complete vertex trigger subsystem with the main functionalities of each stage.

The second stage is to adjust the timing between all signals coming from the different VUPROM2 modules before feeding them to the veto matrix modules. Incoming signals to the veto matrix modules are clustered up to 6 neighboring channels in order to reduce the number of channels to evaluate and to reduce potential cross talk noise from PMTs of the fiber detectors.

Each hit pattern corresponding to a primary track template is vetoed and only the remaining hit is fed to the last stage in the master vertex module. A decision is taken corresponding to the remaining multiplicity after primary track veto. The multiplicity of each fiber layer is also measured and can be used in the main master trigger module for full event tagging.

Implementation and achieved performances

The full implementation of the vertex trigger subsystem uses 38 VUPROM2 modules corresponding to the diagram of Figure 5.16. However, before the complete trigger system, the algorithm for online clustering has been successfully tested during a beam experiment.

During the data taking of the Phase 0 experiments in August and October 2009, the trigger decision taken by the secondary vertex trigger system has been recorded for each event. Each channel which was not vetoed has been also sent to the TDC function of the VUPROM2 module, while the master trigger module took the decision. With the information of fired fiber channels before any clustering, an offline analysis tries to reproduce the trigger decision. For this purpose, this offline analysis has to simulate the online clustering by taking care of the coincidence window of each incoming signal, since the time information for each channel is available from the TDC functionality. After matching the online clustering, the offline analysis uses the veto matrix file used to generate the FPGA implementation of this veto matrix. With the *a posteriori* decision making analysis, incoming fired channels can be sorted in two categories, one corresponding vetoed channels and the other to granted one.

On an event by event basis, all the channels which have been accepted and recorded after the veto matrix stage can be compared to the offline analysis. This comparison warrants the consistency of online decisions and thus of the full implementation of the vertex trigger with the initial idea of the trigger design.

Since vetoed channels during the data acquisition are unknown, only accepted channels are recorded. Thus, channels which are vetoed during the offline decision analysis should not be found among recorded channels after the veto stage. In the same way, the latter channels should be found as passed in the offline analysis. Figure 5.17 shows a summary of the consistency check for each fiber layer, TR1y, TR2y, TR1x and TR2x. The two first bins correspond to consistent status between online and offline decisions, the first one when channels are passing the veto matrix in both cases, and the second one when they are vetoed on- and offline. The *Unknown* status, stands for cases in which recorded data after the vetoed matrix are not sufficient to determine the consistency.

A deep review of the channels returning the *Unknown* status reveals that those channels are not found in any of vetoed or passed offline categories. It indicates that there is no online channels in the considered event which could give those channels. The *Inconsistent*

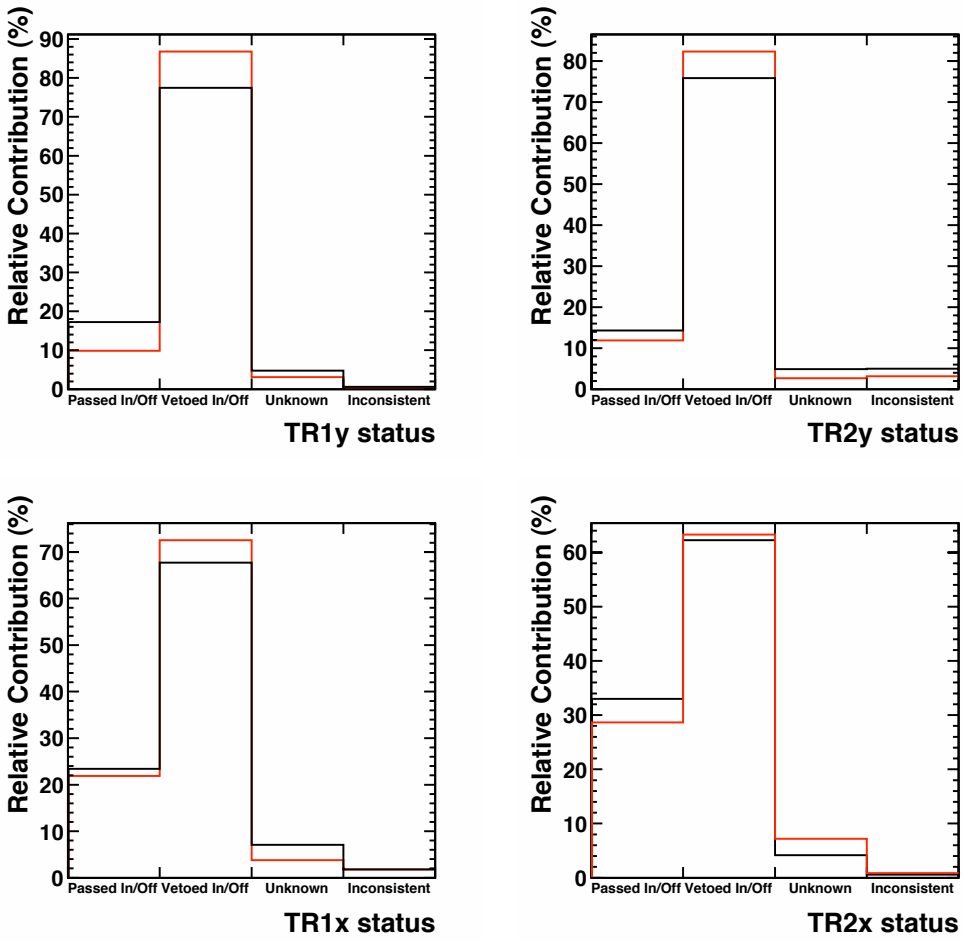

Figure 5.17.: Comparison between online and offline decisions of the vertex trigger for each fiber layer TR{1,2}{x,y}. *Passed In/Off* and *Vetoed In/Off* correspond to a consistent status of evaluated channels. The *Unknown* status means that the recorded data are not sufficient to explain the current channel status while the *Inconsistent* flag represents a complete inconsistent decision taken online and by the offline analysis. The black color represents the hypernuclear trigger selection in which the vertex trigger is requested, while the red color corresponds to the minimum bias trigger selection. For each trigger type, counts are normalized (and shown in %) in order to compare to each other.

status arises when online passed channels are found to be vetoed during the offline decision analysis.

Figure 5.17 also gathers analysis results of two different trigger type selections. The black color corresponds to events tagged with the hypernuclear trigger which includes the vertex trigger system while the red color represents the minimum biased events.

The first outcome of this comparison is the fairly low level of inconsistency between online and offline decisions. In average between TR{1,2}{x,y}, only 1.74% ± 0.57 of the online passed channels should be vetoed according to the offline analysis. This gives a mean consistent level of 98.26% ± 0.57. If *Unknown* status yield is included, it becomes 93.57% ± 0.79.

The second important result is the difference between minimum bias events and events triggered by the hypernuclear trigger. First of all, it is clearly observed that the balance between passed and vetoed channels is different between both trigger types. Indeed, there are more vetoed channels for minimum bias events (around 76.25% ± 5.24) in comparison to hypernuclear trigger type events (70.82% ± 3.55), which shows that an event with the hypernuclear trigger produces more accepted channels. The minimum bias trigger emphasizes events with primary tracks, while the hypernuclear trigger requests tracks from secondary vertices. The concept of these triggers explains the difference between the yields observed in Figure 5.17.

From the offline analysis, vetoed hits can be determined, and it is possible to illustrate the hit profile dependency on the vertex trigger decision. In Figure 5.18, the hit profile in each fiber layer for all the hits is represented with the contribution of vetoed (in dashed line) and passed (in red line) hits. The vetoed part corresponds to hits which are considered to be consistently vetoed, and, in each layer, their profile coincides with the area of primary track hits, which is observed in simulations. The hit profile representing those channels which have passed the veto stages is nearly flat, except for few noisy channels, where the hit profiles from secondary tracks are expected .

The behavior of achieved vertex trigger system has been analyzed and has fulfilled the design with a fairly good agreement with the simulations. Hit profiles give also a reasonably good consistency with the Monte Carlo simulations.

5.2.3. π^- detection tagging stage

Another part of the trigger decision includes the requirement of the detection of a π^- meson in the TFW wall which accepts mainly π^-. Since this trigger condition is rather simple in comparison to the two other trigger tags, a simple coincidence between both signals from the PMTs of the vertical scintillating bars is requested. The method of the meantimer, discussed in Section 5.2.1, has been used in order to obtain a trigger

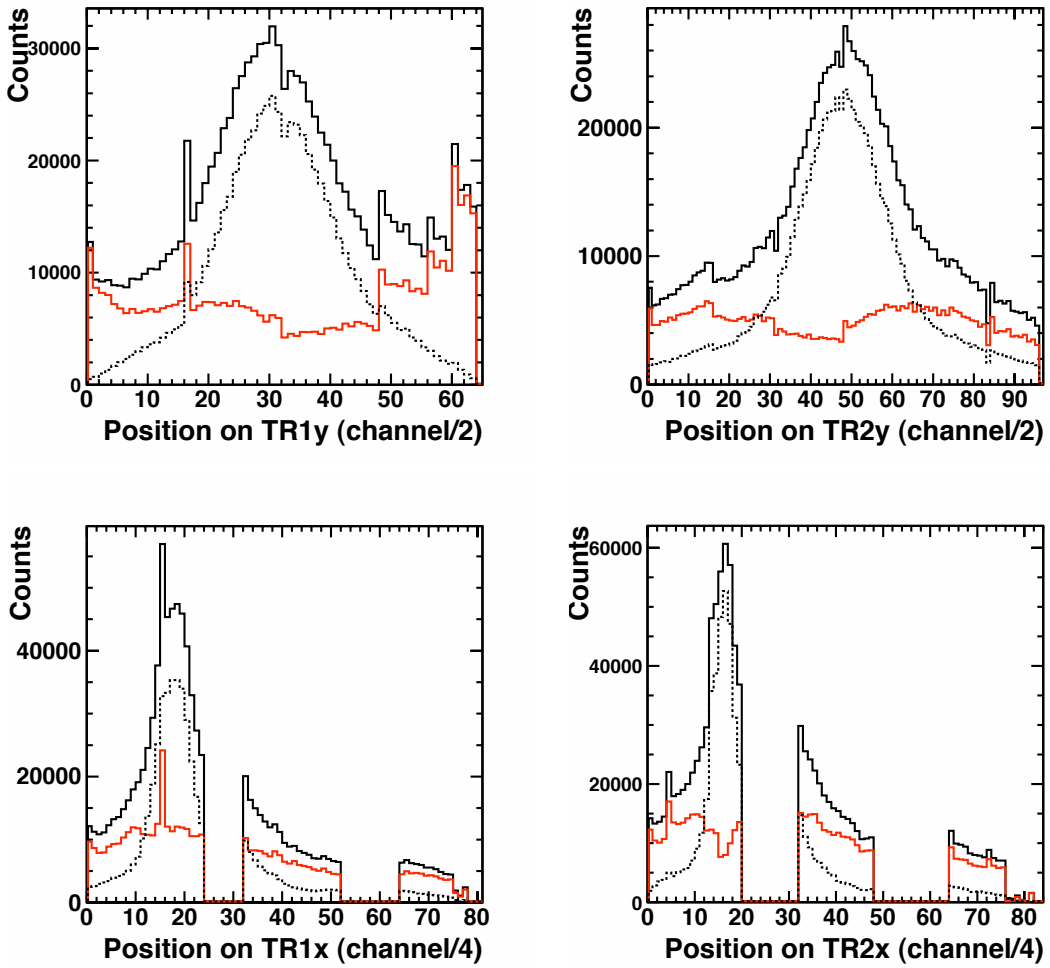

Figure 5.18.: Hit distribution on each fiber layer TR{1,2}{x,y}. In solid black line, the complete hit profile. In dashed line, hits which have been vetoed, obtained consistently by the offline analysis. In red color, hits which have passed online and offline the veto stage. The x-axis is indexed by detector channel divided by 2 or 4 because the output cable of the VUPROM2 modules of the veto stage has 32 channels and each portion of the incoming signal passing the veto stages has been or-ed to match this restriction. The visible gaps in TR{1,2}x are a consequence of this property: output signals have been or-ed 4 by 4, giving not 32 channels but less. (each new part starts at channel 32 or channel 64 corresponding to another module).

timing being independent of the hit position in the bar. The meantimer method needs the coincidence between both input signals, therefore the output logic signals of the electronics are fed directly to the master trigger module.

5.2.4. Full trigger system

The complete trigger system in the data acquisition system has been realized with a total of 42 VUPROM2 modules shared between the three sub parts, the secondary vertex trigger, the Z=2 trigger and the π^- detection trigger. The latest stage of the trigger system gives a decision within 300 ns. Four different types of physics triggers have been implemented. The first one, the *minimum bias* trigger requires only a hit in the TOF-start detector and at least one hit on any fiber detector. It allows to record any data with a minimum bias, useful to collect beam background events. The *reaction* trigger is used to acquire fragmentation events. It requests TOF-start detector, any fiber detector hit plus a higher multiplicity on TR1 and any hit in the TOF+ wall. The two last trigger patterns are used to select hypernuclear event candidates. One focuses on any *hypernuclear* events and another on *Helium hypernuclear* three body decay events. Two mixtures of events have been selected during the experiment. Each mixture of events consists of minimum bias and reaction events which are scaled down and one of the hypernuclear trigger as explained in Section 5.1.4. It allows to gather a combination of several trigger patterns with a scaling factor to weigh the importance of the selected events. Table 5.2 summarizes the different conditions requested for the trigger pattern.

In the HypHI Phase 0 experiment, the data rate was 2.6 kHz with a beam intensity of 3.2 $\times$ 10^6 Li^6 per second for the mixed trigger 1, and 1.2 kHz with an intensity of 1.8 $\times$ 10^7 particles per second for the second mixed trigger.

Table 5.2.: Conditions requested for each trigger type: minimum bias trigger, reaction trigger, hypernuclear trigger and He hypernuclear trigger.

Trigger		Min bias	Reaction	Hypernuclear	He Hypernuclear
Vertex	Mult$\geqslant$1			On	On
	Mult$\geqslant$2				On
TR012	Mult$\geqslant$1	On	On	On	On
TR1	Mult$\geqslant$2		On	On	On
TOF+	Z$\geqslant$1 Mult$\geqslant$1		On	On	On
	Z$\geqslant$2 Mult$\geqslant$1			On	On
TOF-	π^- Mult$\geqslant$1			On	On
TOFstart	Mult$\geqslant$1	On	On	On	On
	Mult$\leqslant$2			On	On
Scaling factor		1/65536		1	
Mixed Trigger 1		On	On	On	
Mixed Trigger 2		On	On		On

6

Development of analysis software for the Phase 0 experiment

The third part of the present work has been to develop methods for data analysis softwares in addition to the design study and implementation of the experimental apparatus (Chapter 4) and the development and realization of the trigger systems (Chapter 5). In the present chapter, the implementation of online and offline analysis softwares is presented.

Each detector gives several measurements to process from a not direct exploitable data to different more useful data structures. The final stage of the analysis is the event reconstruction. It includes the momentum reconstruction of each potential track and the mass calculation for each detected particle. With the information of the secondary vertex of the hypernuclear decay, hypernuclear events can be reconstructed.

The online and offline analysis strategy is first described before presenting the procedure of the track reconstruction. The tracking system provides information on the particle position which has to be combined in order to recognize and reconstruct the path of the particles. The track extrapolation methods underlie the track reconstruction procedure, and the chosen method for track extrapolation is presented in comparison of the standard method. Several track finding methods are then discussed and the approach chosen for the track reconstruction is reported. The track fitting based on the Kalman Filter is presented. The simulation study of the track reconstruction methods is described and the achieved performance of the tracking in the reconstruction procedure, obtained by a systemic study, is reported.

The event reconstruction strategy based on the track reconstruction is then described in the last part of this chapter. The different cut conditions used to reject the combinatorial background in the hypernuclear event reconstruction are presented. The efficiency of each cut has been investigated during a background rejection study. The results show the power of the background rejection of these cut conditions. The achieved performances of the hypernuclear event reconstruction are summarized and the expected rates for the reconstructed hypernuclei per week in the Phase 0 experiment are given.

6.1. Online & Offline analysis

The first step of the analysis procedure is to translate recorded digitized data for each detector to data structures suitable for physics analyses. Those data representations contain several physical observables which give a high-level data description easily usable. The main part of the analysis before the event reconstruction process is to handle proper data structures for calibrations of each detector system.

Unpacker As the first step of the analysis, one has to unpack data files which contain recorded measurements. Data are organized module-wise by groups of channels coming from the same electronic module. Hierarchically, each module-wise structure is considered as electronics-wise in a pool of type of electronics. In this step, data size is reduced by pedestal and zero suppression. It gives a first compact data representation which is convenient for the next calibration steps.

Calibration The calibration procedure is spilt in three different subroutines for each detector set. The subroutines are separated in complete independent processes in order to run each of them in parallel or rerun one without affecting the others. Each part includes detectors which can be treated with a similar approach. Time-of-Flight detectors (TOF-start, TOF+, ALADiN and TFW walls) are gathered in the same dedicated part, and the same procedure is done for drift chambers and scintillating fiber detectors. Calibrations include several transformations of unpacked data such as gain matching of amplitude measurements, time reference adjustment and/or position offset of each sub layer of detectors from the target. Since those parts are focused on detectors, the output data are now organized detector-wise.

Merger This step is used to merge all calibrated data in a single data structure and to provide a first set of local observables such as calibrated position in the local system of the detector, the calibrated energy deposit and/or the measured time-of-flight.

Global The last step before the event reconstruction provides observables in the laboratory frame centered at the target position.

Figure 6.1 summarizes all these steps in a data flow diagram. UML (Unified Modeling Language) diagrams of all data structures can be found in the Appendix A.2.

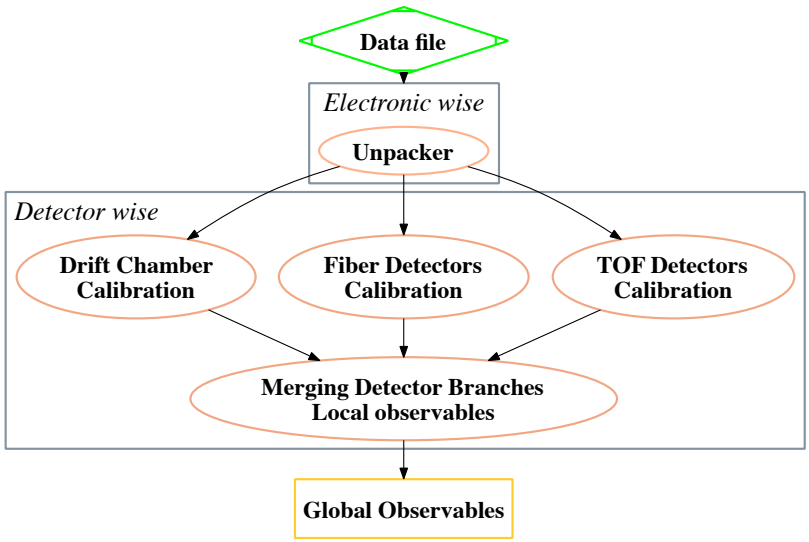

Figure 6.1.: Data flow from raw to reconstructed data structures, including calibration steps for each detector set in parallel. Unpacked raw data is represented in a electronic module-wise data structure. Calibration steps give a new detector-wise representation. Reconstructed data is the merge of detector-wise data structure transposed to the global coordinate system.

The online analysis software is based on the Go4 analysis framework developed by GSI and based on ROOT [87, 88], while the offline analysis is based only on the ROOT framework in order to minimize dependencies. The Unpacker step is bounded on the Go4 framework to be able to handle the file format of recorded data. The online monitoring includes all the detector branches which could be individually turned on or off by the user. The offline analysis involves the same analysis code as for the online one, but without the Go4 dependency or the code responsible for histogramming. Calibration of each detector has been performed in these different steps.

6.2. Track and event reconstruction

Each detector system gives precious information on the particles or nuclei passing through the detectors. However the information has to be combined in order to understand the motion of each particle. The track reconstruction uses the hit information from each available detector station to reproduce the trajectory of particles across the full setup. Its quadrivector **P** can be thus reconstructed from the momentum vector and the mass m of the particle. The momentum vector is calculated from the deflection of the particle inside the magnetic field. The mass is defined by the particle identification involving the momentum and the velocity β obtained through the time-of-flight measurement.

$$m = q \cdot p\sqrt{1/\beta^2 - 1} \tag{6.1}$$

Each particle can be identified by a correlation plot between the calculated momentum and the velocity β for light particles or the energy deposit dE/dx in the last TOF wall for heavier nuclei.

6.2.1. Equation of motion

The key of the track reconstruction is to compute the full trajectory of the particle from its equation of motion especially in the magnetic field which gives the momentum information. In a magnetic field **B**, the differential equation of motion is given by the Lorentz force :

$$\frac{\mathrm{d}}{\mathrm{d}t}(m\gamma\frac{\mathrm{d}\mathbf{x}}{\mathrm{d}t}) = \frac{q}{c}\frac{\mathrm{d}\mathbf{x}}{\mathrm{d}t} \times \mathbf{B} \tag{6.2}$$

Where q is the charge, $\mathbf{v} = \frac{\mathrm{d}\mathbf{x}}{\mathrm{d}t}$ the velocity, and **B** the magnetic field vector. The equation 6.2 can be expressed in terms of the track length parameter s, the distance along the trajectory, by $\mathrm{d}s/\mathrm{d}t = v$ and by introducing the absolute value of the momentum $p = m\gamma\beta c$:

$$\frac{\mathrm{d}^2\mathbf{x}}{\mathrm{d}s^2} = \frac{q}{cp} \cdot \frac{\mathrm{d}\mathbf{x}}{\mathrm{d}s} \times \mathbf{B}(\mathbf{x}(s)) \tag{6.3}$$

The motion of the charged particle along the z-axis can be written from Eq. 6.3 as:

$$\begin{aligned} x'' &= \kappa \cdot (q/p) \cdot \sqrt{1 + x'^2 + y'^2}\,(x'\,y'\,B_x - (1 + x'^2)\,B_y + y'\,B_z) \\ y'' &= \kappa \cdot (q/p) \cdot \sqrt{1 + x'^2 + y'^2}\,((1 + y'^2)\,B_x - x'\,y'\,B_y - x'\,B_z) \\ (q/p)' &= 0 \end{aligned} \tag{6.4}$$

Where $\kappa = 2.99792458 \cdot 10^{-4}$ $_{[(\mathrm{GeV/c})\,\mathrm{T}^{-1}\,\mathrm{mm}^{-1}]}$ and the prime denotes derivatives with respect to z.

6.2.2. Track propagation

Parameter representation

In a fixed target experiment, the most suitable track representation has to gather, into a state vector $\mathbf{r}(z)$, the transversal coordinates $x(z)$, $y(z)$, the two track slopes in xz- and yz-plane, t_x and t_y, and the inverse particle momentum signed according to charge q/p.

$$\mathbf{r}(z) = \begin{pmatrix} x \\ y \\ t_x \\ t_y \\ q/p \end{pmatrix} \tag{6.5}$$

The idea behind the track propagation or extrapolation is to determine the new state vector $\mathbf{r}$ in a new position z_e from a known state vector $\mathbf{r}(z_0) \longmapsto \mathbf{r}(z_e)$. The equation

of motion with the track derivatives on z of the state vector can be written now as an ordinary differential equation (ODE) $\mathrm{d}\mathbf{r}(z)/\mathrm{d}z = \mathbf{f}(z, \mathbf{r})$:

$$\frac{\mathrm{d}\mathbf{r}(z)}{\mathrm{d}z} = \begin{pmatrix} t_x \\ t_y \\ \kappa \cdot (q/p) \cdot \sqrt{1 + x'^2 + y'^2}\,(x'\,y'\,B_x - (1 + x'^2)\,B_y + y'\,B_z) \\ \kappa \cdot (q/p) \cdot \sqrt{1 + x'^2 + y'^2}\,((1 + y'^2)\,B_x - x'\,y'\,B_y - x'\,B_z) \\ 0 \end{pmatrix} \tag{6.6}$$

The covariance matrix $C(z_e)$ has to be calculated as well from the initial covariance matrix $C(z_0)$ and the Jacobian matrix J, the first-order derivative matrix between $\mathbf{r}(z_e)$ and $\mathbf{r}(z_0)$:

$$J = \frac{\mathrm{d}\mathbf{r}(z_e)}{\mathrm{d}\mathbf{r}(z_0)} = \begin{pmatrix} \partial x_e/\partial x_0 & \partial x_e/\partial y_0 & \partial x_e/\partial t_{x_0} & \partial x_e/\partial t_{y_0} & \partial x_e/\partial(q/p) \\ \partial y_e/\partial x_0 & \partial y_e/\partial y_0 & \partial y_e/\partial t_{x_0} & \partial y_e/\partial t_{y_0} & \partial y_e/\partial(q/p) \\ \partial t_{x_e}/\partial x_0 & \partial t_{x_e}/\partial y_0 & \partial t_{x_e}/\partial t_{x_0} & \partial t_{x_e}/\partial t_{y_0} & \partial t_{x_e}/\partial(q/p) \\ \partial t_{y_e}/\partial x_0 & \partial t_{y_e}/\partial y_0 & \partial t_{y_e}/\partial t_{x_0} & \partial t_{y_e}/\partial t_{y_0} & \partial t_{y_e}/\partial(q/p) \\ 0 & 0 & 0 & 0 & 1 \end{pmatrix} \tag{6.7}$$

The extrapolated covariance matrix $C(z_e)$ is obtained from the calculated Jacobian matrix:

$$C(z_e) = J\,C(z_0)\,J^T \tag{6.8}$$

There are several methods which can be used to extrapolate a new state vector $\mathbf{r}$ and its associated covariance matrix C. The classical method used as a track extrapolation is the Runge Kutta method [89]. It is an iterative method for integrating any ODE by performing several evaluations of $\mathbf{f}(z, \mathbf{r})$, in which each integration needs to be calculated on several subintervals for a given precision. Details of the Runge Kutta method can be found in Appendix A.1.1.

Another idea instead of using iterative methods is to use an analytic formula to directly calculate the extrapolated state vector. This method has been developed for the CBM experiment to obtain *an analytic formula for track extrapolation in non-homogeneous magnetic field* [90].

In the equation of motion, Eq. 6.6, knowing an analytic form of the track directions, t_x and t_y, gives an opportunity to calculate the complete state vector. Indeed, coordinates x and y can be determined by integration:

$$\begin{aligned} x(z_e) &= x(z_0) + \int_{z_0}^{z_e} t_x(z)\, dz \\ y(z_e) &= y(z_0) + \int_{z_0}^{z_e} t_y(z)\, dz \end{aligned} \tag{6.9}$$

From Eq. 6.6, the track directions can be written as a function of the magnetic field components as:

$$\begin{cases} t'_x(z) = \sum\limits_{i \subset \{x,y,z\}} B_i(z) \cdot a_i(z) \\ t'_y(z) = \sum\limits_{i \subset \{x,y,z\}} B_i(z) \cdot b_i(z) \end{cases} \tag{6.10}$$

with the functions $a_i(z)$ and $b_i(z)$ defined as:

$$\begin{cases} \mathbf{a}(z) &= h \cdot (\ t_x\, t_y\ ,\ -(1 + {t_x}^2)\ ,\ t_y\ ) \\ \mathbf{b}(z) &= h \cdot (\ (1 + {t_y}^2)\ ,\ -t_x\, t_y\ ,\ -t_x\ ) \end{cases} \tag{6.11}$$

$$\tag{6.12}$$

with:

$$h = \kappa \cdot (q/p) \cdot \sqrt{1 + {t_x}^2 + {t_y}^2} \tag{6.13}$$

and where the components of the magnetic field $\mathbf{B}(z)$ are assumed on the trajectory as a function of z:

$$\mathbf{B}(z) = B(x_{track}(z), y_{track}(z), z) = (\ B_x(z)\ ,\ B_y(z)\ ,\ B_z(z)\ ) \tag{6.14}$$

The idea of this method is to expand the equations 6.10 in series of antiderivatives of the magnetic field **B** by repeated integration of successive derivations of the track directions t_x and t_y. Eqs. 6.10 are linear with respect to the magnetic field, therefore the derivatives of **a** and **b** can be written for these same equations. Complete details of the calculation can be found in Appendix A.1.2.

The extrapolated track parameters with an error of order (n+1) are:

$$\begin{cases} t_x(z_e) &= t_x(z_0) + \sum_{k=1}^{n} \sum_{i\,i_1\cdots i_k \subset \{x,y,z\}} h^k A_{i\,i_1\cdots i_k}\, s_{i\,i_1\cdots i_k} \\ t_y(z_e) &= t_y(z_0) + \sum_{k=1}^{n} \sum_{i\,i_1\cdots i_k \subset \{x,y,z\}} h^k B_{i\,i_1\cdots i_k}\, s_{i\,i_1\cdots i_k} \\ x(z_e) &= x(z_0) + t_x(z_0)\cdot(z_e - z_0) + \sum_{k=1}^{n} \sum_{i\,i_1\cdots i_k \subset \{x,y,z\}} h^k A_{i\,i_1\cdots i_k}\, S_{i\,i_1\cdots i_k} \\ y(z_e) &= y(z_0) + t_y(z_0)\cdot(z_e - z_0) + \sum_{k=1}^{n} \sum_{i\,i_1\cdots i_k \subset \{x,y,z\}} h^k B_{i\,i_1\cdots i_k}\, S_{i\,i_1\cdots i_k} \end{cases} \tag{6.15}$$

With Eq. 6.15, only the repeated integrals of the magnetic field $S_{i\,i_1\cdots i_k}$ and $s_{i\,i_1\cdots i_k}$ have to be calculated along the path of the particle in order to extrapolate the state vector $\mathbf{r}(z)$ of a track. The relevance of this formula for tracking extrapolation is that the steps between initial z_0 position to any z_e position depend only on how the magnetic field can be extrapolated. It is in a completely opposite way of the Runge Kutta method explained in Section A.1.1 for which a small step is required when the magnetic field is non uniform in order to obtain a good accuracy.

This method has been tested and compared with the standard fourth order Runge Kutta method expressed in Ref. [90]. Those two extrapolation methods were used in the Kalman filter procedure of the reconstruction software (CBMroot) of the CBM experiment [91]. Residuals and pulls of the track parameters are shown to be practically identical between the analytic formula of the third order and the fourth-order Runge Kutta method, demonstrating that this new method is worth using inside the fitting procedure of track reconstruction.

The other important issue is to model the magnetic field map of the dipole magnet in a way to be able to integrate it along the trajectory.

6.2.3. Power series of magnetic field components

The profile of the realistic magnetic field map has been already presented in Chapter 4. As discussed in the chapter, the magnetic field derivatives $\partial B/\partial x$ and $\partial B/\partial y$, and the magnetic field components B_x and B_z are negligible. These assumptions give a simplified field map.

The simplified profile has to be used to calculate the variables $S_{i\,i_1\cdots i_k}$ and $s_{i\,i_1\cdots i_k}$ defined in Eq. A.17. They have to be calculated along the approximate trajectory in order to use the analytic formula for the track extrapolation. The analytic formula with a power series to the third order is precise enough for the extrapolation as presented in Ref. [90]. With the simplified field map, only the first three variables of $S_{i\,i_1\cdots i_k}$ and $s_{i\,i_1\cdots i_k}$ have to be computed during the track extrapolation.

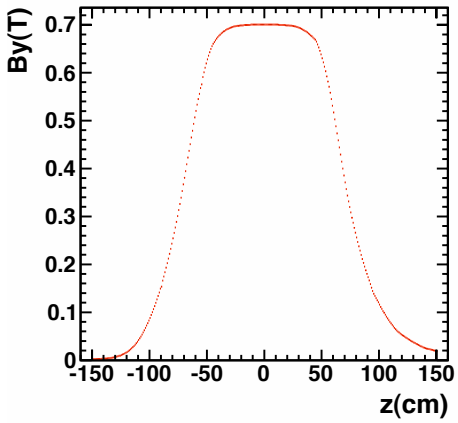

Figure 6.2.: Profile of the y-component of the magnetic field along all trajectories as function of the z direction. Error bars are represented by filled rectangles in red color.

The profile of the magnetic field along the z-direction for all trajectories considered in the simulations is plotted in Figure 6.2. In order to calculate $S_{i\,i_1\cdots i_k}$ and $s_{i\,i_1\cdots i_k}$, the profile has been extrapolated by 2^{nd} order polynomial function over several segments along the z-direction. Those repeated integrals can be formally calculated by knowing an extrapolation form of the field map. A total field length of 3 m has been divided into 13 segments which gives a good extrapolation.

Along each segment, several values of the field components from the field map are fitted by a polynomial function of the 2^{nd} order, which gives the extrapolated function of the field used for integration.

These values have to be as close as possible to the expected magnetic field felt by the particles. To improve the estimation of the field map, a preliminary set of values is extracted by assuming a straight line propagation. A simple track extrapolation using those values gives a new position estimation of the particles in the field. With the improved position estimation, a new set of values for the magnetic field is chosen for the polynomial fit. Figure 6.3 shows the residual of the extrapolated field to the expected magnetic field along the complete track propagation. The RMS value of the distribution is 0.895 mT which demonstrates that the estimation of the field is fair enough.

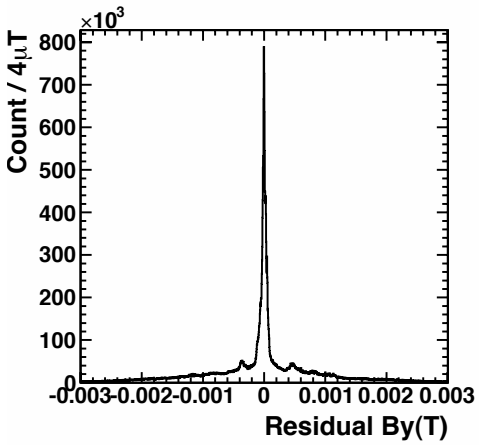

Figure 6.3.: Residual distribution of the extrapolated field compared to the expected magnetic field value.

The extrapolation of the field map by a polynomial function of the 2^{nd} order along several segments has been demonstrated. The field map can also be compacted in the computer memory. In the analysis, the field map has to be completely loaded in memory, which represents around 300 Mb per computer process.

Transversal xy-profile at several steps can be used instead of the full field map for the field extrapolation. A polynomial interpolation can be used instead of a fitting extrapolation. With this method, only a few transversal profiles of the field are needed, reducing the memory consumption and the fitting computation time. However, in the current status of the analysis, the field map is still extrapolated by the fitting procedure, which is explained above.

A gain is significant in running time by using this method for the track propagation in the fitting procedure with the Kalman Filter. For example a complete event reconstruction of 112600 events takes 4 min 21 s on one core of a Intel Core^{TM} 2 Duo T8300 CPU, which

indicates 2.32 ms per event for a full reconstruction, which will be discussed in Chapter 7, instead of 50 ms per event when the Runge Kutta method is used.

6.2.4. Simulation study of event and track reconstruction

In the Phase 0 experiment, the hypernuclear spectroscopy focuses on producing and identifying mainly ${}^{3}_{\Lambda}$H, ${}^{4}_{\Lambda}$H and ${}^{5}_{\Lambda}$He hypernuclei by their mesonic weak decay channels, ${}^{3}_{\Lambda}\mathrm{H} \rightarrow \pi^{-} + {}^{3}\mathrm{He}$, ${}^{4}_{\Lambda}\mathrm{H} \rightarrow \pi^{-} + {}^{4}\mathrm{He}$ and ${}^{5}_{\Lambda}\mathrm{He} \rightarrow \pi^{-} + {}^{4}\mathrm{He} + p$. Identification of hypernuclear events is achieved by vertex reconstruction and the invariant mass method from the track reconstruction of particles from the decay of the hypernucleus. The mean decay length of produced hypernuclei is approximately 15 cm due to a Lorentz factor around 3, since the velocity of the produced hypernuclei is similar to the one of the projectile. Therefore, the decay vertex of the produced hypernuclei takes place well behind the target, which gives an opportunity for clear identification of hypernuclear events in the analysis algorithm.

It has been evaluated that the invariant mass resolution should be at least 5 MeV/c^2 in RMS to demonstrate the feasibility and down to 3 MeV/c^2 to achieve the precise spectroscopy. The major background signal is expected to come from the free Λ decay and the associated fragments from the target since this type of events is not to be rejected by the trigger system as discussed in Chapter 5. The reduction factor between this background and the hypernuclear events is requested to be at least 1% in the mass region of the hypernuclei of interest. The event reconstruction procedure has been studied to achieve an accurate track reconstruction. It is necessary for the invariant mass method and thus for the hypernuclear event identification.

Figure 6.4 shows the schematic layout used in the simulation study. It is based on the initial layout planned for the experiment before the final optimization. The main differences with the setup described in Chapter 3 are the position of the ALADiN TOF wall and TOF+ wall, as well as the non-inclusion of the TFW detector in front of the ALADiN TOF wall. The field map used in the simulation study has a maximum of 0.7 T instead of 0.75 T. All the optimizations have been discussed in Chapter 4, however, the simulation study of the track and event reconstruction do not include those modifications of the setup. The event reconstruction analysis does not depend much on the geometry, thus the revision of the setup does not affect this study. In Figure 6.4, positions of the

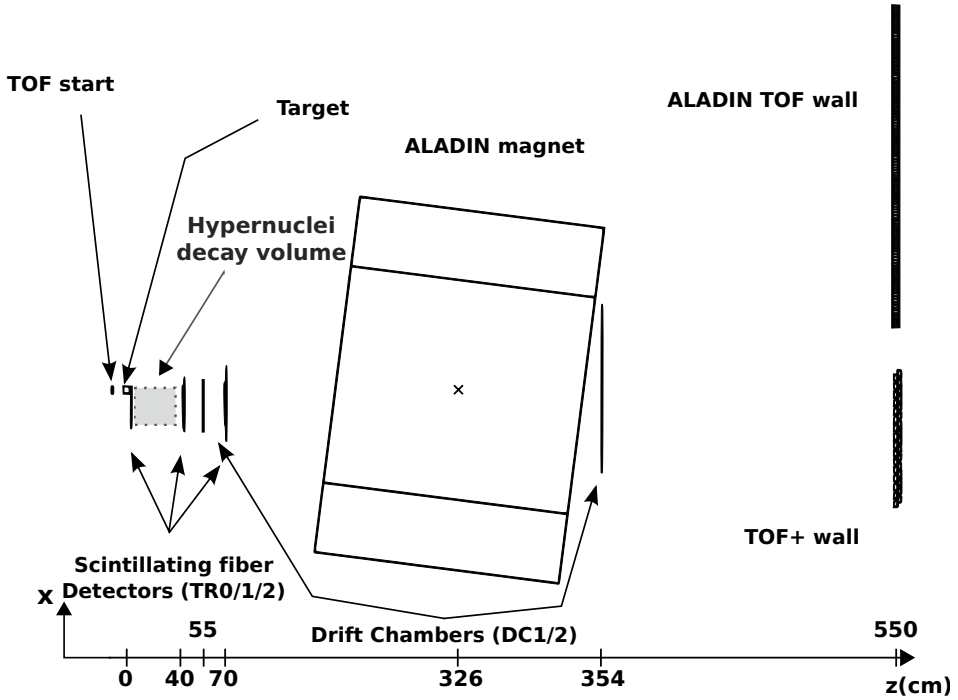

Figure 6.4.: The schematic layout of the experimental setup used in the simulation study with the distance of each detector system from the target.

detectors used in the simulations are annotated on the axis, and the decay volume of the produced hypernuclei is also symbolized by the grey area.

The two drift chambers have been placed between TR1 and TR2 and at the exit of the dipole magnet in order to improve the tracking resolution and the redundancy in the analysis. The addition of two drift chambers has been the starting point of the simulation study and the inclusion of new algorithms for the event reconstruction analysis. The study led to efficiency studies of track and event reconstruction and to evaluate the expected performances for the Phase 0 experiment.

The event generator used for this study is based on the UrQMD model [54] and the GiBUU model [55] presented in Chapter 2. Events from the UrQMD event generator are processed in the experimental setup mentioned above by means of Monte Carlo simulations within the GEANT4 framework [82]. The resolutions of the fiber detectors (TR0, TR1 and TR2), the drift chambers (BDC and SDC), the ALADiN TOF wall and the TOF+ wall, summarized in Table 6.1, have been used in the Monte Carlo simulations to process events through the experimental setup. Those estimations are from each detector commissioning experiments.

Table 6.1.: Summary of position resolutions in RMS of detectors, TR (TR0, TR1 and TR2), Drift Chambers (DC1 & DC2), the ALADiN TOF and TOF+ walls.

	TR	DC	ALADiN TOF	TOF+
x-direction (mm)	0.46	0.3	10	15
y-direction (mm)	0.46	0.3	100	120

The track reconstruction is formed by two main parts. Firstly the track candidates have to be built from the measurements on each detector station. All hits have to be connected to each other in order to conceptualize those tracks. Tracks are fitted to obtain and select the good tracks in the event. The selection of good tracks leads to the event reconstruction which represents the physics processes. Each part of the reconstruction will be presented: the pattern recognition for track finding, the track fitting procedure and then the event reconstruction in Chapter 7.

6.2.5. Pattern recognition for track finding

In the data analysis procedure, pattern recognition algorithms are used to build track candidates in the earliest steps of the data analysis. Those methods are commonly used in offline and/or online analyses to reduce the data flow and to consider anything but the track candidates. This particular step had to be included in the event reconstruction for the Phase 0 experiment.

Among viable global methods of pattern recognition a specific Fuzzy Radon method, so called the Hough Transform [92], has been adopted and implemented in this work.

Hough Transform

The idea behind the algorithm of Hough Transform is to define for each hit in two dimensions, a line, or generally a surface into a feature space [93]. Each hit (x_i, y_i) belonging to a same line verifies $y_i = a \cdot x_i + b$. For each couple (x_i, y_i), a line can be defined in the feature space by $b = -x_i \cdot a + y_i$ where $-x_i$ becomes the slope and y_i the y-intercept. The pattern recognition is then transposed to find the intersect of all those lines in the feature space. Indeed, if a set of hits belongs to a same line, their associated line in the feature space is intersecting into a point which defines the parameters of the initial line.

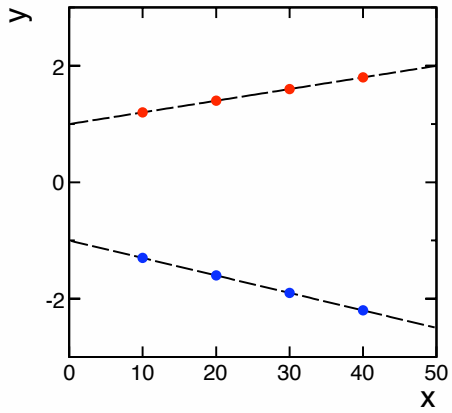

Figure 6.5.: Set of points in 2D space.

In Figure 6.5 there are two tracks plotted with four associated hits. For each of these hits, two parametrization in the feature space are possible: $b = x_i \cdot a + y_i$ or $\rho = x_i \cdot \cos\theta + y_i$. Figure 6.6 shows the two resulting feature spaces. The color of each curve corresponds to the color of the hits in Figure 6.5. It is observed that the curves associated to hits which belong to a same track are all crossing each other at a same point. Finding those intersections defines the parameters of the found tracks.

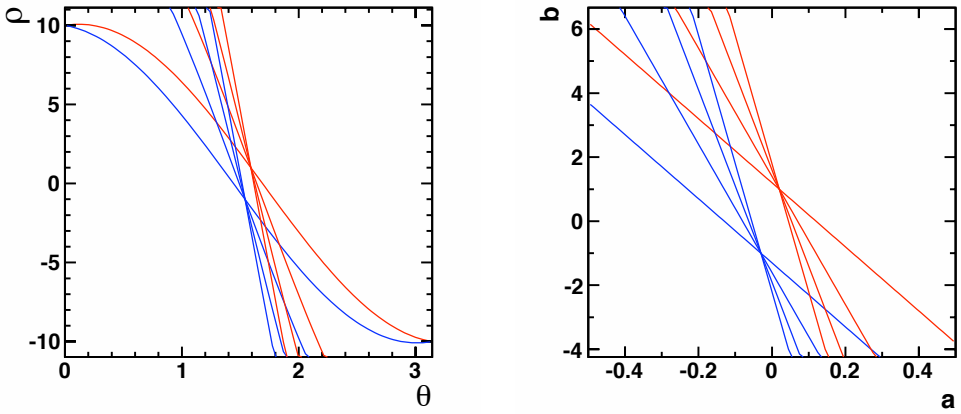

Figure 6.6.: Hough transform of the blue and red set of points shown in Figure 6.5. The parametrization of the feature space is represented in polar coordinates (left panel) and in Cartesian coordinates (right panel).

All detectors provide a hit of particles within a certain resolution. The inaccuracies imply that in the feature space the curves corresponding to a hit of a same track are not crossing

at a unique intersection point. When all of those curves are close enough to each other nearby the expected point, this area still corresponds to a close estimation of the track parameters. The feature space can be binned as in histograms to simplify the search of the areas that represent the intersection points. All curves are accumulated in the binned feature space, and the track candidates can be found by looking for local maxima of the accumulated density. The size of the bin is important to allow curves associated to a same track to be concentrated to a unique bin nearby the expected intersection point of the parameters of the track. This procedure is called the Hough Transform.

If resolutions of detectors largely differ from each other, it is also possible to include the affection of the resolution discrepancies in the feature space. Instead of building a curve from a hit, the curve can be set to have a specific width. This technique is the Fuzzy Radon Transform [94]. Figure 6.7 shows the resulting surfaces from the initial curves in the feature space for Cartesian parameters that are plotted in the right panel of Figure 6.6.

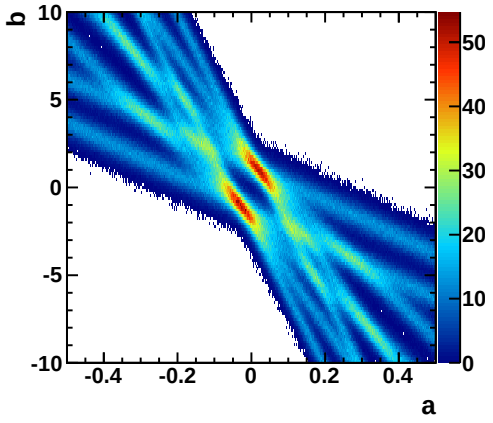

Figure 6.7.: Fuzzy Radon transform similar to the feature space of the Cartesian parametrization plotted in the right panel of Figure 6.6.

With this method, local maxima have to be found within a window of several bins to take the width of those surfaces into account. In order to optimize the procedure to find the local maxima, one can use a pre-tracking which provides some track segments. These segments give a rough estimation of possible track parameters. In the feature space, track segments are equivalent to a single point corresponding to the known track parameters of the segment. The prior knowledge allows to focus the search for local maxima to a restrictive area in the parameter space [95].

A pre-tracking procedure is necessary in the case of the phase 0 experiment, especially in front of the dipole magnet with the fiber detector sets and the drift chamber. This is because each fiber detector station independently measures the x- and y-position of incoming particles.

Pre-tracking

An algorithm dedicated to the tracking between the fiber detectors for the secondary vertex trigger has been already discussed in Chapter 5. While this method is suitable in case of a hardware implementation, it costs much more computer time in the offline analysis. The implementation of the secondary vertex trigger is done by means of FPGA chips which are known for their strong parallelism ability. Using a CPU is extremely difficult to obtain the same parallelism paradigm in an analysis code.

A first naïve pre-tracking routine has then been used. Thanks to the drift chamber BDC between TR1 and TR2, a combinatorial track following method gives a preliminary group of track segments. Each segment has to be validated by several geometrical acceptance cuts.

Another idea for the pre-tracking is to employ projective space of the tracks to handle a 3D perspective view of each of them. From a one-point perspective, it is possible to accumulate, like in the Hough transform, all the fired wires and fibers into a virtual XY-plane. Each fired tube (wire or fiber) in 3D can be projected via its *homogeneous* coordinates into a fixed virtual XY-plane.

Figure 6.8 shows an example in which a track (dashed brown line) hits three detection planes and fires three different tubes (wire or fiber). Each of these tubes is projected through a perspective projection from the decided viewpoint (O_1 or O_2 in Figure 6.8). If the viewpoint is close to the track of interest, all fired tubes intersects in one point (top panel), otherwise the projection of fired tubes makes a triangle on the virtual plane. By looking for those intersections in the virtual plane, all fired tubes from one track can be brought together to build track candidates. The track parameters can then be estimated by fitting all the sets of 1D-hits with a 3D line. The projective plane can be segmented in a similar manner of the Hough Transform to take into account the resolution and the width of wire and fiber hit clusters.

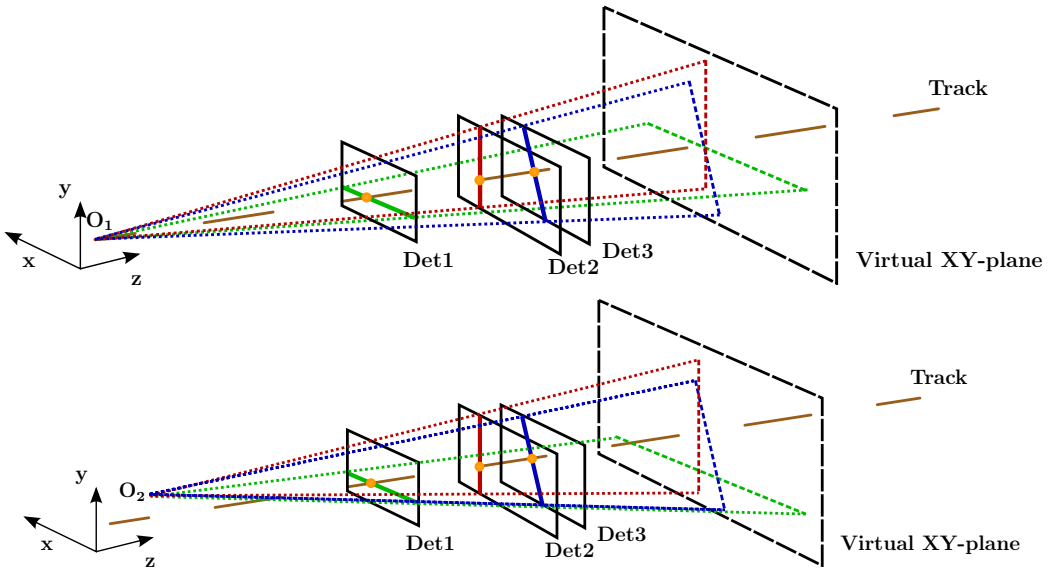

Figure 6.8.: 3D perspective view of a track (dashed brown line) and its hits on the three detector planes (Det1, Det2, Det3). Fired wires/fibers in each detection plane are shown in green, red and blue color. The perspective projection on the virtual plane (dashed plane) is shown for all fired wires and fibers from the viewpoint O_1 (top panel) or O_2 (bottom panel). In the top panel, O_1 is aligned with all the hits of the drawn tracks, while, in the bottom panel O_2 is not aligned.

The procedure is to define several viewpoints and to look for local maxima in the virtual XY-plane placed right behind the last fiber detector. Each time a set of 1D-hits is validated, the corresponding wires or fibers are removed for the next step. The procedure ends when a track cannot be built with the remaining wires or fibers.

This method allows to avoid any combination of independent layers to build track segments. The pre-tracking procedure in front of the magnet is a useful method of the complete track finding procedure because it reduces the density in the Hough transform procedure and helps to focus on a specific area in the feature space.

Track finding and efficiency

In front of the dipole magnet the multiplicity of each detector layer varies from 5 to 12 particles depending on the type of events. The pre-tracking allows to reduce the amount of fake tracks in the upstream part of the setup. The hit multiplicity on detectors behind the ALADiN magnet is decreased since particles without a large enough initial momentum do not reach the exit of the magnet. In average, the second drift chamber SDC has a

hit miltiplicity of around 2 to 5 while the TOF wall for π^- detection has only 1 hit per hypernuclear event, and the TOF+ wall has around 1 to 3 hits.

The Hough transform permits to associate, for each hit in the TOF walls, hits from SDC and the track segment from upstream. Track candidates are formed by finding local maxima on the density in the feature space. The subroutine to find a local maximum is optimized to look for a maximum around the area corresponding to a track segment. A linear fit is done in the yz-plane, since the magnetic field is only along the y-direction, in order to reject any fake track which does not satisfy a loose χ^2 cut. This χ^2 cut does not tightly discriminate fake candidates since the vertical resolution of the TOF walls is too poor for any strong rejection.

This track finding procedure has been tested with a cocktail of particles as input events in the MC simulations. The particle multiplicity was similar to the expected multiplicity of each detector to evaluate its efficiency as a function of the momentum of each particle. The efficiency is determined by comparing found track candidates across the setup to real tracks which have been simulated. A track which has all its associated hits corresponding to the ones of a real track is considered as a good track candidate, otherwise those candidates are reckoned as fake tracks.

The track finding efficiency has been estimated to be around 95% in a wide range of particle momenta. In addition to the found good candidates, a maximum of 10% of fake tracks is also selected as track candidates. This amount of fake tracks is reasonably acceptable since the track multiplicity per event is not critical for the fit procedure which has stronger criteria of selection and rejection.

6.2.6. Track fitting by the Kalman filter

After the track finding processed by the Hough transform, tracks are fitted based on the Kalman filter.

Kalman Filter method

The Kalman filter is a recursive estimator used in several domains to estimate the state of a dynamic system from successive noisy or incomplete measurements [96]. This method has been applied to the track fitting in high-energy physics [97].

This technique has to be opposed to the global fit methods, in which all measured hits of a track candidate are treated at the same time. The Kalman filter starts with a first approximation of the $\mathbf{r}_0$ state and improves the state vector $\mathbf{r}$ (introduced in Section 6.2.2) by adding successively measured hits. The best estimation of $\mathbf{r}$ is reached when the last measurement is added.

The step to include a new measurement $\mathbf{m}_k$ from the previous added measured hit $\mathbf{m}_{k-1}$ consists of three distinct parts:

- Firstly, the next temporary track state $\mathbf{r}_k^{k-1}$ is *predicted* from the current state $\mathbf{r}_{k-1}$ to the place of the new measurement to be added . In this step, the track propagation, explained in Section 6.2.2, is used to extrapolate a prediction from the current state $\mathbf{r}_{k-1}$. The prediction of the state vector and its covariance matrix C_k^{k-1} can be written as in Eq. 6.16.

$$\begin{aligned} \mathbf{r}_k^{k-1} &= f(\mathbf{r}_{k-1}) \\ C_k^{k-1} &= J_k \, C_{k-1} \, J_k^T \end{aligned} \tag{6.16}$$

- In the next step, a process noise term Q_k is added to the predicted covariance matrix C_k^{k-1} in order to describe probabilistic deviations of the state vector.

$$\begin{aligned} \hat{\mathbf{r}}_k^{k-1} &= f(\mathbf{r}_{k-1}) \\ \hat{C}_k^{k-1} &= C_k^{k-1} + Q_k \end{aligned} \tag{6.17}$$

- The last part is the filtering step in which the predicted state is updated with the new measurement $\mathbf{m}_k$ to obtain the optimal estimation of $\mathbf{r}_k$. To be able to compare the predicted state with the measurement, the predicted state has to be projected on the measurement space. If the detector layer provides only one coordinate, the measurement m_k is a scalar, while a planar detector measuring two coordinates gives a vector measurement. Thus, a projection matrix H_k is used corresponding to the type of measurement. The residual of the prediction is then denoted by $\mathbf{m}_k - H_k \, \hat{\mathbf{r}}_k^{k-1}$. A covariance matrix V_k is also associated to each measurement error of $\mathbf{m}_k$.

The filtering step is then expressed by the following equations:

$$K_k = \hat{C}_k^{k-1} H_k^T \left(V_k + H_k \hat{C}_k^{k-1} H_k^T\right)^{-1} \tag{6.18}$$

$$\mathbf{r}_k = \hat{\mathbf{r}}_k^{k-1} + K_k \left(\mathbf{m}_k - H_k \hat{\mathbf{r}}_k^{k-1}\right) \tag{6.19}$$

$$C_k = \hat{C}_k^{k-1} - K_k H_k \hat{C}_k^{k-1} \tag{6.20}$$

The χ^2 is also updated with the new residual between the measurement $\mathbf{m}_k$ and the filtered state $\mathbf{r}_k$:

$$\chi_k^2 = \chi_{k-1}^2 + \left(\mathbf{m}_k - H_k \mathbf{r}_k\right)^T \left(V_k - H_k C_k H_k^T\right)^{-1} \left(\mathbf{m}_k - H_k \mathbf{r}_k\right) \tag{6.21}$$

Figure 6.9 illustrates the procedure when the measurements $\mathbf{m}_k$ and $\mathbf{m}_{k+1}$ are successively added. From the state $\mathbf{r}_{k-1}$ to the predicted state $\mathbf{r}_k^{k-1}$, the effect of the material layer on the trajectory increases the predicted error on the state $\mathbf{r}_k^{k-1}$ by including the matrix Q_k. The measurement $\mathbf{m}_k$ corrects the prediction during the filter step to obtain the filtered state $\mathbf{r}_k$.

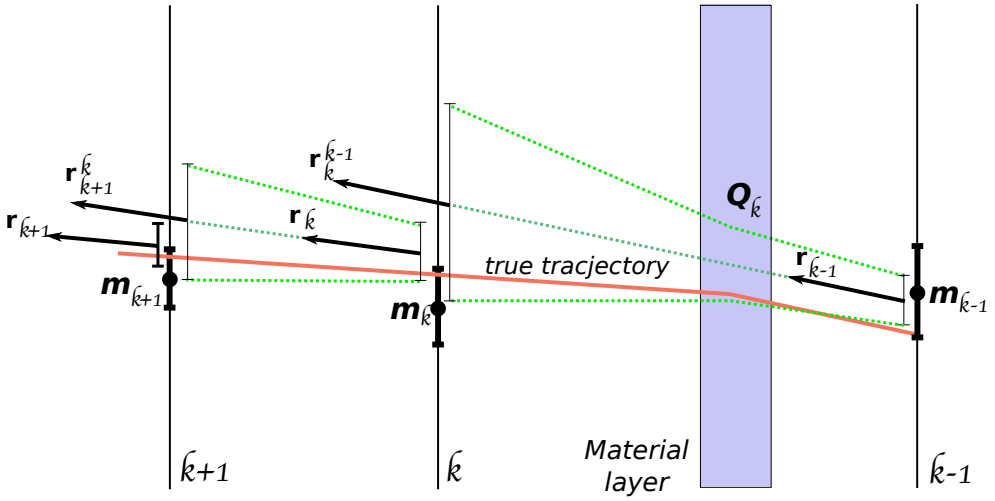

Figure 6.9.: Kalman Filter procedure from a state $\mathbf{r}_{k-1}$ to $\mathbf{r}_{k+1}$. The material layer leads to larger predicted errors on the estimated state $\mathbf{r}_k^{k-1}$. After the filtering step the filtered state r_k is the correction of $\mathbf{r}_k^{k-1}$ by the measurement $\mathbf{m}_k$.

Once the Kalman Filter has added all available measurements, the last one provides the best estimation of the state vector $\mathbf{r}$. In order to have the best estimation on all other measurement stations, the *smoother equations* propagate backward this estimation to all

the other points:

$$A_k = C_k \, J_{k+1} \, (C^k_{k+1})^{-1} \tag{6.22}$$

$$\mathbf{r}^n_k = \mathbf{r}_k + A_k \, (\mathbf{r}^n_{k+1} - \mathbf{r}^k_{k+1}) \tag{6.23}$$

$$C^n_k = C_k - A_k \, (C^n_{k+1} - C^k_{k+1}) \, A^T_k \tag{6.24}$$

Implementation

Prior to the Kalman Filter, a first estimation of the state $\mathbf{r}$ is required to start the Kalman Filter procedure. In the current track fitting routine, the momentum vector is calculated approximately for each candidate by assuming that the magnetic field inside of the dipole magnet is constant. This assumption gives a first order estimation of the track parameters $\mathbf{r}$.

The method is based on the Kalman filter implementation for the PANDA project, so called GENFIT *Generic Toolkit for Track Reconstruction* [98]. However, it has been modified for the event reconstruction of the HypHI Phase 0 experiment.

One of the main modifications was to include the new propagation algorithm presented in Section A.1.2. The calculation of the path length of the trajectory during the track fitting had to be included as well. After each step of the Kalman filter, the cubic Hermite spline between the two filtered states $\mathbf{r_k}$ and $\mathbf{r_{k-1}}$ are calculated. Only the starting and ending points and their tangent vectors are needed to calculate the Hermite spline. The analytic formula of the spline is obtained by:

$$\mathbf{S}(t) = (2t^3 - 3t^2 + 1)\,\mathbf{x_{k-1}} + (-2t^3 + 3t^2)\,\mathbf{x_k} + (t^3 - 2t^2 + t)\,\mathbf{p_{k-1}} + (t^3 - t^2)\,\mathbf{p_k} \tag{6.25}$$

Where $\mathbf{x}$ and $\mathbf{p}$ denote the vector position and momentum. In this parametric form of the spline, the variable t is included in the unit interval $[0, 1]$. The integral of the path length s is computed with this polynomial formula of the spline:

$$s = \int_0^1 \sqrt{(S'_x)^2 + (S'_y)^2 + (S'_z)^2}\,\mathrm{d}t \tag{6.26}$$

Efficiency of the track fitting

The track fitting procedure using the Kalman filter has been tested first without the track finding routine to avoid any disturbance. A cocktail of particles has been used from a low to a high momentum range which should include the expected momentum range of particles produced during the Phase 0 experiment.

The residual of each track parameter has been evaluated to estimate the resulted resolution. The pull of each of them is calculated as well, which is the normalized residual by the variance of the interested parameters:

$$Pull_x = \frac{x_{rec} - x_{MonteCarlo}}{\sigma_x} \tag{6.27}$$

This random variable should follow a Gaussian distribution $N(0, 1)$ if the fitting procedure handles properly the errors and their propagation.

Table 6.2 summarizes the RMS values of pull distributions of the systematic study. All pull distributions have been fitted by a Gaussian distribution, providing a RMS value close to unity, except for the pull of the momentum estimation. Table 6.3 summarizes the RMS values of the residual distribution.

Table 6.2.: Pull of the track parameters after the fitting procedure.

q/p	x	y	t_x	t_y
1.16	1.04	1.08	1.02	1.09

Table 6.3.: Residual of the track parameters after the fitting procedure.

$\delta p/p_{(\%)}$	$x_{(\mu m)}$	$y_{(\mu m)}$	$t_{x_{(\times 10^{-3})}}$	$t_{y_{(\times 10^{-3})}}$
1.1	23	24	1.6	1.6

The efficiency of the Kalman Filter is evaluated if a track can be properly reconstructed with a good confidence level and gives the mass of the particle in a range of $\pm$ 5% of the expected mass. Figure 6.10 shows the efficiency of the Kalman filter for α-particles (top left), protons (bottom left), and π^- mesons (top right) with a confidence level of

95%. Thanks to the χ^2 test which determine the confidence level, the 10% of fake tracks in addition to proper track candidates are easily rejected down to 1% of full amount of tracks.

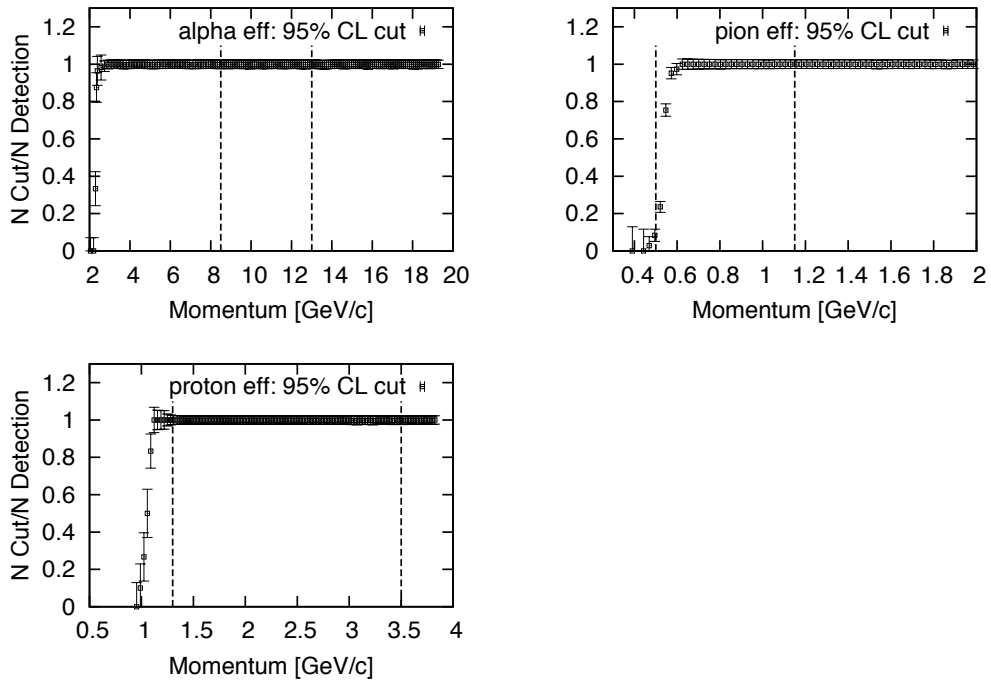

Figure 6.10.: Efficiency of track fitting by the Kalman filter for α-particles (top left), protons (bottom left), and π^- mesons (top right) with a confidence level (CL) of 95%. Vertical lines mark the boundary of interested momentum in the HypHI Phase 0 experiment.

The region of momentum of interest in the HypHI Phase 0 experiment for each particle is marked by the two vertical lines on each plot. Those intervals are inferred from the kinematics of the primary and secondary reaction simulated by the UrQMD model. Inside of this range a good efficiency larger than 95% is observed in each panel. For the slow π^-, however, the track reconstruction efficiency drops to 75%. The presented reconstruction efficiencies result from the systematic study which does not include dependency on physics processes. When the momentum distribution of produced and detectable particles is taken into account, reconstruction efficiency is even larger and especially for the case of π^- it reaches 85%.

Figure 6.11 shows an achieved momentum resolution $\delta p/p$ of 1% for all particles of interest. It shows that for the very slow particles the momentum resolution is instead close to 3%.

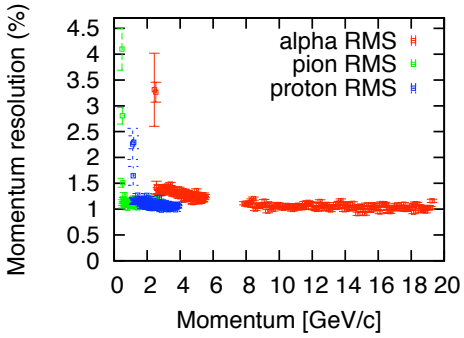

Figure 6.11.: Momentum resolution $\delta p/p$ as function of the momentum of the reconstructed track.

This value is still acceptable when the momentum distribution of detectable particle is considered.

6.2.7. Event reconstruction procedure and performance on simulated data

The first step of the event reconstruction procedure is to realize the track reconstruction. In each event, hit positions from all tracking stations are connected to each other as potential tracks using the Hough transform. In addition, a first estimation of the charge information is associated to each possible track from the charge identification obtained by the energy loss in the Time-of-Flight walls. For each submitted track, a calculation of the momentum is performed analytically, and is used as a seed for the Kalman filter algorithm.

The track fitting routine includes three iterations of the Kalman filter. The first iteration gives a first estimation of the path length of the particle trajectory. It gives a first estimation of the velocity β from the Time-of-Flight measurements. At this stage of the procedure, most of the fake tracks resulting from the track finding routine have been rejected because of their large χ^2 value (see Section 6.2.6).

This first approximation allows us to determine the particle identity. The two next iterations of the Kalman filter use the new information to perform a better evaluation of the multiple scattering effects and of the energy loss in the detector materials. A χ^2 test of the resulting momentum fit is used to select tracks within 95% CL (Confidence Level) as presented above. After this procedure, the final particle identification is completed

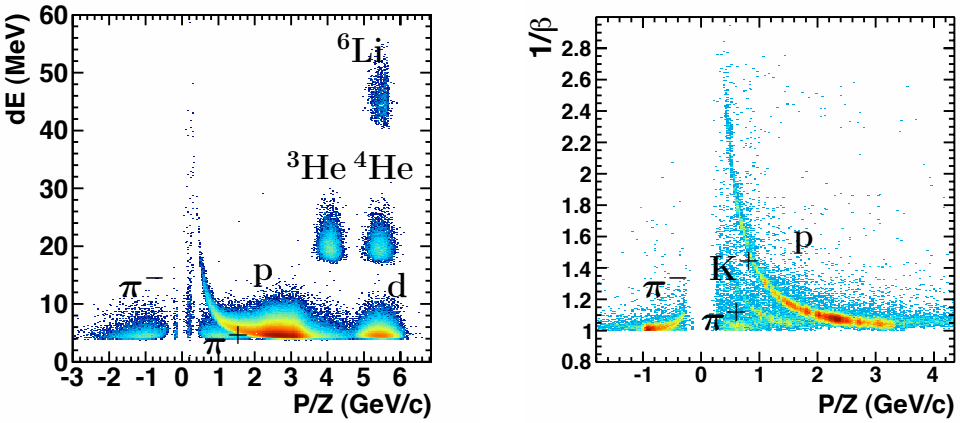

Figure 6.12.: Particle identification plots: Correlation between the energy deposit of charged particles in the TOF walls and the momentum-to-charge ratio p/Z (left panel) and the correlation velocity $1/\beta$ against p/Z (right panel) for the identification of lighter particles.

by the correlation plot of the energy deposit dE against the momentum-to-charge ratio p/Z as shown in Figure 6.12 (left panel). The correlation plot using the inverse of the velocity $1/\beta$ instead of the energy deposit is employed to achieve a better identification of light particles, as shown in Figure 6.12 (right panel). The Four-momentum **P** is thus determined for each track candidate which fulfills the χ^2 test. All results that will be presented are based on a track selection within 95% CL.

After the track reconstruction procedure, each track that originates from one of the mesonic decays of the hypernucleus of interest, ${}^{3}_{\Lambda}$H$\rightarrow \pi^- + {}^3$He, ${}^{4}_{\Lambda}$H$\rightarrow \pi^- + {}^4$He and ${}^{5}_{\Lambda}$He$\rightarrow \pi^- + {}^4$He$+p$, is selected. For each pair (π^-, ^{3}He or ^{4}He) or triplet (π^-, ^{4}He, p), decay particle candidates are extrapolated to a common vertex by the point of closest approach method. With this method, the positions at which two or more moving objects reach their closest possible distance are calculated.

Hypernuclear events can be discriminated from the signal of the primary vertices produced in the target by proper tight conditions, since the mean decay length of the produced hypernuclei is approximately 15 cm in the HypHI Phase 0 experiment. Indeed, by selecting the region of the reconstructed secondary vertex, the signal-to-background ratio can be improved. This condition on the secondary vertex is needed because the cross section for hypernuclear production is expected to be seven orders of magnitude smaller than the total reaction cross section. Primary reactions from the target are considered as a signal

which contributes to the combinatorial background during the hypernuclear reconstruction. Among these primary reactions, hypernuclei are characterized by their weak decay, which is considered as a secondary reaction.

The pair or triplet of tracks which has a relative distance smaller than 2 mm and has the point of closest distance placed 6 cm or more behind the center of the target is considered as a candidate of a hypernucleus.

With these procedures, simulated hypernuclear events of ${}^{3}_{\Lambda}$H, ${}^{4}_{\Lambda}$H and ${}^{5}_{\Lambda}$He were reconstructed by using the invariant mass method. The secondary vertex resolution for the reconstruction of the decay of the ${}^{3}_{\Lambda}$H, ${}^{4}_{\Lambda}$H and ${}^{5}_{\Lambda}$He hypernuclei has been also investigated. The resolutions obtained are summarized in Table 6.4. The vertex resolution has been improved in comparison to the former analysis method of the HypHI experiment [71].

Table 6.4.: Secondary decay vertex resolutions of ${}^{3}_{\Lambda}$H, ${}^{4}_{\Lambda}$H and ${}^{5}_{\Lambda}$He hypernuclei.

Species	x (mm)	y (mm)	z (mm)
${}^{4}_{\Lambda}$H	0.23	0.33	3.53
${}^{3}_{\Lambda}$H	0.22	0.35	3.61
${}^{5}_{\Lambda}$He	0.17	0.29	6.4

The combinatorial background contribution has to be simulated as well, and the background rejection capability has to be determined before any conclusion on the hypernuclear event reconstruction.

This background contribution arises from the calculation of the invariant mass of the pair or triplet of hypothetical daughter particles which do not come from any secondary vertex, and thus are not correlated. The total reaction cross section, which is about 1b, is seven orders of magnitude larger than the one of the hypernuclear production. This hypernuclei production cross section is expected to be of the order of 0.1 μb. Because of this large difference between these respective cross sections, it is technically difficult to naturally simulate the production reaction by assuming these orders of magnitude. Indeed, by simply running the UrQMD or GiBUU event generator with this difference of cross sections for one produced hypernuclear event, 10 millions of events should have been also produced. It is mainly impossible to carry out any event reconstruction performance study

in these conditions. Therefore, hypernuclear events have been produced independently to the total reaction cross section. The background production has been then achieved separately as well. The event reconstruction has been performed on each simulated data set, and the resulting invariant mass spectra have been scaled in order to represent the cross section difference and to obtain a proper comparison.

As explained in Chapter 3, the trigger design study has demonstrated that the background rejection of the trigger system is about 0.017% with a hypernucleus selectivity of 7% [99]. It means that the ratio of 1 hypernucleus every 10^7 collisions becomes 1 hypernuclear event every $2.4 \cdot 10^4$ recorded events. This background contribution has been modeled by 20 millions of events from the UrQMD event generator. Mainly, this background consists of events which do not involve any strangeness production. After the track reconstruction and the secondary vertex requested behind the target, any of these background signals have been visible in any invariant mass spectrum of hypernuclei. It shows that the requirement of a secondary vertex after the target has a critical power for the background rejection.

The most important background contribution in the case of the reconstruction of hydrogen Λ-hypernuclei is a recorded event in which a $Z = 2$ particle (He-like particle) and a free Λ are very close to each other. This kind of event is similar to a hydrogen hypernucleus event in which the proton from the free Λ decay is not observed. The combinatorial background corresponds then to the miss-reconstruction of a hydrogen hypernuclei by considering the pair formed by a Z=2 particle and the π^- of the free Λ decay.

For this reason, prior to any hypernuclear reconstruction, the invariant mass reconstruction from a π^- meson and proton is performed, and the π^- and proton tracks reproducing the free Λ mass are rejected in order to suppress the background due to the free Λ production. A second criterion is also used when the track of a proton has not been properly found and identified. These background events can be distinguished by the energy deposit information in TR0. The background event registers an energy deposit which corresponds to a $Z = 2$ charge in the TR0 layer, while the hydrogen hypernuclei passing through the TR0 detector induces a signal corresponding to a charge $Z = 1$ [99]. The measured energy resolution of 20% in TR0 is sufficient to distinguish $Z = 1$ signals from $Z = 2$ [77]. A cut condition has been applied in the reconstruction procedure by requiring the energy deposit in TR0 to be less than 5.5 MeV in the case of the reconstruction of ${}^{3}_{\Lambda}\mathrm{H}$, and ${}^{4}_{\Lambda}\mathrm{H}$ hypernuclei. The ${}^{5}_{\Lambda}\mathrm{He}$ hypernucleus does not suffer from this background contribution

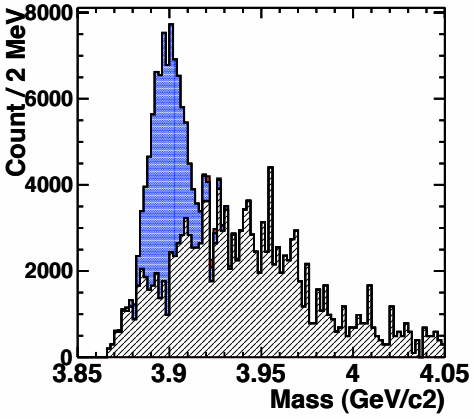

Figure 6.13.: Invariant mass spectrum of simulated ${}^{4}_{\Lambda}$H after the trigger decision. No cut condition is applied. The combinatorial background consists of the two background sources as discussed in the text. The background from the primary vertices is plotted in hashed black, while the background from the free Λ contribution is in dotted blue. The hypernucleus signal is plotted in red but it is almost invisible.

since the secondary vertex reconstruction of a three body decay requires a tighter vertex cut which efficiently rejects this background.

The combinatorial background contribution of recorded events with Z=2 particles and a free Λ-hyperon have been represented by 815000 UrQMD events during the background rejection study.

The invariant mass distributions of the hypernucleus of interest, shown later on, have been obtained by means of 20000 hypernuclear events produced by the UrQMD event generator. These hypernuclear events include the hypernucleus of interest, and the particles and fragments produced as well during the calculation of the event generator. For the formation of hypernuclei in the event generator, the probability to coalesce in a projectile fragment (coalescence factor) is assumed to be 0.01, which is a similar condition to the one used in Ref. [99]. The latter value is consistent with the one deduced by the STAR experiment with a similar momentum range for produced hypernuclei [75].

Figure 6.13 shows the invariant mass spectrum of ${}^{4}_{\Lambda}$H from combinatorial background and the hypernucleus signal. Each invariant mass spectrum of the two combinatorial background contributions, explained above, and of the hypernuclear events have been scaled to each others in order to reproduce the cross section differences. No cut condition has been applied to obtain this spectrum. It shows that the hypernuclear signal is not visible

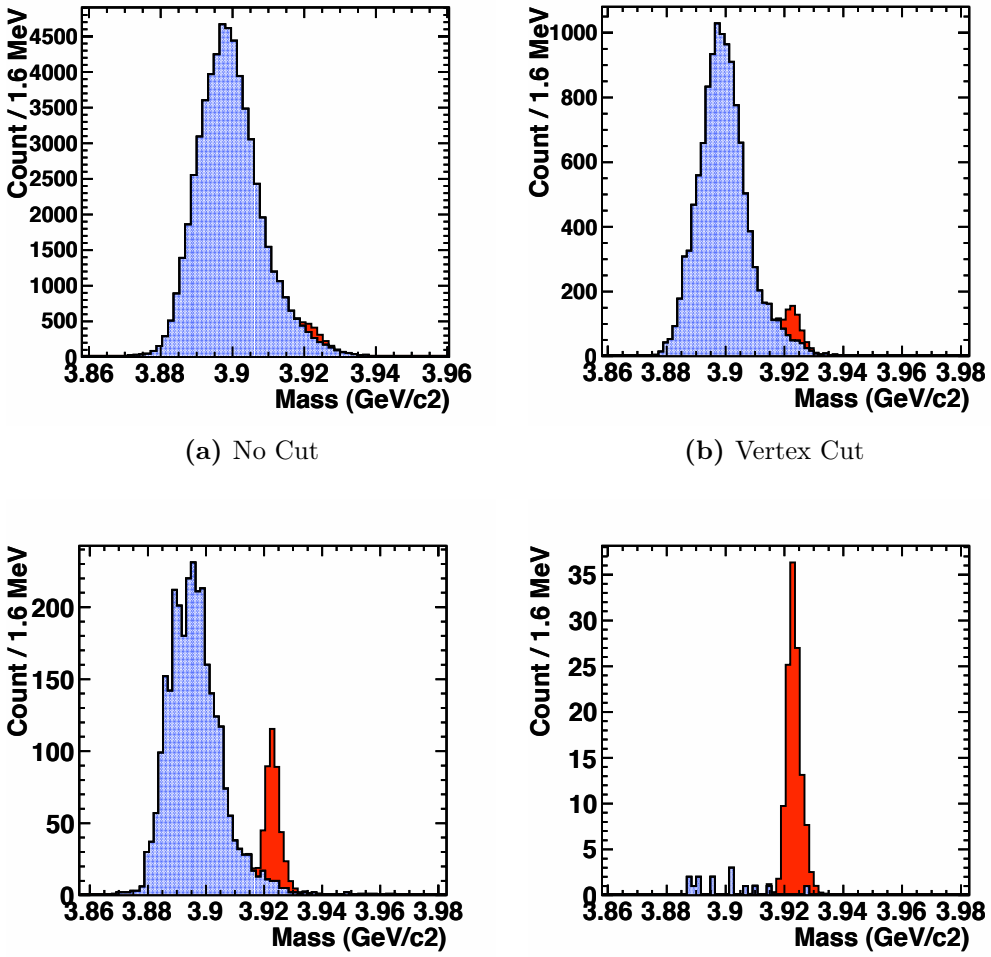

(a) No Cut

(b) Vertex Cut

(c) Vertex and Λ Cut

(d) Vertex, Λ, and TR0 energy Cut

Figure 6.14.: Illustration of the series of applied cuts. Adding a new cut improves the signal-to-background ratio in the invariant mass spectrum of simulated ${}^{4}_{\Lambda}\mathrm{H}$

without cut condition (in red in the figure). The histogram in hashed black corresponds to the primary vertices. The second histogram in dotted blue stands for the contributions of the miss-reconstruction of a α-particle and the π^- of the free Λ decay. As it was presented above, the combinatorial background from the primary vertices is discriminated by rejecting any vertex placed before 6 cm from the target. The following invariant mass spectra of Figure 6.14 do not include this contribution since this simple cut is sufficient.

Figure 6.14 shows the invariant mass spectra of ${}^{4}_{\Lambda}\mathrm{H}$ obtained by a sequence of applied cuts. Only the second source of the combinatorial backgrounds, explained above, is considered in order to illustrate the power of the background reduction after each cut condition.

Figure 6.14a is the invariant mass spectrum without any cut condition. The hypernuclear signal is very small compared to the background. With the secondary vertex cut defined above, hypernucleus signal becomes visible in Figure 6.14b. By applying an additional cut condition to reject track candidates which correspond to a free Λ particle, the peak of the hypernucleus is more pronounced, as shown in Figure 6.14c. With the rejection of candidates fulfilling the energy cut on TR0, the hypernucleus peak is dominant in the invariant mass spectrum shown in Figure 6.14d.

Table 6.5 summarizes the signal-to-background ratio of each invariant mass spectrum of the Figure 6.14. It shows that a cut condition which requests a secondary vertex after the TR0 layer and which rejects secondary vertex candidates of Λ hyperon gives already a good peak-to-background ratio of 3.2. Including, in addition, the energy deposit cut on the TR0 layer reduces almost completely the background contribution.

Table 6.5.: Signal-to-background ratio of the each invariant mass distribution, shown in Figure 6.13 and Figure 6.14, after applying cut conditions. B and S stands for, respectively, the integral of background and the hypernuclear signal around the peak position. S/B corresponds to the signal-to-background, or peak-to-background ratio.

	After trigger selection	Full Background	Vertex Cut	Vertex & Λ Cut	Vertex, Λ, and TR0 energy Cut
B	$2.4 \cdot 10^4$	35843	652	115	1
S	1	523	373	369	124
S/B	$0.41 \cdot 10^{-4}$	0.152	0.572	3.209	124

By applying all the procedures discussed above, ${}^{3}_{\Lambda}$H, ${}^{4}_{\Lambda}$H and ${}^{5}_{\Lambda}$He hypernuclei were reconstructed by calculating the invariant mass of π^-+^{3}He, π^-+^{4}He and π^-+^{4}He+p channels, respectively. Distributions of the reconstructed invariant mass of ${}^{3}_{\Lambda}$H, ${}^{4}_{\Lambda}$H and ${}^{5}_{\Lambda}$He are shown in Figure 6.15. These invariant mass distributions have been produced with a different set of cut conditions which explain the difference between Figure 6.15 and Figure 6.14.

The values of the widths, expressed in terms of standard deviation, for the invariant mass distributions are 2.23, 2.07 and 2.09 MeV for ${}^{3}_{\Lambda}$H, ${}^{4}_{\Lambda}$H and ${}^{5}_{\Lambda}$He, respectively. In

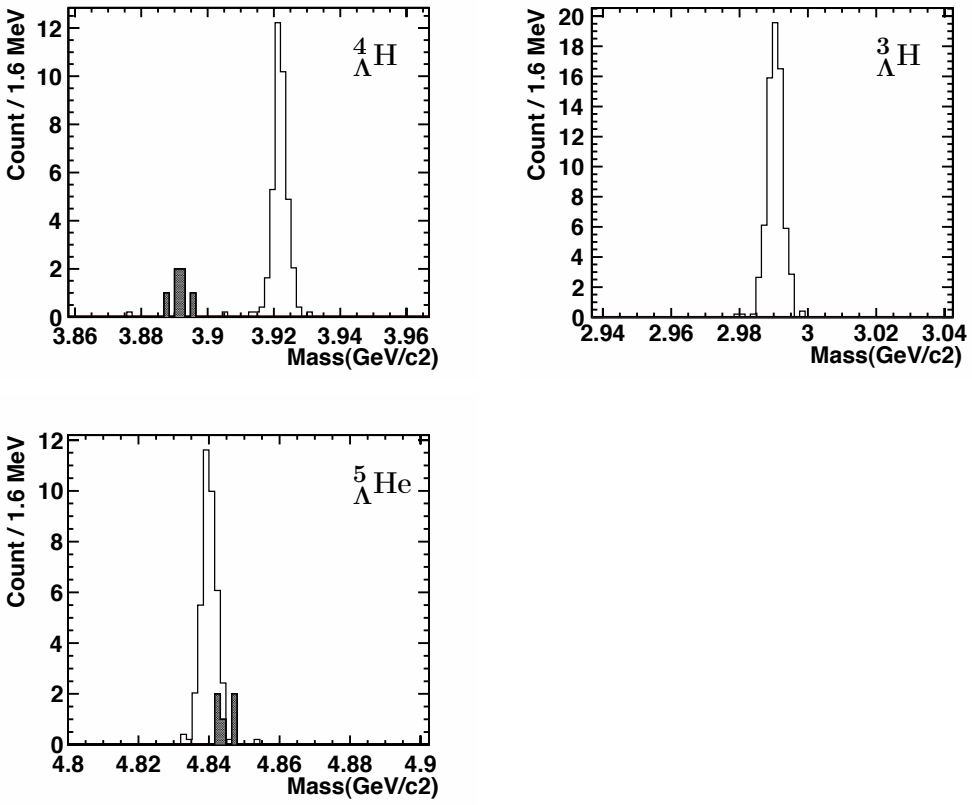

Figure 6.15.: Invariant mass spectra of simulated $^{4}_{\Lambda}$H (top left), $^{3}_{\Lambda}$H (top right) and $^{5}_{\Lambda}$He (bottom left). See text for more details.

Figure 6.15, the contributions from the background are separately shown in hashed black, and an excellent signal-to-background ratio is observed.

Table 6.6.: Expected rates for reconstructed hypernuclei per week in Phase 0 experiment in the condition for a ^{6}Li beam intensity of 10^{7} particles per second.

Species	Expected cross section (μb)	event/week
$^{3}_{\Lambda}$H	0.1	7.8×10^{3}
$^{4}_{\Lambda}$H	0.1	7.2×10^{3}
$^{5}_{\Lambda}$He	0.5	18.2×10^{3}

The expected rates for reconstructed hypernuclei discussed in the original proposal of the Phase 0 experiment [99] have been revised with this new reconstruction procedure. Rates deduced by the present work are summarized in Table 6.6 with values of expected

cross sections. It has been shown that the expected reconstructed rates are increased in comparison to the values shown in the proposal. This work succeeds to provide more analyzing power for the reconstruction for the Phase 0 experiment.

7

Preliminary results from the data analysis of the Phase 0 experiment

In this chapter, the first results from a preliminary analysis of the Phase 0 experiment are presented. The data analysis is performed by a simplified version of the reconstruction software described in the previous chapter. This pre-reconstruction procedure with a simplified method based on geometrical tracking is presented at first. This simpler reconstruction was used to check the performances of the full apparatus, whose configuration has been described in Chapter 4. The obtained energy deposit distribution in the fiber detector TR0 is shown since it is an important information for the event reconstruction. The particle identification obtained with this simplified version is then shown, which allows to perform the reconstruction of Λ hyperon candidates. The first invariant mass spectrum of Λ particle and its lifetime measurement are presented. Finally the first result of reconstruction with the full event reconstruction procedure of Chapter 7 is shown. The first estimations of the invariant mass distribution of ${}^{5}_{\Lambda}\mathrm{He}$ and its lifetime measurement are given.

7.1. Preliminary results

7.1.1. Simplified reconstruction procedure

The pre-reconstruction consists of algorithms to find track candidates by iterating all the fired channels of the fiber detectors. This pre-tracking by considering every combination

has been mentioned in Chapter 6 as a naïve track finding method [92]. Hits from the TOF+ wall and the TFW wall are associated to those track segments from the pre-tracking in the fiber stations via a linear fit for a straight track in the vertical direction. This linear fit is relevant because the magnetic field is parallel to the vertical direction. Once the track candidates are built, the momentum is calculated analytically by assuming a box-like field map for the magnetic field. Then, the momentum is adjusted to take the asymmetry of the magnetic field into account. This simplified procedure has been used in Ref. [99]. It is the first analysis procedure written before the full event reconstruction presented in Chapter 6. The power of rejection of fake tracks is not optimum. However, the pre-reconstruction procedure is fast enough to allow multiple runs and feedback to the analysis tuning, which will be used later for the full event reconstruction.

7.1.2. Energy deposit distribution of the TR0 fiber detector

The performances of the TOF system (see Chapter 4) are important for the full particle identification. Furthermore, for the full event reconstruction, the energy deposit measurement in the fiber detector TR0 is crucial, as it was illustrated by the reconstruction of simulated data in Chapter 6. In the MC simulations, an energy resolution of TR0 detector was used with a similar value to the measured resolution. As discussed in Chapter 6, a cut condition on the energy deposit in the TR0 layer is foreseen to have a significant impact on the background suppression. Thus, the experimental energy resolution of TR0 is reviewed in this section to start the discussion on the preliminary experimental results.

After applying the hit clustering procedure to the data from the fiber detectors, the energy deposit of each hit cluster is extracted. The energy measurement for each hit cluster is performed as the sum of the calibrated energy deposit measurement within the hit set of interest. The calibration of the energy deposit in each fiber channel is achieved by calculating the gain to apply to each channel in order to align each energy deposit measurement of Z=1 particles. The energy deposit obtained in the TR0 layer is shown in Figure 7.1. The particle identification has been provided by the track reconstruction along the rest of the setup. The measured energy deposit is associated to each track which has a corresponding hit cluster in the TR0 detector. Figure 7.1 shows a distinct separation between the two energy distributions corresponding to Z=1 and Z=2 particles. The achieved energy resolutions ($\Delta E/E$) are 81% and 27% for, respectively, Z=1 and Z=2 particles. Thus, an energy deposit cut condition between 100 to 900 channels is

sufficient to discriminate the Z=2 particles passing through the TR0 detector, which is a useful information for the full event reconstruction.

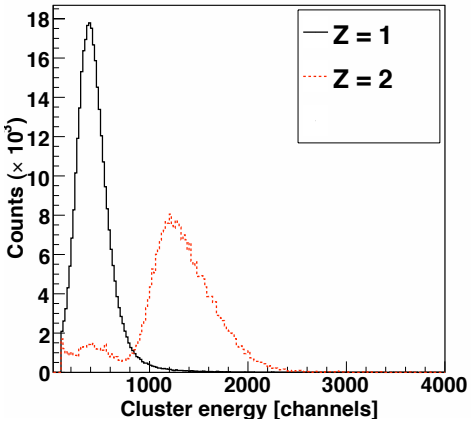

Figure 7.1.: The energy deposit distributions in the TR0 detector for Z=1 and Z=2 particles.

The calibration of the detectors have involved several steps. First of all, the position of each detector have been corrected from a laser measurement with a 100 μm accuracy. All the mis-alignments of the tracker detectors (ie. fiber detectors and drift chambers) were then known and adjusted to obtain a precise hit position. The time and energy deposit measurements from PMTs of the Time-of-Flight walls were calibrated as well. The walk correction of each PMT has been applied. The achieved resolution after correction for the TOF+ wall has been presented in Chapter 4.

7.1.3. Particle identification

After the detector calibration, the pre-reconstruction, described above, was performed in order to check the calibration and the performances of the detectors. The data analysis of the Phase 0 experiment is currently at the pre-reconstruction stage. This pre-reconstruction stage has a poorer selective power of the tracks in comparison to the full reconstruction. Thus tighter cut conditions in the track finding procedure have been applied in order to select cleaner events from the full data set.

With this simplified track reconstruction, the particle identification (PID) has been performed by combining the momentum, the energy deposit and the Time-of-Flight of the measured particles, as shown in Figure 6.12. The separation of each kind of particles

is expected to be poorer than the one in the full reconstruction. However, the current PID procedure still provides a reasonable charge and mass separation for the simplified analysis of the data.

Figure 7.2 shows, in the left panel, a correlation plot between the momentum-to-charge ratio p/Z and the energy deposit in the TOF+ wall. A reasonably clear separation among hydrogen isotopes can be observed. The separation for the helium isotopes is also observed though the statistics is rather poor. A correlation between the inverse velocity $1/\beta$ and the momentum-to-charge ratio P/Z is shown in the right panel of Figure 7.2. The expected correlations corresponding to the function $1/\beta = \sqrt{((m/p)^2 + 1)}$ are also shown in this figure for each particle type. The observed correlation reveals a reasonably clear separation between K^+, protons and deuterons, as shown in the figure. With the full event reconstruction procedure, it is expected to achieve a much clearer PID, as discussed in Chapter 6.

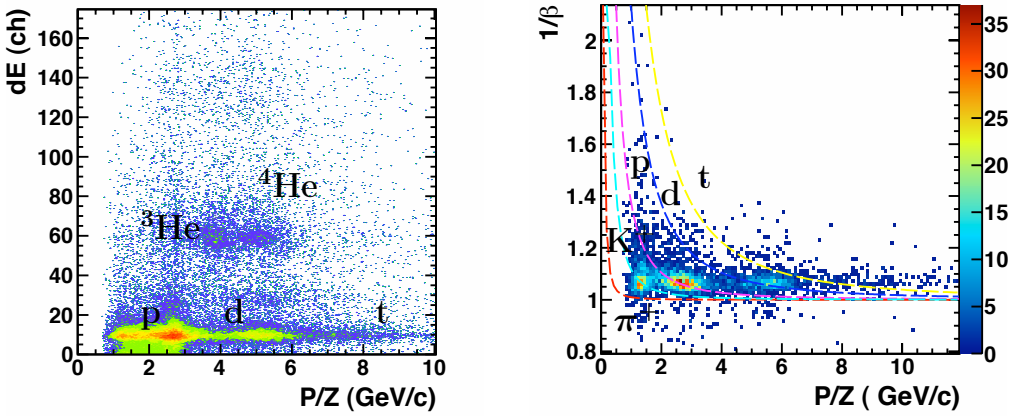

Figure 7.2.: Correlation plots used for PID are shown. The left panel shows the correlation between the energy deposit of positively charged particles in the TOF+ wall and the momentum-to-charge ratio p/Z. Energy deposit, dE, is expressed in channels. The right panel shows the correlation of the inverse velocity $1/\beta$ against p/Z for the identification of lighter particles (K^+, p, d, t). The correlation between $1/\beta$ and p/Z follows the function $1/\beta = \sqrt{((m/p)^2 + 1)}$, which is drawn for each light particle of interest.

7.1.4. Invariant mass spectrum and lifetime measurement of Λ-hyperon

With the achieved PID, the invariant mass of the Λ-hyperon has been reconstructed with the simple geometrical reconstruction method, described above. Very tight cut conditions in the track finding procedure have been applied in order to perform a descent secondary vertex reconstruction. Tracks candidates for π^- and protons are selected, respectively, with the TFW detector and the TOF+ wall based on the correlation between $1/\beta$ and p/Z. In the present analysis, a relative distance between the π^- and proton tracks smaller than 2 mm in the decay volume between the TR0 and TR1 detectors has been required. Those selected pairs of tracks should thus correspond to the secondary vertex candidates. Calculations of the invariant mass of the system π^-+p have been performed with those selected tracks. For each recorded event in the data set, only the best candidate, in the fitting procedure, has been considered as a Λ-hyperon candidate.

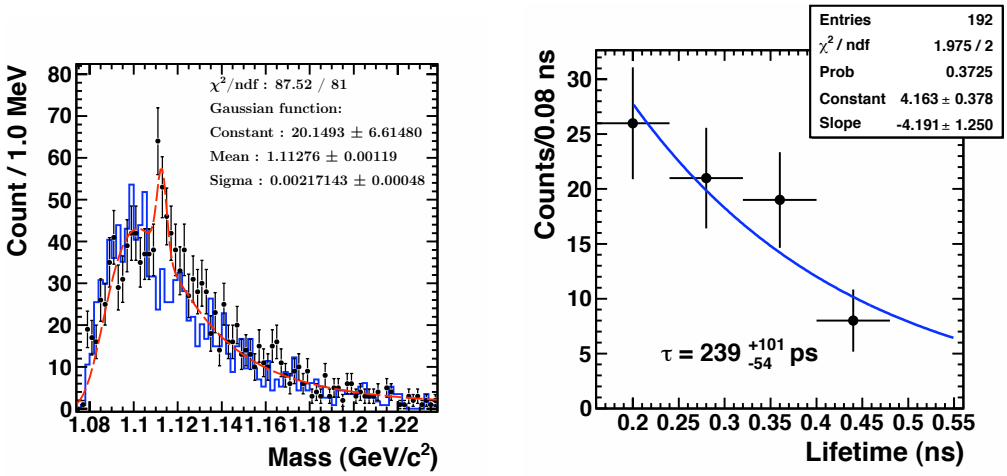

Figure 7.3.: The invariant mass distribution of Λ candidates (left panel) obtained by the simplified analysis procedure described in the text. The black points represent the analyzed data, and the histogram in blue corresponds to the mixed event analysis for the evaluation of the background contribution. The peak at 1.113 GeV/c^2 corresponds to the reconstructed Λ-hyperons. The measured distribution is fitted by a combination of a 5^{th} order polynomial function and a Gaussian distribution. The lifetime distribution of selected Λ candidates is shown in the right panel with an exponential fitting function.

The left panel of Figure 7.3 shows the reconstructed invariant mass distribution of the (π^-, proton) pairs. The black points represent the full obtained spectrum, while the

blue histogram corresponds to the invariant mass obtained using a mixed event analysis. The mixed event analysis consists in reconstructing a hypothetical invariant mass of the (π^-, proton) pairs, in which the π^- track is coming from a given event and the proton track from another event. The resulting invariant mass spectrum corresponds only to a combinatorial background since both hypothetical daughter particles are not correlated.

In the figure, a clear enhanced peak around 1.113 GeV/c^2 is observed, which corresponds to the Λ-hyperon. A fit of the background and the Λ-signal has been performed as represented by the dashed red line in the figure. The Gaussian distribution corresponding to the Λ peak has a mean value of 1.1128 ± 0.00119 GeV/c^2 and a width of 2.2 ± 0.5 MeV/c^2. The background signal has been estimated by the fitting function and by the mixed event analysis. The significance of the mass peak of the Λ-hyperon is deduced to be 4.2 σ. The estimation of the significance is obtained by the common formula : $S/\sqrt{(S+B)}$, in which S stands for the number of Λ candidates in the peak and $(S+B)$ the full integral of the peak and background in the range of interest. Stronger methods to evaluate the significance exist [100, 101, 102], however for preliminary results on the invariant mass spectrum of the Λ-hyperon, this first method is sufficient.

Since the secondary vertex position has been calculated for each Λ particle candidate, it is possible to give a first estimation of its lifetime. The right panel of Figure 7.3 shows the obtained decay time of the Λ candidates around the peak at 1.113 GeV/c^2. These candidates have been selected by the invariant mass calculation with a background subtraction. The distribution has been fitted by a simple exponential function, and a mean lifetime of $239\ ^{+101}_{-54}$ ps was deduced. The value is, within the errors, in agreement with the known value of the Λ-hyperon lifetime of 263 ± 2 ps [103]. Those first results about the reconstruction of the Λ particles indicate that the recorded events include secondary vertices of Λ particles. This indication reveals that the trigger system has selected potential secondary vertex candidates thanks to the vertex trigger.

The deviation of the observed mass from the known values of 1.115 GeV/c^2 could originate from the methods used in the simplified pre-reconstruction procedure.Better results are expected with the full event reconstruction, which involves a better signal-to-background ratio. The significance will also be improved with the analysis of larger number of events since only 1% of the recorded data have been analyzed to obtain those first results.

7.1.5. Invariant mass spectrum and lifetime measurement of $^{5}_{\Lambda}$He

The first trial of the full event reconstruction focused on the reconstruction of the $^{5}_{\Lambda}$He hypernuclei since less cut conditions are required to obtain a visible signal. Indeed, the reconstruction of $^{5}_{\Lambda}$He hypernuclei does not require any energy deposit cut in the TR0 detector. In addition, requiring a secondary vertex of three daughter particles gives more power to reject possible spurious candidates. The left panel of Figure 7.4 shows the achieved invariant mass distribution corresponding to $^{5}_{\Lambda}$He hypernuclei candidates. The distribution results from the reconstruction of selected (π^-, protons and α) track triplets. A mixed event analysis has not been performed yet. Instead, a simple fit combining a constant and a Gaussian function has been used to evaluate the peak position of the invariant mass distribution. A mean value of 4.8394 ± 0.0001 GeV/c^2 has been deduced with a width of 3.1 ± 0.6 MeV/c^2. The measured mass is consistent with the known value of 4.8399 GeV/c^2 for the $^{5}_{\Lambda}$He hypernuclei [104]. The significance of the peak is evaluated to 5.6 σ.

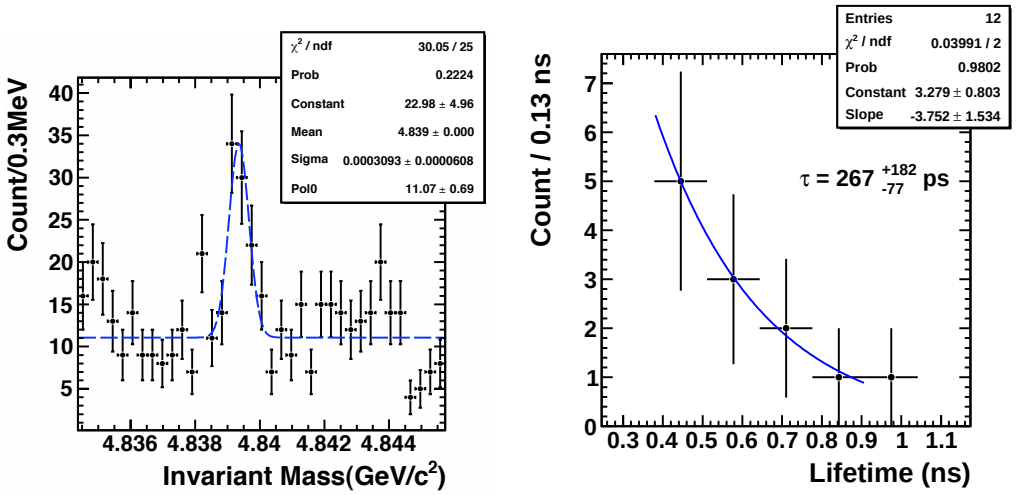

Figure 7.4.: Invariant mass distribution for the reconstruction of $^{5}_{\Lambda}$He hypernucleus (left panel) and its associated lifetime distribution (right panel). A fitting function of the invariant mass distribution is shown. The mean value of the Gaussian distribution is 4.8394 ± 0.0001 GeV/c^2.

The analysis of the lifetime of the reconstructed $^{5}_{\Lambda}$He hypernuclei has also been performed. In order to reject all the background signal and obtain a very clean mass spectrum, tighter cut conditions have been applied to select $^{5}_{\Lambda}$He hypernuclei candidates. Only 12 candidates have been selected under these conditions. The resulting decay time distribution is shown

in the right panel of Figure 7.4. Using the same procedure for the Λ-particles, a fit of the lifetime distribution gives a mean lifetime of 267 $^{+182}_{-77}$ ps. The resulting lifetime value has a large error because of the small number of candidates. The deduced value are in good agreement with the previous known values [105, 106, 107, 108, 109, 110], as shown in Figure 7.5.

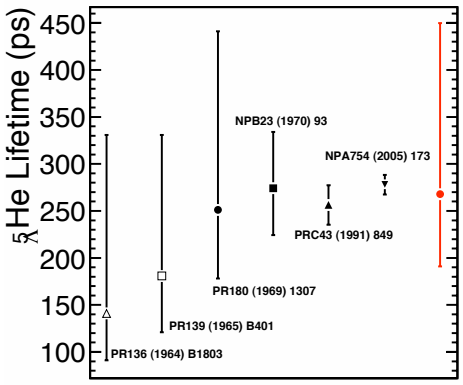

Figure 7.5.: World data for lifetime measurements of $^{5}_{\Lambda}$He. The data points are from [105, 106, 107, 108, 109, 110]. The resulting lifetime from the preliminary analysis is represented in red color. The error bars correspond to the reported statistical uncertainties only.

The first attempt of the full event reconstruction procedure has succeeded to show the first signature of $^{5}_{\Lambda}$He hypernuclei. Those preliminary results are very promising, indicating that more advanced and detailed analyses of the data will provide better results for the mass reconstruction of the hypernuclei of interest, on which the Phase 0 experiment focuses on.

7.2. Perspectives

The full event reconstruction has to be performed over the full data set of the Phase 0 experiment which took place in October 2009. The reconstruction of the other hypernuclei, $^{3}_{\Lambda}$H and $^{4}_{\Lambda}$H, as well as the reconstruction of $^{5}_{\Lambda}$He with larger statistics will be carried out. The study of the non mesonic weak decay of $^{4}_{\Lambda}$He is considered as well. The production cross section of each of hypernucleus will be estimated and the coalescence factor, useful for theoretical calculations, will be then deduced.

During this thesis work, an extension of the Phase 0 experiment has been carried out and a second experiment was performed in March 2010, where a ^{20}Ne beam was impinged on a ^{12}C target at an energy of 2 A GeV. Few modifications of the setup took place to handle this heavier beam. Mainly, the drift chamber behind the ALADiN magnet was moved out of the beam trajectory and placed on the side for the π^- detection. Signals from this drift chamber were included in the trigger system to obtain an improved π^- trigger. This recent experiment focused on the study of heavier hypernuclei and their mesonic weak decay. Their production cross section is expected to be larger than the one of light hypernuclei such as ${}^{3}_{\Lambda}$H, ${}^{4}_{\Lambda}$H, ${}^{5}_{\Lambda}$He. This larger production cross section should compensate the smaller branching ratio of the mesonic weak decay of the p-shell hypernuclei, allowing to study several heavier hypernuclear species. Non mesonic weak decay of heavier hypernuclei, which does not involve any neutron emission, such as ${}^{4}_{\Lambda}$He$\rightarrow$d+d, is also an interesting topic to focus on. Lithium-, beryllium- and boron hypernuclei are expected to be identified and some signatures of heavier hypernuclei are also possible to observe.

Meanwhile, hypernuclear experiments at J-PARC will be performed soon with the high intensity secondary (K/π) beams provided by beam line, K1.8, and its K1.8BR branch at the Hadron Hall. The first beam was successfully extracted to the Hadron Hall in January 2009, after the success of the first acceleration of the protons to 30 GeV in December 2008 [111]. During the beam time from October 2009 to February 2010, they have confirmed the yield of kaons to be above 10 thousand per spill. The first physics data will be taken by the experiment E17 dedicated to precise X-ray spectroscopy of kaonic helium 3 from October 2010. The first hypernuclear experiments namely hypernuclear γ-ray spectroscopy (E13) and Ξ hypernucleus spectroscopy (E05) will be performed soon.

Conclusion

The study of hypernuclei is an established tool to investigate hyperon-nucleon (YN) and hyperon-hyperon (YY) interactions. Until recently, hypernuclei have been produced and studied mainly by meson- or electron induced reactions. Their structure has thus been studied with a very high resolution and a comprehensive picture of the part of the YN interactions has been deduced. Their mesonic and non-mesonic weak decay modes have been under the scope of those research works as well. However, several important questions remain still open, such as the nature of the YY interactions, the dependence of the YN interaction on the hypernuclear isospin, the structure of neutron-rich hypernuclei, the branching ratios of the mesonic and non mesonic weak decays.

The HypHI project aims mainly to investigate hypernuclear matter at extreme isospin and the hypernuclear magnetic moment by means of heavy ion and rare isotope beams. Prior to any deep investigation, the feasibility of a precise hypernuclear spectroscopy had to be demonstrated in the first, Phase 0, experiment by identifying mainly ${}^{3}_{\Lambda}\mathrm{H}$, ${}^{4}_{\Lambda}\mathrm{H}$ and ${}^{5}_{\Lambda}\mathrm{He}$ hypernuclei. The achievement of the Phase 0 experiment represents the accomplishment attained in the present thesis. The development of the detailed Monte Carlo simulations have been the starting point, with the conception and design of a dedicated Time-of-Flight wall detector. After the final optimization procedure, the implementation of every detector has been carried out. The development and realization of the data acquisition and trigger systems have been a second part of the achievement. The realization of a dedicated analysis software has been the third part. The preliminary results of the Phase 0 experiment concluded the fulfillment of the present thesis.

The development of the apparatus including the design of new detectors has been the first step of the HypHI project. Monte Carlo simulations were used to describe the different physics processes needed for the conception of the complete setup. Two new detector sets were built for the experiment. First of all, a set of fiber detectors, TR0, TR1 and TR2, has been assembled and tested. These detectors allow a high precise tracking needed for the secondary vertex reconstruction. Secondly, a Time-of-Flight wall, TOF+ wall, has been designed for the detection of the hypernuclear decay fragments. The complete design of the overall experimental setup has been presented in the first part of this thesis. Several test experiments took place, and the final implementation of the detectors was accomplished in early 2009. The final optimization of the apparatus has been carried out, and the procedure has been reported as well. The performances of the detectors during the experiment, performed in October 2009, were fairly suitable for a good data taking, and the achievement obtained by the TOF+ wall is described and compared to the design specifications.

The second main part of this thesis presents the data acquisition and the trigger system which have been developed for the specific purpose of the HypHI project. Details of the conception of the three parts of the trigger are exposed. The Z=2 trigger and the secondary vertex trigger were the key of the experiment, as they allow an efficient online selection of the hypernuclei candidates. The Z=2 trigger tags events in which a fragment of charge Z=2 is detected by the TOF+ wall. The concept of this trigger subsystem and its complete implementation are described. In the offline analysis, an efficiency study has been performed and the achievement of the Z=2 trigger obtained during the experiment is shown. The concept of the secondary vertex trigger is then presented, and the algorithm programmed on FPGA (Field-Programmable Gate Array) chips for this subsystem is described. An offline analysis of the data shows a reasonably sufficient consistency between the MC simulations and the performances achieved during the experiment.

The online and offline analysis softwares were the third major part of this work, especially the physics analysis which includes the track and event reconstruction. A good momentum reconstruction is important to perform a precise spectroscopy. Thus several specific tracking algorithms have been developed to handle the complex analysis. The track finding and track fitting procedures are presented. A satisfactory efficiency study of each procedure is reported in this thesis. A momentum resolution of 1% within a wide range of momenta has been obtained for the particles of interest. Simulated data have been used to investigate the event reconstruction efficiency and the effect of several physics

cuts on the background rejection of the invariant mass spectra of hypernuclei. Several expectations on the hypernuclear reconstruction are then summarized before presenting the first preliminary results of the Phase 0 experiment.

The spectrum of the energy deposit in the TR0 detector is shown, and a fair charge separation can be observed. This achievement is crucial for the background rejection of the invariant mass distribution of hydrogen hypernuclei. The rejecting power of this energy deposit cut has been demonstrated on the simulated data. In order to investigate the detector performances, a simpler analysis than the full event reconstruction was performed. A preliminary invariant mass spectrum of the Λ-hyperon and an estimate of its lifetime are reported. A clear Λ peak is visible on top of the combinatorial background which has been analyzed by a mixed event analysis. A preliminary result of the full event reconstruction procedure, which corresponds to the invariant mass spectrum of ${}^{5}_{\Lambda}$He hypernuclei, is then presented. The lifetime of the ${}^{5}_{\Lambda}$He hypernucleus candidates has been estimated, and fairly agrees with the previously known values. Although the full statistics has not been analyzed yet, several ${}^{5}_{\Lambda}$He hypernucleus candidates have already been observed, which is the first evidence that a precise hypernuclear spectroscopy by means of heavy ion beams on a stable target is feasible.

The extended experiment mentioned in the end of Chapter 7 is a good occasion to study heavier hypernuclei by means of heavy ion collisions with an improved experimental setup. It was also a good opportunity to gather some expertise for the design of the future phases of the HypHI project. Future HypHI experiments will concentrate on the use of heavier beams, stable and radioactive, for the study of hypernuclei at extreme isospin. These future experiments will also focus on the observation of the non-mesonic weak decay, which will be another challenge. Finally, with the FAIR facility, the direct measurement of the hypernuclear magnetic moment will be accessible for the first time.

The present thesis work has contributed not only to initiate the HypHI project by conducting the Phase 0 experiment, but also to the development of the further phases of the HypHI project.

Meanwhile, at J-PARC the first hypernuclear experiments namely hypernuclear γ-ray spectroscopy (E13) and Ξ hypernucleus spectroscopy (E05) will be performed soon. The E13 experiment will focus on several single Λ hypernuclei (${}^{4}_{\Lambda}$He, ${}^{7}_{\Lambda}$Li, ${}^{10}_{\Lambda}$B, ${}^{11}_{\Lambda}$B and ${}^{19}_{\Lambda}$F). In particular, the measurement of the reduced transition probabilities of the Λ spin-flip M1($3/2^{+} \rightarrow 1/2^{+}$) transition of ${}^{7}_{\Lambda}$Li will provide information on the g-factor of a Λ inside

a nucleus, and thus an indirect measurement of the magnetic moment [112]. The E05 experiment will open a new frontier of hadronic physics in the spectroscopic studies of S=-2 baryonic system. The ΞN and ΛΛ interactions from the spectroscopic data are important to extend our knowledge of the equation of state of hadronic matter at high baryonic density, such as in the core of neutron stars.

A

Appendices

A.1. Extrapolation methods

A.1.1. Classical method: Runge Kutta method

The extrapolation of the state vector from z_0 to z_e is used to solve the ODE defined by Eq. 6.6:

$$\frac{\mathrm{d}\mathbf{r}(z)}{\mathrm{d}z} = \mathbf{f}(z, \mathbf{r}) \tag{A.1}$$

The Runge Kutta method [89] is an iterative method for integrating any ODE by performing several evaluations of $\mathbf{f}(z, \mathbf{r})$, in which each integration, subinterval is requested for a given precision.

For a step $\Delta z = z_e - z_0$ the state vector in z_e is expressed by the following Runge Kutta formula:

$$\mathbf{r}(z_e) = \mathbf{r}(z_0) + \frac{1}{6} \cdot (k_1 + 2\,k_2 + 2\,k_3 + k_4) + O((\Delta z)^5) \tag{A.2}$$

With:

$$\begin{aligned} k_1 &= \Delta z \cdot \mathbf{f}(z_0, \mathbf{r}(z_0)) \\ k_2 &= \Delta z \cdot \mathbf{f}(z_0 + \Delta z/2, \mathbf{r}(z_0) + k_1/2) \\ k_2 &= \Delta z \cdot \mathbf{f}(z_0 + \Delta z/2, \mathbf{r}(z_0) + k_2/2) \\ k_3 &= \Delta z \cdot \mathbf{f}(z_e, \mathbf{r}(z_0) + k_3) \end{aligned} \tag{A.3}$$

The covariance matrix C in z_e is obtained by calculating the Jacobian matrix and Eq. 6.8. The Jacobian matrix is evaluated by a combination of Jacobians of k_i:

$$J(z_e) = \frac{\mathrm{d}\mathbf{r}(z_e)}{\mathrm{d}\mathbf{r}(z_0)} = I_5 + \frac{1}{6} \cdot (J_1 + 2\,J_2 + 2\,J_3 + J_4) \tag{A.4}$$

With $z_i = \left\{ z_0; z_0 + \frac{\Delta z}{2}; z_0 + \frac{\Delta z}{2}; z_e \right\}$:

$$J_i = \frac{\mathrm{d}k_i}{\mathrm{d}\mathbf{r}(z_0)} = \Delta z \cdot \frac{\mathrm{d}\mathbf{f}(z_i, \mathbf{r}(z_i))}{\mathrm{d}\mathbf{r}(z_0)} = \left.\frac{\mathrm{d}\mathbf{f}(z, \mathbf{r}(z))}{\mathrm{d}\mathbf{r}(z)}\right|_{z_i} \cdot (I_5 + J_{i-1}\frac{z_i - z_0}{\Delta z}) \cdot \Delta z \tag{A.5}$$

Where the Jacobian matrix of $\mathbf{f}$ is given by:

$$\frac{\mathrm{d}\mathbf{f}(z, \mathbf{r})}{\mathrm{d}\mathbf{r}} = \begin{pmatrix} 0 & 0 & 1 & 0 & 0 \\ 0 & 0 & 0 & 1 & 0 \\ 0 & 0 & \partial t'_x/\partial t_x & \partial t'_x/\partial t_y & \partial t'_x/\partial(q/p) \\ 0 & 0 & \partial t'_y/\partial t_x & \partial t'_y/\partial t_y & \partial t'_y/\partial(q/p) \\ 0 & 0 & 0 & 0 & 0 \end{pmatrix} \tag{A.6}$$

In this way, the new state vector $\mathbf{r}$ can be estimated from an initial state. The track propagation across the setup is achieved by dividing the integration interval into steps. Each step becomes an initial value problem and can be solved as best suited for that particular part of the integration interval.

A.1.2. Analytic formula for track extrapolation

The idea of this method is to expand the equations 6.10 in series of antiderivatives of the magnetic field $\mathbf{B}$ by repeated integration of successive derivations of the track directions t_x and t_y. Eqs. 6.10 are linear with respect to the magnetic field, therefore the derivatives of $\mathbf{a}$ and $\mathbf{b}$ can be written for these same equations:

$$\begin{cases} \dfrac{\partial \mathbf{a}}{\partial z} &= \dfrac{\partial \mathbf{a}}{\partial t_x} \cdot \dfrac{\partial t_x}{\partial z} + \dfrac{\partial \mathbf{a}}{\partial t_y} \cdot \dfrac{\partial t_y}{\partial z} \\ \dfrac{\partial \mathbf{b}}{\partial z} &= \dfrac{\partial \mathbf{b}}{\partial t_x} \cdot \dfrac{\partial t_x}{\partial z} + \dfrac{\partial \mathbf{b}}{\partial t_y} \cdot \dfrac{\partial t_y}{\partial z} \end{cases} \tag{A.7}$$

By substituting t'_x and t'_y from the equations 6.10, Eq. A.7 can be rewritten as:

$$\begin{cases} \mathbf{a}' &= \sum\limits_{i_1 \subset \{x,y,z\}} B_{i_1}(z) \left(\dfrac{\partial \mathbf{a}}{\partial t_x} \cdot a_{i_1}(z) + \dfrac{\partial \mathbf{a}}{\partial t_y} \cdot b_{i_1}(z) \right) \\ \mathbf{b}' &= \sum\limits_{i_1 \subset \{x,y,z\}} B_{i_1}(z) \left(\dfrac{\partial \mathbf{b}}{\partial t_x} \cdot a_{i_1}(z) + \dfrac{\partial \mathbf{b}}{\partial t_y} \cdot b_{i_1}(z) \right) \end{cases} \tag{A.8}$$

Hereby, let us introduce the new functions $\mathbf{a}_{i_1}$ and $\mathbf{b}_{i_1}$ as:

$$\begin{cases} \mathbf{a_{i_1}}(z) &= \dfrac{\partial \mathbf{a}}{\partial t_x} \cdot a_{i_1}(z) + \dfrac{\partial \mathbf{a}}{\partial t_y} \cdot b_{i_1}(z) \\ \mathbf{b_{i_1}}(z) &= \dfrac{\partial \mathbf{b}}{\partial t_x} \cdot a_{i_1}(z) + \dfrac{\partial \mathbf{b}}{\partial t_y} \cdot b_{i_1}(z) \end{cases} \tag{A.9}$$

In order to rewrite Eq. A.8 in a similar manner as Eq. 6.10:

$$\begin{cases} \mathbf{a}'(z) = \sum_{i_1 \subset \{x,y,z\}} B_{i_1}(z) \cdot \mathbf{a_{i_1}}(z) \\ \mathbf{b}'(z) = \sum_{i_1 \subset \{x,y,z\}} B_{i_1}(z) \cdot \mathbf{b_{i_1}}(z) \end{cases} \tag{A.10}$$

By the same procedure, derivatives of $\mathbf{a}_{i_1}$ and $\mathbf{b}_{i_1}$ can also be written in a similar way:

$$\begin{cases} \mathbf{a_{i_1}}'(z) &= \sum\limits_{i_2 \subset \{x,y,z\}} B_{i_2}(z) \left(\dfrac{\partial \mathbf{a_{i_1}}(z)}{\partial t_x} \cdot a_{i_2}(z) + \dfrac{\partial \mathbf{a_{i_1}}(z)}{\partial t_y} \cdot b_{i_2}(z) \right) = \sum\limits_{i_2 \subset \{x,y,z\}} B_{i_2}(z)\ \mathbf{a_{i_1 i_2}}(z) \\ \mathbf{b_{i_1}}'(z) &= \sum\limits_{i_2 \subset \{x,y,z\}} B_{i_2}(z) \left(\dfrac{\partial \mathbf{b_{i_1}}(z)}{\partial t_x} \cdot a_{i_2}(z) + \dfrac{\partial \mathbf{b_{i_1}}(z)}{\partial t_y} \cdot b_{i_2}(z) \right) = \sum\limits_{i_2 \subset \{x,y,z\}} B_{i_2}(z)\ \mathbf{b_{i_1 i_2}}(z) \end{cases} \tag{A.11}$$

With:

$$\begin{cases} \mathbf{a_{i_1 i_2}}(z) &= \dfrac{\partial \mathbf{a_{i_1}}}{\partial t_x} \cdot a_{i_2}(z) + \dfrac{\partial \mathbf{a_{i_1}}}{\partial t_y} \cdot b_{i_2}(z) \\ \mathbf{b_{i_1 i_2}}(z) &= \dfrac{\partial \mathbf{b_{i_1}}}{\partial t_x} \cdot b_{i_2}(z) + \dfrac{\partial \mathbf{b_{i_1}}}{\partial t_y} \cdot b_{i_2}(z) \end{cases} \tag{A.12}$$

In general, derivatives of $\mathbf{a_{i_1 \cdots i_n}}$ and $\mathbf{b_{i_1 \cdots i_n}}$ can be expressed as:

$$\begin{cases} \mathbf{a_{i_1 \cdots i_n}}'(z) &= \sum\limits_{i_n \subset \{x,y,z\}} B_{i_n}(z)\ \mathbf{a_{i_1 \cdots i_{n-1}}}(z) \\ \mathbf{b_{i_1 \cdots i_n}}'(z) &= \sum\limits_{i_n \subset \{x,y,z\}} B_{i_n}(z)\ \mathbf{b_{i_1 \cdots i_{n-1}}}(z) \end{cases} \tag{A.13}$$

Where both functions $\mathbf{a_{i_1\cdots i_n}}$ and $\mathbf{b_{i_1\cdots i_n}}$ are obtained recursively:

$$\begin{cases} \mathbf{a_{i_1\cdots i_n}}(z) & = \dfrac{\partial \mathbf{a_{i_1\cdots i_{n-1}}}}{\partial t_x} \cdot a_{i_n}(z) + \dfrac{\partial \mathbf{a_{i_1\cdots i_{n-1}}}}{\partial t_y} \cdot b_{i_n}(z) \\ \mathbf{b_{i_1\cdots i_n}}(z) & = \dfrac{\partial \mathbf{b_{i_1\cdots i_{n-1}}}}{\partial t_x} \cdot a_{i_n}(z) + \dfrac{\partial \mathbf{b_{i_1\cdots i_{n-1}}}}{\partial t_y} \cdot b_{i_n}(z) \end{cases} \tag{A.14}$$

With **a** and **b** defined by the equations 6.11, the (n-1)th derivative of t_x and t_y is obtained from the previous recursion.

Consecutively, $t_x(z_e)$ and $t_y(z_e)$ can be expressed from $t_x(z_0)$ and $t_y(z_0)$ as an expansion of antiderivatives:

$$\begin{aligned} t_x(z_e) &= t_x(z_0) + \int_{z_0}^{z_e} t'_x(z_1)\,\mathrm{d}z_1 \\ &= t_x(z_0) + \sum_i \int_{z_0}^{z_e} B_i(z_1) a_i(z_1)\,\mathrm{d}z_1 \\ &= t_x(z_0) + \sum_i \int_{z_0}^{z_e} B_i(z_1)\Big(a_i(z_0) + \int_{z_0}^{z_1} a'_i(z_2)\mathrm{d}z_2\Big)\,\mathrm{d}z_1 \\ &= t_x(z_0) + \sum_i \int_{z_0}^{z_e} B_i(z_1)\Big(a_i(z_0) + \int_{z_0}^{z_1} \sum_{i_1} B_{i_1}(z_2) a_{i_1}(z_2)\,\mathrm{d}z_2\Big)\,\mathrm{d}z_1 \\ &= t_x(z_0) + \sum_i a_i(z_0) \int_{z_0}^{z_e} B_i(z_1)\,\mathrm{d}z_1 + \sum_{i\,i_1} \int_{z_0}^{z_e} B_i(z_1) \int_{z_0}^{z_1} B_{i_1}(z_2) a_{i_1}(z_2)\,\mathrm{d}z_2\,\mathrm{d}z_1 \\ &= t_x(z_0) + \sum_i a_i(z_0) \int_{z_0}^{z_e} B_i(z_1)\,\mathrm{d}z_1 + \sum_{i\,i_1} a_{i_1}(z_0) \int_{z_0}^{z_e} B_i(z_1) \int_{z_0}^{z_1} B_{i_1}(z_2)\,\mathrm{d}z_2\,\mathrm{d}z_1 \\ &\quad + \sum_{i\,i_1\,i_2} \int_{z_0}^{z_e} B_i(z_1) \int_{z_0}^{z_1} B_{i_1}(z_2) \int_{z_0}^{z_2} B_{i_2}(z_3) a_{i_1 i_2}(z_3)\,\mathrm{d}z_3\,\mathrm{d}z_2\,\mathrm{d}z_1 \\ &= \cdots \end{aligned} \tag{A.15}$$

Where the index i_k stands for the components x, y, z.

The expression for t_y is similar to the equation A.15 with $b_{i\,i_1\cdots\,i_k}$ and b_i instead of $a_{i\,i_1\cdots\,i_k}$ and a_i. The expansion to any order can then be written:

$$\begin{aligned} t_x(z_e) = t_x(z_0) &+ \sum_{k=1}^{n} \sum_{i\,i_1\cdots i_k \subset \{x,y,z\}} a_{i\,i_1\cdots i_k}(z_0) \int_{z_0}^{z_e} B_i(z_1) \cdots \int_{z_0}^{z_{k-1}} B_i(z_k)\,\mathrm{d}z_k \cdots \mathrm{d}z_1 \\ &+ \mathrm{O}\Big(\frac{\kappa B(q/p)(z_e - z_0)^{n+1}}{(n+1)!}\Big) \end{aligned} \tag{A.16}$$

To achieve a more practical expression, let us introduce several new variables. The integrals of magnetic field can be denoted:

$$S_{i\,i_1\cdots i_k} = \int_{z_0}^{z_e} B_i(z_1)\cdots\int_{z_0}^{z_{k-1}} B_{i_k}(z_k)\,\mathrm{d}z_k\cdots\mathrm{d}z_1 \tag{A.17}$$

$$s_{i\,i_1\cdots i_k} = \int_{z_0}^{z_e}\int_{z_0}^{z} B_i(z_1)\cdots\int_{z_0}^{z_{k-1}} B_{i_k}(z_{k-1})\,\mathrm{d}z_{k-1}\cdots\mathrm{d}z_1\mathrm{d}z \tag{A.18}$$

Let us also define:

$$A_{i\,i_1\cdots i_k} = a_{i\,i_1\cdots i_k}/h^k \tag{A.19}$$

$$B_{i\,i_1\cdots i_k} = b_{i\,i_1\cdots i_k}/h^k \tag{A.20}$$

with h expressed in equation 6.13

A.2. UML diagram of online-offline analysis

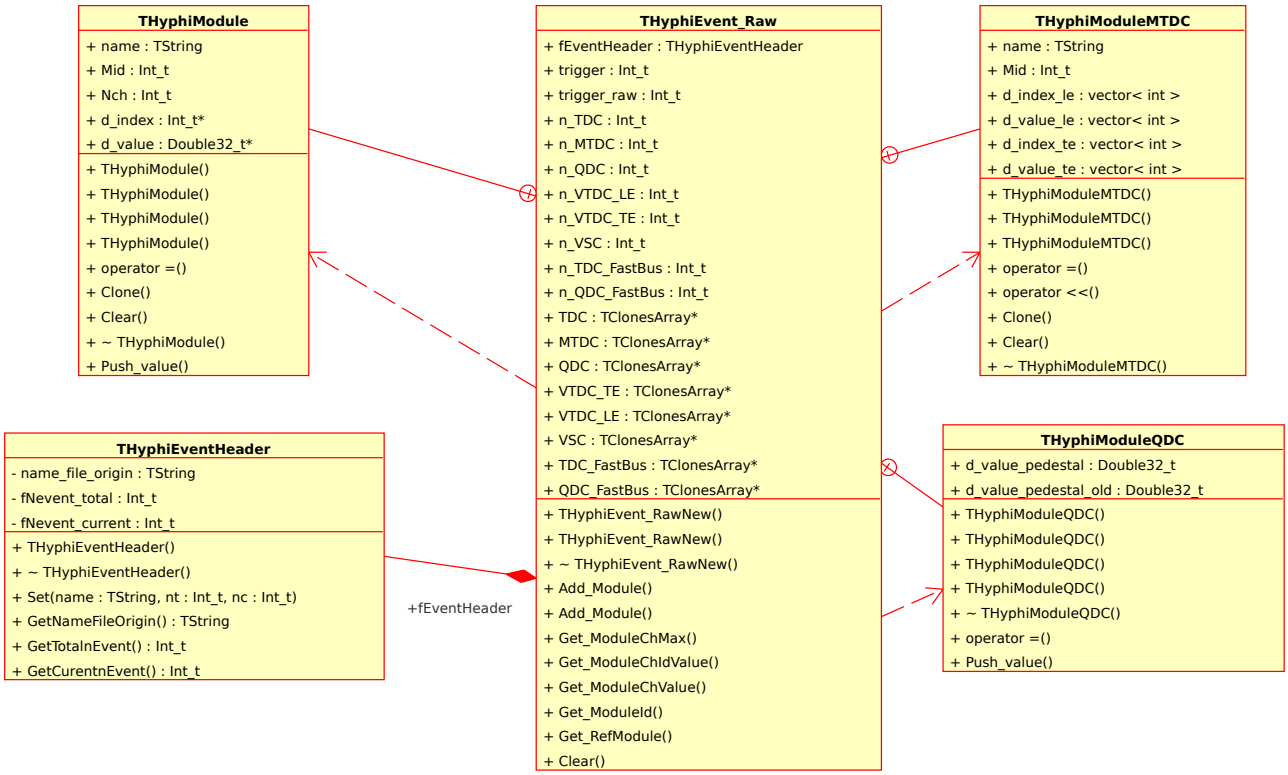

Figure A.1.: UML diagram of the class `THyphiEvent_Raw`. This data structure corresponds to the *Unpacker* procedure described in Chapter 6. It includes raw data separated in 3 classes : `THyphiModule` (no specification), `THyphiModuleQDC` (for QDC), `THyphiModuleMTDC` (for multiTDC)

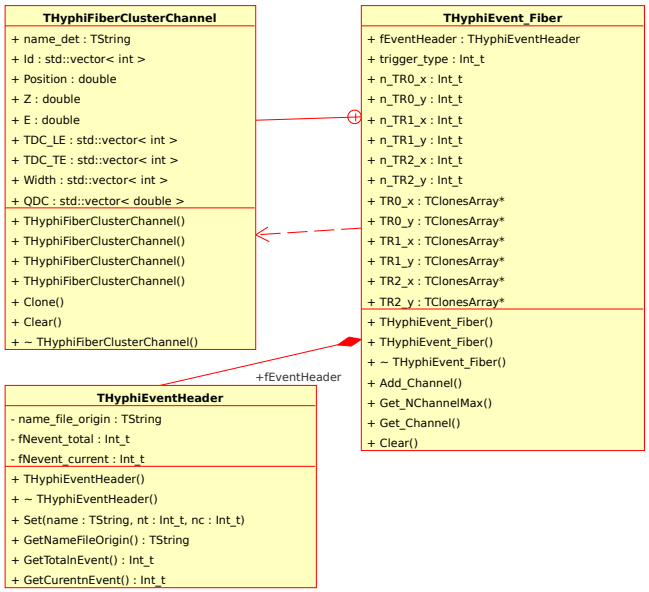

Figure A.2.: UML diagram of the class `THyphiEvent_Fiber`. This data structure corresponds to the *Calibration* procedure of the fiber detector sets described in Chapter 6. Data of the fiber detector are represented as cluster hit in a class `THyphiFiberClusterChannel`.

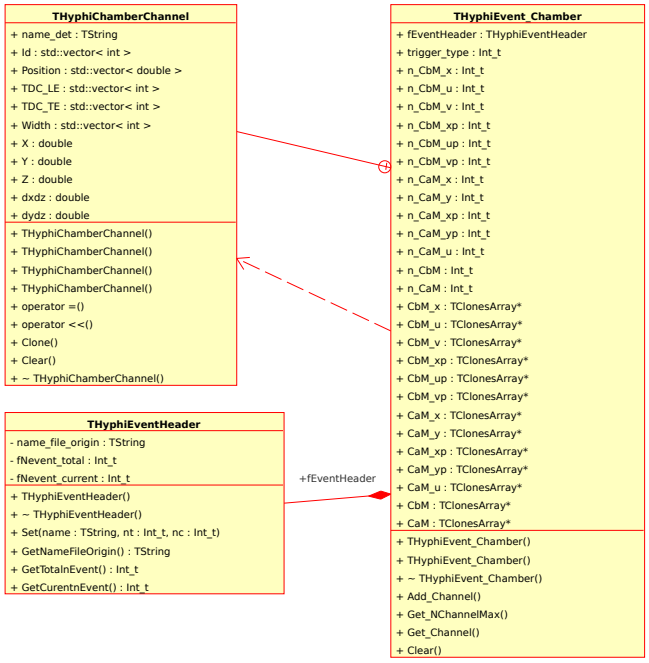

Figure A.3.: UML diagram of the class `THyphiEvent_Chamber`. This data structure is used in the *Calibration* step of the drift chambers described in Chapter 6. Data related to the drift chambers are represented as wire channel in a class `THyphiChamberChannel`

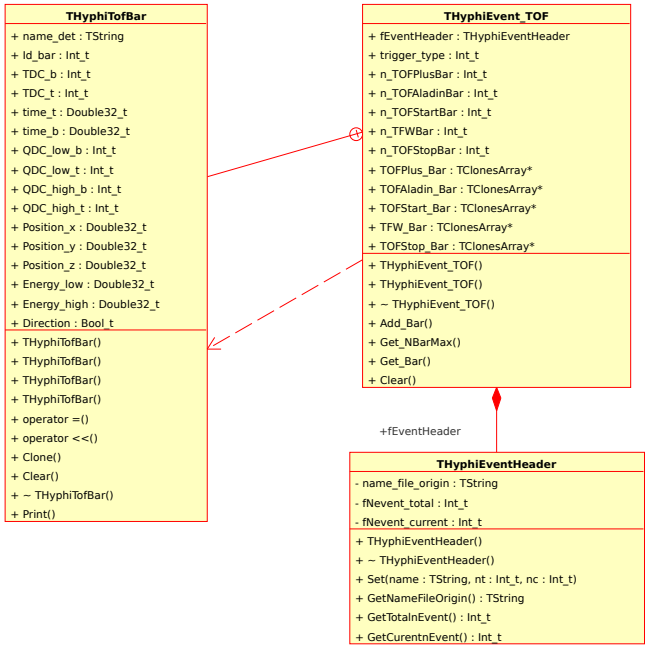

Figure A.4.: UML diagram of the class `THyphiEvent_TOF`. This data structure is used in the *Calibration* step of the detectors related with the Time-of-Flight measurement. Data related to those detectors is represented as scintillating TOF bar in a class `THyphiTofBar`

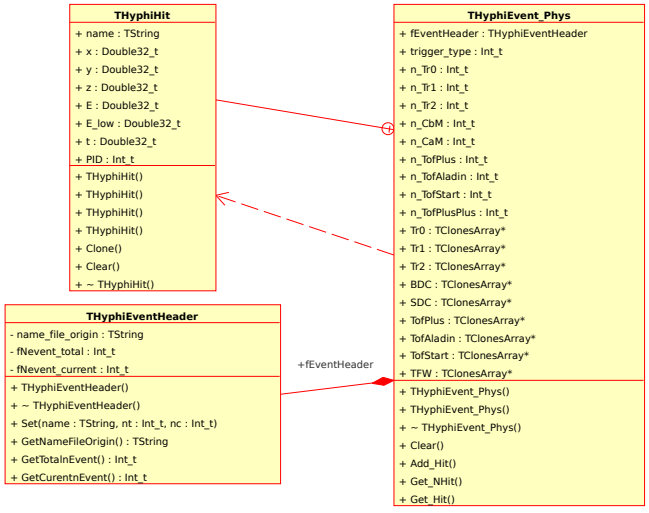

Figure A.5.: UML diagram of the class `THyphiEvent_Phys`. This data structure is used in the *Merger* procedure described in Chapter 6. All data structure of calibrated detectors is merged in a single structure. Each detector information is transposed in the laboratory frame in a class `THyphiHit`

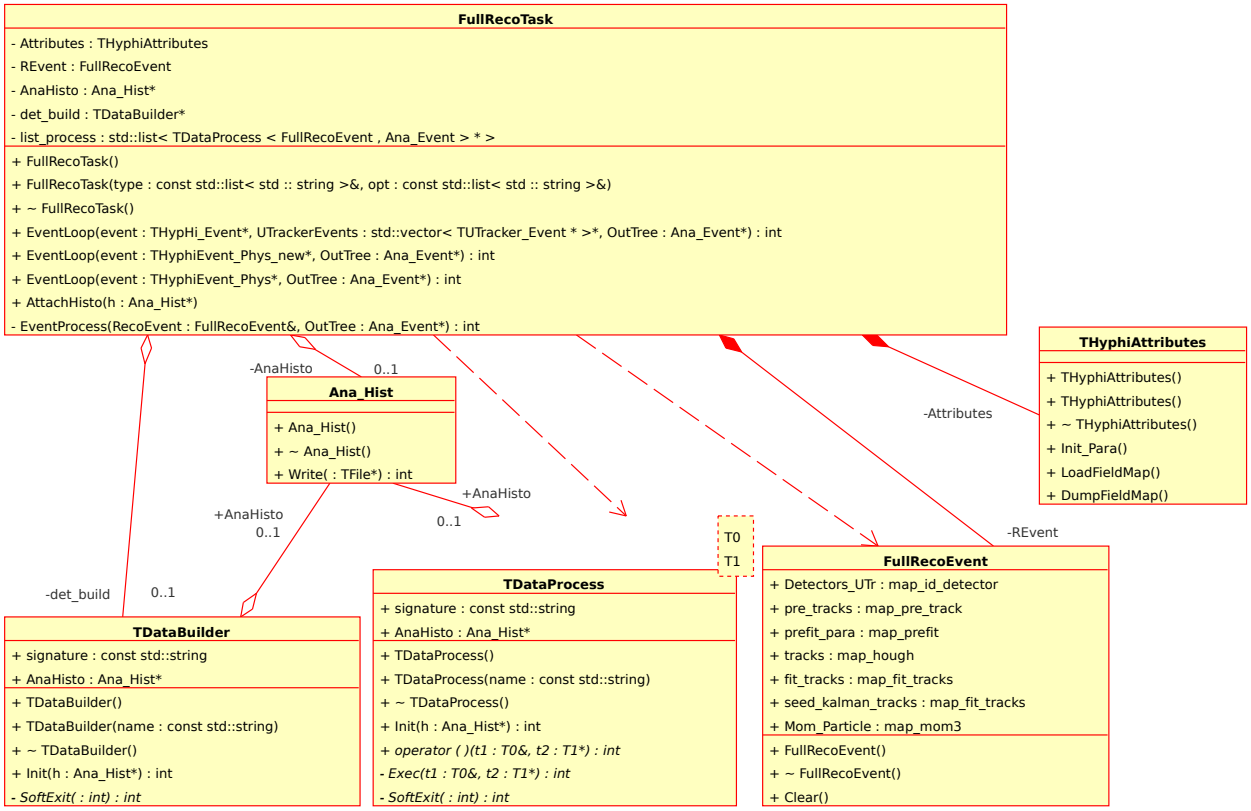

Figure A.6.: UML diagram of the class `FullRecoTask`. This class corresponds to the task manager of the full event reconstruction analysis described in Chapter 7. A virtual data `TDataBuilder` is used to handle the input data to analyze, which can be the simulated data or experimental data. The list `list_process` of `TDataProcess` corresponds to list of procedures that the event reconstruction should execute in order. Usually this list contains the procedures of pre-tracking, track finding, track fitting and secondary vertex reconstruction, which have been presented in Chapter 6. The class `FullRecoEvent` gathers the different data structure which are used by the classes `TDataProcess`. All parameters needed is gathered in the object `Attributes` of the class `THyphiAttributes`. All histograms, which are used and intended to be saved, are in class `Ana_Hist`.

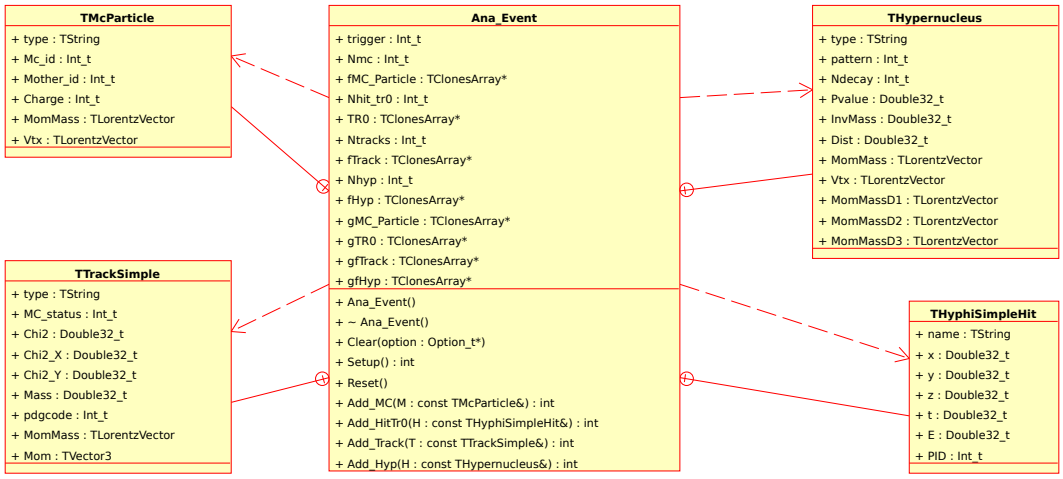

Figure A.7.: UML diagram of the class `Ana_Event`. The output of the event loop in the FullRecoTask task manager is loaded in a class of `Ana_Event`. Four different kind of objects is gathered in this class: The cluster hit of the TR0 detector in order to be able to those information for the background rejection, as discussed in Chapter 7. The output data of the track fitting are available via the object class `TTrackSimple`. When simulated data are analyzed the MC information are saved in the objects `TMcParticle`, useful for latter comparison. The last structure is `THypernucleus` which corresponds to the hypernucleus candidates after the achieved secondary vertex reconstruction.

Bibliography

[1] P. Koch, B. Muller, and J. Rafelski, *Strangeness in relativistic heavy ion collisions*, Phys. Rep. **142** (1986) 167.

[2] Spyridon Margetis, Karel Safarik and Orlando Villalobos Baillie, *Strangeness production in heavy-ion collisions*, Annu. Rev. Nucl. Part. Sci. **50** (2000) 299.

[3] R. D. McKeown, *Sensitivity of polarized elastic electron-proton scattering to the anomalous baryon number magnetic moment*, Phys. Lett. B **219** (1989) 140;
D. H. Beck, *Strange-quark vector currents and parity-violating electron scattering from the nucleon and from nuclei*, Phys. Rev. D **39** (1989) 3248;
F. E. Maas, et al, *Measurement of Strange-Quark Contributions to the Nucleons Form Factors at* $Q^2 = 0.230(GeV/c)^2$, Phys. Rev. Lett. **93** (2004) 022002.

[4] J.Barrette et al, Λ *production and flow in Au-Au collisions at 11.5 A GeV/c*, Phys. Rev. C **63** (2000) 014902.

[5] F Antinori et al, *Strangeness enhancements at central rapidity in 40 A GeV/c Pb-Pb collisions*, J. Phys. G: Nucl. Part. Phys. **37** (2010) 045105.

[6] Fridolin Weber, *Strangeness in neutron stars*, J. Phys. G: Nucl. Part. Phys. **27** (2001) 465.

[7] J. Pochodzalla et al., *Probing the Nuclear Liquid-Gas Phase Transistion*, Phys. Rev. Lett. **75** (1995) 1040.

[8] W. Trautmann, *Multifragmentation and the liquid-gas phase transition: an experimental overview*, Nucl. Phys. A **752** (2005) 407c.

[9] H. A. Gustafsson et al., *Collective Flow Observed in Relativistic Nuclear Collisions*, Phys. Rev. Lett. **52** (1984) 1590.

[10] S. C. Jeong et al., *Collective motion in selected central collisions of Au on Au at 150 A MeV*, Phys. Rev. Lett. **72** (1994) 3468.

[11] D. Miśkowiec et al., *Observation of enhanced subthreshold K+ production in central collisions between heavy nuclei*, Phys. Rev. Lett. **72** (1994) 3650.

[12] H. Oeschler, *Strangeness production at 1-2 A GeV*, Prog. Part. Nucl. Phys. **62** (2009) 433.

[13] F. Weber and M. K. Weigel, *Equation of state of dense baryonic matter*, J. Phys. G: Nucl. Part. Phys. **15** (1989) 765.

[14] N.K. Glendenning, *The hyperon composition of neutron stars*, Phys. Lett. B **114** (1982) 392.

[15] Jürgen Schaffner and Igor N. Mishustin, *Hyperon-rich matter in neutron stars*, Phys. Rev. C **53** (1996) 53.

[16] H. Tamura, *Baryon-baryon interactions with strangeness studied from hypernuclei*, Nucl. Phys. A **752** (2005) 155.

[17] O. Hashimoto, H. Tamura, *Spectroscopy of* Λ *hypernuclei*, Prog. Part. Nucl. Phys. **57** (2006) 564.

[18] M. Gell-Mann, *Isotopic Spin and New Unstable Particles*, Phys. Rev. **92** (1953) 833.

[19] Tadao Nakano and Kazuhiko Nishijima, *Charge Independence for V-particles*, Prog. Theor. Phys. **10** (1953) 581.

[20] D. J. Millener, C. B. Dover and A. Gal, Λ*-nucleus single-particle potentials*, Phys. Rev. C **38** (1988) 2700.

[21] D. H. Davis, R. Levi Setti, M. Raymund, O. Skjeggestad, and G. Tomasini, *Binding Energy of* Λ^0 *Hyperons in Heavy Hypernuclei (60<A<100)*, Phys. Rev. Lett. **9** (1962) 464.

[22] F. Weber, *Pulsars as Astrophysical Laboratories for Nuclear and Particle Physics*. High Energy Physics, Cosmology and Gravitation Series (IOPPublishing, Bristol, GreatBritain, 1999).

[23] Jürgen Schaffner-Bielich, *Hypernuclear physics for neutron stars*, Nucl. Phys. A **804** (2008) 309.

[24] W.M. Albericoa, G. Garbarino, *Weak decay of* Λ*-hypernuclei*, Phys. Rep. **369** (2002) 1.

[25] E.Oset et al., *A Review on Mesonic Decay of* Λ *Hypernuclei*, Prog. Theor. Phys. Suppl. **117** (1994) 461.

[26] J. Cohen, *Weak non-mesonic decays of* Λ*-hypernuclei*, Nucl. Phys. A **547** (1992) 133.

[27] M. Danysz, J. Pniewski, Philos. Mag. **44** (1953) 348.

[28] J. D. Walecka, *The binding energy of* Λ*-particles in nuclear matter*, Il Nuovo Cimento **16** (1960) 342.

[29] Lemonne J et al., *A determination of the* Λ*-nuclear potential well-depth*, Phys. Lett. **18** (1965) 354.

[30] W. Brückner et al., *Spin-orbit interaction of lambda particles in nuclei*, Phys. Lett. B **79** (1978) 157.

[31] M. May et al., *Observation of Levels in* ${}^{13}_{\Lambda}C$*,* ${}^{14}_{\Lambda}N$*, and* ${}^{18}_{\Lambda}O$ *Hypernuclei*, Phys. Rev. Lett. **47** (1981) 1106.

[32] C. Milner et al., *Observation of* Λ*-Hypernuclei in the Reaction* ${}^{12}C(\pi^+, K^+)\ {}^{12}_{\Lambda}C$, Phys. Rev. Lett. **54** (1985) 1237.

[33] P.H. Pile et al., *Study of hypernuclei by associated production*, Phys. Rev. Lett. **66** (1991) 2585.

[34] M. Akel et al., *The* (π^+, K^+) *reaction on* ${}^{12}C$ *and* ${}^{56}Fe$, Nucl. Phys. A **534** (1991) 478.

[35] T. Hasegawa et al., *Core-Excited States of* $\Lambda{}^{12}C$ *Hypernuclei Formed in the* (π^+, K^+) *reaction*, Phys. Rev. Lett. **74** (1995) 224.

[36] O. Hashimoto et al., *The* (π^+, K^+) *reaction and light* Λ *hypernuclear spectroscopy*, Nucl. Phys. A **639** (1998) 93c.

[37] H. Hotchi et al., *Spectroscopy of medium-heavy* Λ *hypernuclei via the* (π^+, K^+) *reaction*, Phys. Rev. C **64** (2001) 044302.

[38] H. Tamura et al., *Observation of a Spin-Flip M1 Transition in* ${}^{7}_{\Lambda}Li$, Phys. Rev. Lett. **84** (2000) 5963.

[39] T. Miyoshi et al., *High Resolution Spectroscopy of the* ${}^{12}_{\Lambda}B$ *Hypernucleus Produced by the* $(e, e'K^+)$ *Reaction*, Phys. Rev. Lett. **90** (2003) 232502.

[40] M.M. Nagels et al., *Baryon-baryon scattering in a one-boson-exchange-potential approach. II. Hyperon-nucleon scattering*, Phys. Rev. D **15** (1977) 2547;
M.M. Nagels et al., *Baryon-baryon scattering in a one-boson-exchange-potential approach. III. A nucleon-nucleon and hyperon-nucleon analysis including contributions of a nonet of scalar mesons*, Phys. Rev. D **20** (1979) 1633;
P.M. Maessen et al., *Soft-core baryon-baryon one-boson-exchange models. II. Hyperon-nucleon potential*, Phys. Rev. C **40** (1989) 2226;
Th.A. Rijken, V.G.J. Stokes, Y. Yamamoto, *Soft-core hyperon-nucleon potentials*, Phys. Rev. C **59** (1999) 21.

[41] B. Holzenkamp et al., *A meson exchange model for the hyperon-nucleon interaction*, Nucl. Phys. A **500** (1989) 485;
K. Holinde, *The Jülich hyperon-nucleon interaction models*, Nucl. Phys. A **547** (1992) 255.

[42] R.H. Dalitz, A. Gal, *The formation of, and the* γ*-radiation from, the p-shell hypernuclei*, Ann. Phys. **116** (1978) 167.

[43] D.J. Millener, A. Gal, C.B. Dover, R.H. Dalitz, *Spin dependence of the* ΛN *effective interaction*, Phys. Rev. C **31** (1985) 499.

[44] H. Bandö, T. Motoba, Y. Yamamoto, *Narrow widths of* Λ *single particle states in hypernuclei*, Phys. Rev. C **31** (1985) 265.

[45] A. Likar, M. Rosina, B. Povh, *The Lambda particle as a probe of deeply bound single particle states in heavy nuclei*, Z. Phys. A **324** (1986) 35.

[46] Kiyoshi Tanida, *Experimental Program at J-PARC*, Nucl. Phys. A **835** (2010) 75.

[47] K. Imai et al., *Letter of Intent for Nuclear and Particle Physics Experiments at the J-PARC (L06)*, The J-PARC Project Ofce, KEK, J-PARC 03-6, 2003, p. 77.

[48] J. Pochodzalla, *Future hypernuclear physics at MAMI-C and PANDA-GSI*, Nucl. Phys. A **754** (2005) 430.

[49] A. K. Kerman and M. S. Weiss, *Superstrange Nuclei*. Phys. Rev. C **8** (1973) 408.

[50] F. Asai, H. Bando, M. Sano, *The probability of hypernucleus production in high-energy heavy-ion collisions*, Phys. Lett. B **145** (1984) 19.

[51] M. Wakai, H. Bando, M. Sano, *Hypernucleus formation in high-energy collisions*, Phys. Rev. C **38** (1988) 748.

[52] H.Bando, M. Sano, M. Wakai, and J.Zofka, *Production of hypernuclei in relativistic ion beams*, Nucl. Phys. A **501** (1989) 900.

[53] H. Bando, et al., *Energy dependence of hypernucleus production in high-energy nuclear collision*, Nucl. Phys. A **547** (1992) 89c.

[54] S.A. Bass, et al., *Microscopic models for ultrarelativistic heavy ion collisions*, Prog. Part. Nucl. Phys. **41** (1998) 255.

[55] T. Gaitanos, H. Lenske, and U. Mosel, *Formation of hypernuclei in high energy reactions within a covariant transport model*, Phys. Lett. B **675** (2009) 297.

[56] D.H.E. Gross, *Statistical decay of very hot nuclei-the production of large clusters*, Rep. Prog. Phys. **53** (1990) 605.

[57] T.H.R. Skyrme, *The effective nuclear potential*, Nucl. Phys. **9** (1959) 615.

[58] L.P. Kadanoff, G. Baym, *Quantum Statistical Mechanics*, Benjamin, N.Y., 1962.

[59] B. Blättel, V. Koch, U. Mosel, *Transport-theoretical analysis of relativistic heavy-ion collisions*, Rep. Prog. Phys. **56** (1993) 1.

[60] http://gibuu.physik.uni-giessen.de/GiBUU/

[61] A.S. Botvina, et al., *Statistical simulation of the break-up of highly excited nuclei*, Nucl. Phys. A **475** (1987) 663.

[62] J.P. Bondorf, et al., *Statistical multifragmentation of nuclei*, Phys. Rep. **257** (1995) 133.

[63] H. Tamura, *Impurity nuclear physics*, Eur. Phys. J. A **13** (2002) 181.

[64] D. Vretenar, W. Pöschl, G. A. Lalazissis, and P. Ring, *Relativistic mean-field description of light Λ-hypernuclei with large neutron excess*, Phys. Rev. C **57** (1998) R1060.

[65] H.F. Lu et al., *Neutron halos in hypernuclei*, Eur. Phys. J. A **17** (2003) 19.

[66] C Samanta, P Roy Chowdhury and D. N. Basu, *Lambda hyperonic effect on the normal drip lines*, J. Phys. G: Nucl. Part. Phys. **35** (2008) 065101.

[67] A. O. Gattone and M. Chiapparini, Λ*-hypernuclei magnetic moments in a relativistic model*, Phys. Rev. C **44** (1991) 548.

[68] J. Cohen and J. V. Noble, *Hypernuclear currents in a relativistic mean-field theory with tensor* ωYY *couplings*, Phys. Rev. C **46** (1992) 801.

[69] Y. Tanaka, *The Schmidt diagrams and the configuration mixing effects on hypernuclear magnetic moments*, Phys. Lett. B **227** (1989) 195.

[70] C. B. Dover, H. Feshbach, A. Gal, *Signatures of* $\Lambda - \Sigma$ *mixing in the magnetic moments of hypernuclei*, Phys. Rev. C **51** (1995) 541.

[71] T.R. Saito, *et al.*, *Letter Of Intent of "Hypernuclei with Stable Heavy Ion Beam and RI-beam Induced Reactions at GSI (HypHI)"*, submitted to GSI EA 30.

[72] A.U. Abdurakhimov, et al, *Experimental study of relativistic hypernuclei using the Hybs spectrometer*, Nuovo Cimento A **102** (1989) 645.

[73] S. Avramenko, et al, *A study of the production and lifetime of the lightest relativistic hypernuclei*. Nucl. Phys. A **547** (1992) 95.

[74] T.A. Armstrong, et al, *Production of* ${}^{3}_{\Lambda}H$ *and* ${}^{4}_{\Lambda}H$ *in central 11.5 GeV/c Au+Pt heavy ion collisions*, Phys. Rev. C **70** (2004) 024902.

[75] The STAR Collaboration et al, *Observation of an Antimatter Hypernucleus*, Science **328** (2010) 58.

[76] A. Ozawa, et al, *Interaction cross sections and radii of light nuclei*, Nucl. Phys. A **608** (1996) 63.

[77] D. Nakajima, B. Özel-Tashenov, S. Bianchin, O. Borodina, V. Bozkurt, B. Göküzüm, M. Kavatsyuk, S. Minami, C. Rappold, T. Saito, et al, *Scintillating fiber detectors for the HypHI project at GSI*, Nucl. Instr. Meth. A **608** (2009) 287.

[78] P. Achenbach et al., *In-beam tests of scintillating fibre detectors at MAMI and at GSI*, Nucl. Instr. Meth. A **593** (2008) 353.

[79] T. Fukuda, et al, *The superconducting kaon spectrometer SKS*, Nucl. Instr. Meth. A **361** (1995) 485.

[80] S. Bianchin, et al, *Progress on the Time-of-Flight detectors for the HypHI project*, GSI Scientific Report 2008 (2008) 233.

[81] S. Bianchin, *Multifragmentation : Rôle de la masse et de l'isopin*. PhD thesis, University of Strasbourg (France) (2007).

[82] S. Agostinelli et al, *GEANT 4 - a simulation toolkit*, Nucl. Instr. Meth. A **506** (2003) 250.

[83] R. Brun and F. Rademakers, *ROOT An object oriented Data Analysis Framework*, Nucl. Instr. Meth. A **389** (1997) 81.
I. Antcheva et al., *ROOT - A C++ framework for petabyte data storage, statistical analysis and visualization*, Comp. Phys. Comm. **180** (2009) 2499.

[84] ANSYS®Academic Research, Release 12.1, ANSYS, Inc.

[85] H.G. Essel and N. Kurz, *The general purpose data acquisition system MBS*, IEEE Trans. on Nuclear Science Vol. **47**, No.2 (2000) 337.

[86] T. Yoshioka *et al.*, *Upgrade of the Level-0 trigger system for BNL-E949*, IEEE Trans. on Nuclear Science Vol. **51**, No.3 (2004) 334.

[87] J. Adamczewski, M. Al-Turany, D. Bertini, H.G. Essel, M. Hemberger, N. Kurz, M. Richter, *Go4 multitasking class library with ROOT*, IEEE Trans. on Nuclear Science Vol. **49**, No.2 (2002) 521.

[88] J. Adamczewski, M. Al-Turany, D. Bertini, H.G. Essel, N. Kurz, S. Linev, M. Richter, *Go4 on-line monitoring*, IEEE Trans. on Nuclear Science Vol. **51**, No.3 (2004) 565.

[89] C. Runge, *Über die numerische Auflösing von Differentialgleichungen*, Math. Ann. **46** (1895) 167. M. W. Kutta, Z. für Math. u. Phys. **46** (1901) 435.

[90] S. Gorbunov, I. Kisel, *Analytic formula for track extrapolation in non-homogeneous magnetic field*, Nucl. Instr. Meth. A **559** (2006) 148.

[91] I. Kisel, *Event reconstruction in the CBM experiment*, Nucl. Instr. Meth. A **566** (2006) 85.

[92] R. Mankel, *Pattern Recognition and Event Reconstruction in Particle Physics Experiments*, Rep. Prog. Phys. **67** (2004) 553.

[93] P.V.C. Hough, *Machine Analysis of Bubble Chamber Pictures, Int. Conf. on High Energy Accelerators and Instrumentation*, CERN (1959) 554.

[94] J. Blom, et al, *A Fuzzy Radon Transform for Track Recognition*, Proc. Computing in High Energy Physics Conference, San Francisco (1994).

[95] M. Ohlsson, C. Peterson and A.L. Yuille, *Track Finding with Deformable Templates: The Elastic Arms Approach*, Comput. Phys. Commun. **71** (1992) 77.

[96] R.E. Kalman, *A New Approach to Linear Filtering and Prediction Problems*, Transactions of ASME Journ. Basic Engineering **82** (1960) 35;
R.E. Kalman and R.S. Bucy, *New Results in Linear Filtering Prediction Theory*, Transactions of ASME Journ. Basic Engineering **83** (1961) 95.

[97] R. Frühwirth, *Application of Kalman filtering to track and vertex fitting*, Nucl. Instr. Meth. A **262** (1987) 444.

[98] C. Höppner, S. Neubert, B. Ketzer, and S. Paul, *A novel generic framework for track fitting in complex detector systems*, Nucl. Instr. Meth. A **620** (2010) 518.

[99] T.R. Saito *et al.*, *A proposal of the HypHI Phase 0 experiment*, submitted to GSI G-PAC 33.

[100] S. I. Bityukov et al, *On the observability of a signal above background*, Nucl. Instr. Meth. A **452** (2000) 518.

[101] S.I. Bityukov et al, Proc of Conf. Advanced statistical techniques in particle physics, Durham, UK, 18-22 March, 2002, p77.

[102] I. Narsky, *Estimation of upper limits using a Poisson statistic*, Nucl. Instr. Meth. A **450** (2000) 444.

[103] C. Amsler et al. (Particle Data Group), *Review of Particle Physics*, Phys. Lett. B **667** (2008) 1.

[104] H. Band, T. Motoba, and J. Zofka, *Production, structure and decay of hypernuclei*, Int. J. Mod. Phys. A **5** (1990) 4021.
D.H. Davis, *50 years of hypernuclear physics I. The early experiments*, Nucl. Phys. A **754** (2005) 3c.

[105] R. J. Prem and P. H. Steinberg, *Lifetimes of Hypernuclei,* ${}^{3}_{\Lambda}H$*,* ${}^{4}_{\Lambda}H$*,* ${}^{5}_{\Lambda}He$, Phys. Rev. **136** (1964) B1803.

[106] Y. W. Kang et al., *Lifetimes of Light Hyperfragments*, Phys. Rev. **139** (1965) B401.

[107] R. E. Phillips and J. Schneps, *Lifetimes of Light Hyperfragments. II*, Phys. Rev. **180** (1969) 1307.

[108] G. Bohm et al., *A measurement of the lifetime of the* ${}^{5}_{\Lambda}He$ *hypernucleus*, Nucl. Phys. B **23** (1970) 93.

[109] J. J. Szymanski, *Nonleptonic weak decay of* ${}^{5}_{\Lambda}He$ *and* ${}^{12}_{\Lambda}C$, Phys. Rev. C **43** (1991) 849.

[110] S. Kameoka et al., *Measurement of the* π^- *decay width of* ${}^{5}_{\Lambda}He$, Nucl. Phys. A **754** (2005) 173.

[111] S. Sawada, *J-PARC Facility*, Nucl. Phys. A **834** (2010) 701c.

[112] H. Tamura et al., *Gamma-ray spectroscopy of hypernuclei: Recent results and future plans*, Nucl. Phys. A **804** (2008) 73.
H. Tamura et al., *P13: Gamma-ray spectroscopy of light hypernuclei*,
http://j-parc.jp/NuclPart/pac_0606/pdf/p13-Tamura.pdf

Study of hypernuclei in the reaction ^{6}Li+^{12}C at 2 *A* GeV

This thesis presents a new experimental approach proposed by the HypHI collaboration to study hypernulei by means of reactions induced by stable and radioactive heavy-ion beams. The proposed method allows to measure hypernuclei formed by coalescence of a Λ-hyperon produced in the participant region and a projectile spectator fragment. Such a production mode offers the opportunity to investigate hypernuclei at extreme isospin and to measure directly hypernuclear magnetic moments. A first experiment aiming at demonstrating the feasibility of this new method has been carried out with a ^{6}Li beam at 2 *A* GeV impinged on a ^{12}C target by identifying ${}^{3}_{\Lambda}$H, ${}^{4}_{\Lambda}$H and ${}^{5}_{\Lambda}$He hypernuclei from their mesonic weak decay modes. The design, development and realization of this experiment are presented. Performances of the detectors and of the trigger system have been investigated. The software analysis developed for the reconstruction of hypernuclei is presented and its performances are evaluated using simulated data. The data analysis and preliminary results of the reconstruction of Λ hyperons and of ${}^{5}_{\Lambda}$He and the measurement of their lifetime are reported. The results demonstrate the feasibility of the new experimental approach for the study of hypernuclei and open new perspectives to investigate heavier hypernuclei toward the proton and neutron drip lines

KEY WORDS: Hypernucleus, hypernuclear spectroscopy, invariant mass spectroscopy, heavy ion collisions, ${}^{3}_{\Lambda}$H, ${}^{4}_{\Lambda}$H, ${}^{5}_{\Lambda}$He

---

Étude des hypernoyaux dans la réaction ^{6}Li+^{12}C à 2 GeV/nucléon

Cette thèse présente une nouvelle approche expérimentale proposée par la collaboration HypHI pour l'étude des hypernoyaux dans des réactions induites par des faisceaux d'ions lourds stables ou radioactifs. La méthode proposée permet de mesurer les hypernoyaux formés par coalescence entre un hypéron Λ produit dans la région des participants et un fragment spectateur issu du projectile. Ce mode de production offre la possibilité d'étudier les hypernoyaux dans des conditions extrêmes d'isospin et de mesurer directement leur moment magnétique hypernucléaire. Une première expérience ayant pour objectif principal de démontrer la faisabilité de la nouvelle méthode proposée, a été réalisée en effectuant une spectroscopie précise des hypernoyaux ${}^{4}_{\Lambda}$H, ${}^{3}_{\Lambda}$H et ${}^{5}_{\Lambda}$He produits dans les collisions ^{6}Li+^{12}C à une énergie incidente de 2 GeV par nucléon. La conception, le développement et la réalisation du nouveau dispositif de détection sont présentés. Les performances des détecteurs, ainsi que celles du système de déclenchement ont été étudiées. Le code d'analyse développé pour la reconstruction des hypernoyaux est présenté ainsi que ses performances sur les données simulées. L'analyse des données expérimentales et les premiers résultats de la reconstruction de l'hypéron Λ et de l'hypernoyau ${}^{5}_{\Lambda}$He, ainsi que la mesure de leur temps de vie, sont présentés. Ces premiers résultats démontrent la faisabilité de cette nouvelle approche expérimentale pour l'étude des hypernoyaux et ouvrent de nouvelles perspectives dans la recherche d'hypernoyaux lourds et proches des limites de stabilité.

MOTS-CLÉS : Hypernoyau, spectroscopie hypernucléaire, spectroscopie de masse invariante, collisions d'ions lourds, ${}^{3}_{\Lambda}$H, ${}^{4}_{\Lambda}$H, ${}^{5}_{\Lambda}$He

---

Résumé de thèse :

Cette thèse présente une nouvelle approche expérimentale proposée par la collaboration HypHI pour l'étude des hypernoyaux dans des réactions induites par des faisceaux d'ions lourds stables ou radioactifs. La méthode proposée permet de mesurer les hypernoyaux formés par coalescence entre un hypéron Λ produit dans la région des participants et un fragment spectateur issu du projectile. Ce mode de production offre la possibilité d'étudier les hypernoyaux dans des conditions extrêmes d'isospin et de mesurer directement leur moment magnétique hypernucléaire. Une première expérience ayant pour objectif principal de démontrer la faisabilité de la nouvelle méthode proposée, a été réalisée en effectuant une spectroscopie précise des hypernoyaux $^{3}_{\Lambda}$H, $^{4}_{\Lambda}$H et $^{5}_{\Lambda}$He produits dans les collisions ^{6}Li+^{12}C à une énergie incidente de 2 GeV par nucléon. La conception, le développement et la réalisation du nouveau dispositif de détection sont présentés. Les performances des détecteurs, ainsi que celles du système de déclenchement ont été étudiées. Le code d'analyse développé pour la reconstruction des hypernoyaux est présenté ainsi que ses performances sur les données simulées. L'analyse des données expérimentales et les premiers résultats de la reconstruction de l'hypéron Λ et de l'hypernoyau $^{5}_{\Lambda}$He, ainsi que la mesure de leur temps de vie, sont présentés. Ces premiers résultats démontrent la faisabilité de cette nouvelle approche expérimentale pour l'étude des hypernoyaux et ouvrent de nouvelles perspectives dans la recherche d'hypernoyaux lourds et proches des limites de stabilité.

Mots clefs : Hypernoyau, spectroscopie hypernucléaire, spectroscopie de masse invariante, collisions d'ions lourds, $^{3}_{\Lambda}$H, $^{4}_{\Lambda}$H, $^{5}_{\Lambda}$He

Abstract :

This thesis presents a new experimental approach proposed by the HypHI collaboration to study hypernulei by means of reactions induced by stable and radioactive heavy-ion beams. The proposed method allows to measure hypernuclei formed by coalescence of a Λ-hyperon produced in the participant region and a projectile spectator fragment. Such a production mode offers the opportunity to investigate hypernuclei at extreme isospin and to measure directly hypernuclear magnetic moments. A first experiment aiming at demonstrating the feasibility of this new method has been carried out with a ^{6}Li beam at 2 *A* GeV impinged on a ^{12}C target by identifying $^{3}_{\Lambda}$H, $^{4}_{\Lambda}$H and $^{5}_{\Lambda}$He hypernuclei from their mesonic weak decay modes. The design, development and realization of this experiment are presented. Performances of the detectors and of the trigger system have been investigated. The software analysis developed for the reconstruction of hypernuclei is presented and its performances are evaluated using simulated data. The data analysis and preliminary results of the reconstruction of Λ hyperons and of $^{5}_{\Lambda}$He and the measurement of their lifetime are reported. The results demonstrate the feasibility of the new experimental approach for the study of hypernuclei and open new perspectives to investigate heavier hypernuclei toward the proton and neutron drip lines.

Key Words : Hypernucleus, hypernuclear spectroscopy, invariant mass spectroscopy, heavy ion collisions, $^{3}_{\Lambda}$H, $^{4}_{\Lambda}$H, $^{5}_{\Lambda}$He